Contents

1 Introduction

This master thesis investigates the local variation of mechanical and physical properties of a grey iron cylinder head. The local variation in properties is also connected to microstructural parameters of the material. Finally, it also connects the casting simulation of a component to finite element analysis (FEA) of its behavior during usage. The thesis covers the exam work within the two-year Master of Science programme *Product Development and Materials Engineering* at Jönköping University School of Engineering. The work has been part of a research project within the Materials and Manufacturing department at Jönköping University.

1.1 Background

A better understanding of the casting process and its effect on the local mechanical and physical properties can lead to better cast component with improved properties. A way to simulate the behavior of a cast component prior to manufacturing is in line with the industry’s strive for product development of improved components at lower cost and in shorter time. This can in the long run lead to more optimized designs of components and thus lower weight which, if used in the automotive industry for example, will lead to lower fuel consumption and thus lower emissions. A both economic and environmental benefit.

Jönköping University, JU, has a rich history of world leading research related to casting and the research is made in close collaboration with the industry. The research group Materials and Manufacturing at JU are performing research on the topic Virtual and computational modeling of materials where for example the connection between microstructure of materials and the mechanical properties are connected. This thesis work is a part of the research project CCSIM2 (*Closing the Chain of SIMulation for cast components part 2*) with the industrial partner Volvo Group Trucks Operations in Skövde and Volvo Group Trucks Technology in Gothenburg.

J. Olofsson, in his doctoral thesis, formulated a simulation strategy to predict the local mechanical behavior throughout a whole cast component and also incorporate this into FEA simulations for structural analysis. The standard way of doing material definitions in FEA is to define only one material property for a whole component assuming homogeneous properties. However, as Olofsson emphasizes the complex casting process with e.g. varying thickness and thus varying solidification conditions leads to local variations of the material properties. The computer software developed by Olofsson creates material definitions for FEA which capture the local variations of the mechanical behavior. He found that the stress and strain distribution when including the local variations differed from the homogeneous material description.

In the research done by Olofsson, cast aluminium and ductile iron components was investigated in order to demonstrate the simulation strategy's relevance. In order to try to verify the software simulations with physical testing of the mechanical properties, a truck engine's cylinder head has been investigated. Three cylinder heads were cast consecutively from the same melt. Two of them has already been tested with tensile tests from 30 different locations throughout the component. The third cylinder head has not yet been tested which is why it is in the scope of this thesis to test the last one in order to verify the variation of the mechanical properties. The microstructural variations have to a limited extend been investigated of the two previous cylinder heads. Sample preparations for microstructure analysis has been performed for a few selected sample locations throughout the component and also images from optical microscope analysis has been taken from those samples.

What has not yet been investigated is to perform a comprehensive analysis of the microstructure and relating it the local variations of the mechanical properties and also the physical properties, which has not been investigated at all. Connecting the local microstructural variations throughout a cast component to the physical properties and implementing this into a simulation methodology which combines casting simulation and FEA is, to the authors' knowledge, something that has never been done before.

1.2 Purpose and research questions

A grey iron cylinder head from an industrial casting is to be investigated of its variation of material properties within the component, both mechanical and physical properties. A connection between the variation of properties and the local microstructure of the material is also to be made as well as working out and describing a methodology how to connect casting simulation with FE software to include local variation of physical properties. The research questions sought to be answered in this thesis are:

- *Will the local mechanical properties of cylinder head one and two be validated by the results from the third cylinder head?*
- *How are the mechanical properties varying within the studied component and can the variations be connected to the local microstructure of the material?*
- *How are the physical properties varying within the studied component and can the variations be connected to the local microstructure of the material and be predicted by a casting simulation?*
- *How can a casting simulation be connected to a FE software to include local variation of physical properties in FEA?*

Also examined in this thesis is a modelling procedure for thermal conductivity of cast iron based on microstructural parameters. The aim is to compare modelled values to experimental values from the studied cast component.

1.3 Delimitations

An investigation of the local variation of material properties in a casted grey iron cylinder head is conducted. No other alloys or components are studied in this thesis. The FEA made are using only the physical properties of the material which is experimentally determined in this thesis. The mechanical property testing is limited to tensile testing in order to verify the result from two previously studied components from the same melt. The microstructural analysis of the mechanical test samples is performed on six selected samples from each of the three cylinder heads, not on all the tested samples. The microstructure analysis is limited to the graphite microstructure and identifying the phases of the matrix of the grey iron, not analyzing the local variation of the matrix in detail.

1.4 Outline

The thesis begins by providing the reader with the theoretical background needed to understand the work conducted. How the approach to the research has been made is described including a graphical representation of the research approach. The studied material, grey iron, is described including its microstructural features. The mechanical behavior and the physical properties of grey iron as well as ways to model the mechanical behavior and the thermal conductivity are discussed. General information about the testing equipment used to determine the material properties is also provided.

How the work is carried out and the methods used is described in detail including how and where all the samples for mechanical and physical property testing were made. The testing procedures with all the parameters used when testing is defined. How the samples were prepared for, and examined, in optical microscope is explained as well as how the graphite microstructure is quantified using image analysis. The methodology to connect casting simulation to a FE software using local material properties determined experimentally is then described. The set-up of a FEA of the component to compare using a homogenous material definition to local variations in the material based on casting condition is described.

The results from all the material testing, mechanical and physical, is then presented and analyzed. The mechanical properties are compared to the results from the two previous components studied from the same melt. Images of the graphite microstructure from the same positions in the three components are compared. The connection between microstructural parameters of the graphite and the mechanical properties is examined in order to identify correlations. The samples for physical testing are also examined to find connections between the experimental test results and graphite microstructure from three different solidification times. Models for thermal conductivity based on the graphite microstructure are then compared to the test results. Also the results from the FEA are presented and analyzed.

Lastly the methods used in this thesis as well as the results are discussed. Conclusions are then drawn and recommendations for future work is also provided.

2 Theoretical background

This chapter describes the theories found in the literature that covers this thesis' topics. The research approach in the work is first presented followed by information about grey iron, the mechanical behavior of the material, the physical properties of it and common testing methods for determining the properties of the material studied in this thesis.

2.1 Research approach

Since this thesis will consist of experimental research the approached used is positivism which traditionally is associated with deductive reasoning and linked with hypothesis testing and quantitative methods.[1] Figure 1 shows an illustration of the research approach used in this thesis. It is based on an illustration of the positivist research design described in the book *Research methods for students, academics and professionals* [2] and a modified version of that illustration in the dissertation by J. Olofsson [3]. In this thesis the creation of hypothesis is mainly replaced with forming of research questions and they are attempted to be answered within the frame of the thesis work.

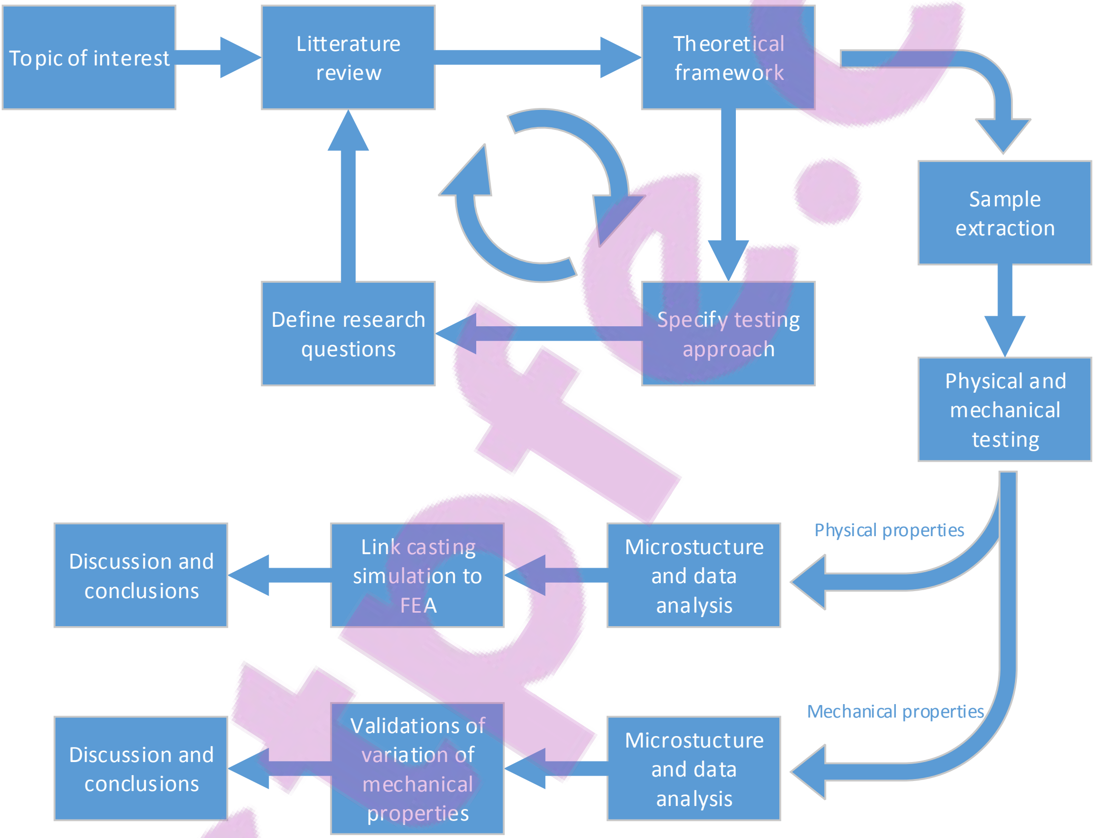

Figure 1. Illustration of the research approach used in this thesis.

The literature review contained reading previously published related research on the area of subject, e.g. J. Olofsson's doctoral thesis and the reports from the two previous tests performed on the other cylinder heads [4, 5]. The literature also included other doctoral theses, scientific articles and books.

The knowledge from the literature review is the base of the theoretical framework this thesis is based on. The framework also contains knowledge about the various machines and testing equipment used during the thesis work, the information was found in reading material about the equipment and getting personal instructions on each machine by experienced personnel. A full list of the literature and other sources of information to this thesis can of course be found in the reference list in section 6 and the people giving instructions are credited in the acknowledgements.

2.2 Grey iron

Grey iron, also called flake/lamellar graphite iron (FGI) is one classification type used to distinguish the varying microstructures of cast irons. The classification names are primarily describing the shape, size, distribution and quantity of the graphite found inside the alloy. Cast irons are a class of alloys within the large family of ferrous metals and as for all the cast irons the main component is iron (Fe). In grey iron the alloying elements can be divided into three groups e.g. the major alloying elements, the minor alloying elements and the trace elements.[6]

2.2.1 Composition

The major alloying elements of cast irons are carbon (C) and silicon (Si), making grey iron a Fe-C-Si alloy.[6] The chemical composition of grey iron usually contain a carbon content in the range of 2.5 - 4.0 % and a silicon content around 1.0 - 3.0 %.

The minor alloying elements e.g. phosphorus (P), sulfur (S) and manganese (Mn) are also added to the melt.[7] Addition of phosphorus has been observed to reduce both the mechanical properties i.e. tensile strength of the grey iron, and the eutectic temperature. The later mentioned effect has shown to increase the fluidity of the melt.[8] Sulfur has normally been considered to be an undesirable element in grey iron not only due to its promotion of e.g. intermetallic carbides and an increased chill tendency which exhibits negative effects, but also due to its reaction with iron. The reaction between S and Fe produce the phase FeS, which has a low melting point and can in elevated temperatures adopt a brittle behavior. To avoid the undesirable outcome of the FeS phase manganese is added to the melt to tie up the sulfur and produce MnS. Addition of sulfur has also exhibited positive effects e.g. promoting nucleation of graphite and increase the strength of the material up to a certain level.[9]

The trace elements, which has concentrations lower than 0.01 %, can involve e.g. aluminium (Al), bismuth (Bi), calcium (Ca), lead (Pb), tellurium (Te), titanium (Ti), tin (Sn) or nitrogen (N), and can be present in the grey iron either intentionally or unintentionally. The trace elements can have an important influence on both the microstructure and the properties of the grey iron.[6]

2.2.2 Microstructure

The graphite microstructure in grey iron can be characterized in different ways. The composition and the solidification condition of grey iron gives rise to the different microstructures in the material.

Graphite characterization

The graphite in cast irons are generally categorized into three main morphologies, e.g. lamellar, compacted or nodular. The shape of the graphite is determined by the preferred growth direction of the graphite within the hexagonal crystallographic structure, as can be seen in Figure 2.[10]

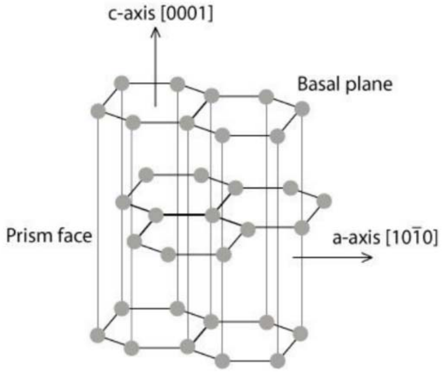

Figure 2. The hexagonal crystallographic structure of graphite [11].

It has been shown that the preferred direction of growth for the lamellar graphite is along the a-axis, to the contrary of nodular shaped graphite that shows a preferred growth direction in a radial manner along the c-axis. The compact graphite does not have one preferred growth direction and its growth mechanism seems more complex.[10]

In the flake/lamellar graphite iron, the graphite flakes can form in a variety of patterns and sizes. Both the pattern and the graphite flake size inside the grey iron are, according to the ASTM Internationals standard A247-10 [12], divided into two separate charts. One chart is identifying the pattern as either one of five types of patterns were each type has been assigned a classification letter going from A to E as seen in Figure 3. The other chart is identifying the graphite flake sizes and is subdivided into eight different length intervals as seen in Figure 4 and Figure 5.[12]

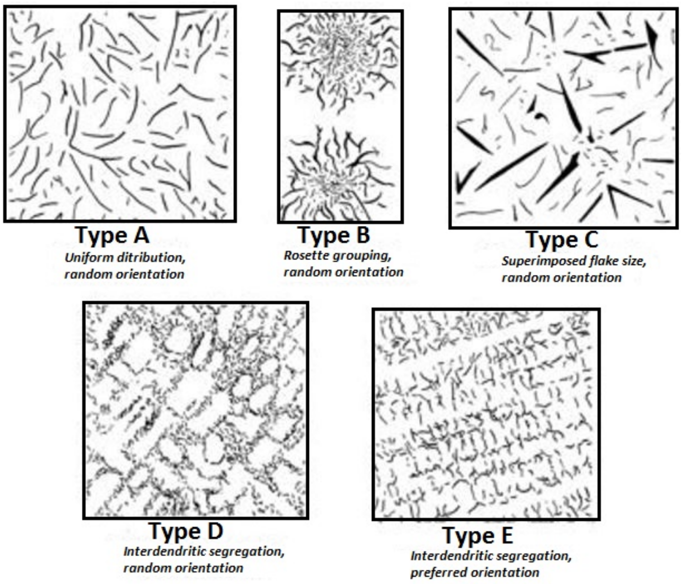

Type A *Uniform ditribution, random orientation*

Type B *Rosette grouping, random orientation*

Type C *Superimposed flake size, random orientation*

Type D *Interdendritic segregation, random orientation*

Type E *Interdendritic segregation, preferred orientation*

Figure 3. Displaying different distribution types of graphite flakes in grey iron according to the ASTM standard A247-10.[13]

Graphite flakes of type A has intermediate flake size and are defined as flakes randomly oriented inside the matrix.[14] Type A graphite is preferred for most applications but has demonstrated superior wear properties in comparison to the other types.[7]

Type B graphite is commonly described to have a rosette pattern where the flakes grows like clusters in the shape of rose petals. This distribution is typically observed when the cooling rate is fairly rapid such as in a component’s thinner sections or at the surface of the thicker parts.[7]

Type C flake graphite is distinguished by its large flakes of typical kish graphite that is formed in hypereutectic grey irons. The large graphite flakes increase the thermal conductivity but decreases the Young’s modulus of the component.[7]

Graphite flakes of type D is characterized by small interdendritic flakes that displays a random orientation in the matrix. The small flakes of type D are commonly generated due to a rapid cooling rate or at locations in a component were the sections are thin. The small flakes promote good surface finish when machined but is often surrounded by a matrix of ferrite that can cause soft spots in the castings.[7]

Type E flake graphite is also characterized by small interdendritic flakes but exhibits an organized orientation inside the matrix. The matrix is commonly of pearlitic structure and can be compared with the wear properties of the type A graphite.[7]

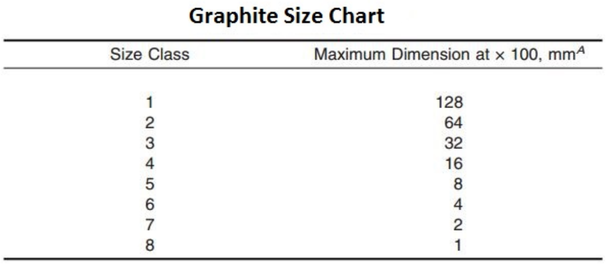

Graphite Size Chart

Size Class	Maximum Dimension at × 100, mm^A
1	128
2	64
3	32
4	16
5	8
6	4
7	2
8	1

Figure 4. The gradation of flake sizes in each size class, flakes measured in mm at a magnification of exactly 100 diameters.[12]

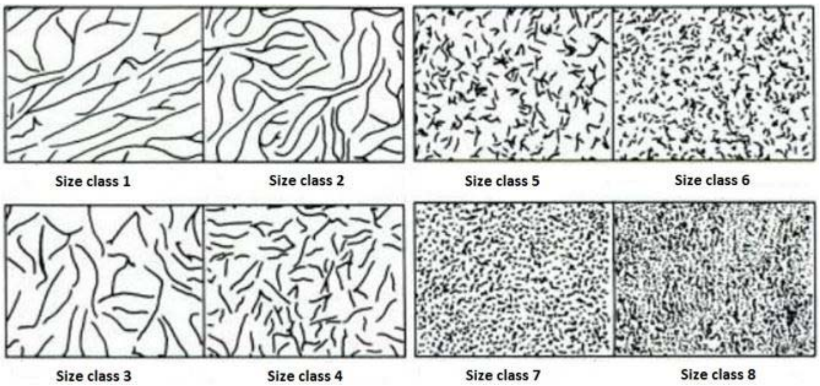

Figure 5. Graphite flake sizes in each size class as specified in ASTM A247-10.[15]

The graphite flakes lengths are important when identifying the strength of a casting. For example, if the matrix structure is assumed to be identical in two type A castings, the casting displaying small shorter graphite flakes when observed in an optical microscope is the casting also demonstrating the highest strength.[14] This is because the shorter graphite flakes disrupt the matrix to a less significant extent than the longer or much larger flakes. The larger flakes however improves the properties of thermal conductivity and is desired in applications promoting good damping qualities.[15] Therefore when describing a casting microstructure both the pattern and the size of the graphite flakes are of significant value.[14]

Solidification of grey iron

In order to estimate the structure of an iron-carbon alloy such as grey iron, the simplified model of the binary iron-carbon phase diagram is not enough. The complexity of the phase relationships between the alloying elements requires a more accurate clarification method. One approach is by using the carbon equivalent value, CE. By adding the most important alloying elements in their weight percentages together with the percentage of carbon, the CE value can be derived. In equation (1) both the carbon and the silicon percentage is taken into account.[10]

$$CE = \%C + \frac{\%Si}{3} \tag{1}$$

If the accuracy of equation (1) is still not fulfilling, an even more accurate approximation of the metal structure needs to be used. This is commonly done by adding the weight percentage of phosphorous to the equation as seen in equation (2).

$$CE = \%C + \frac{\%Si}{3} + \frac{\%P}{3} \tag{2}$$

Equation (2) is the one that demonstrate most similarity to the equation used by Volvo. Volvo use a modified version that calculates the CE value of grey iron as shown in equation (3).

$$CE = \%C + \frac{\%Si}{4} + \frac{\%P}{2} \tag{3}$$

The calculated *CE* value is used to categorize the melt of the grey iron into either a hypoeutectic, a eutectic or a hypereutectic grey iron. The eutectic grey iron normally has a *CE* value of 4.3 % whilst a hypoeutectic has a value below 4.3 % and a hypereutectic a value higher than 4.3 %. The three categories displays a distinct difference in microstructure when observed in an optical microscope as seen in Figure 6.[10]

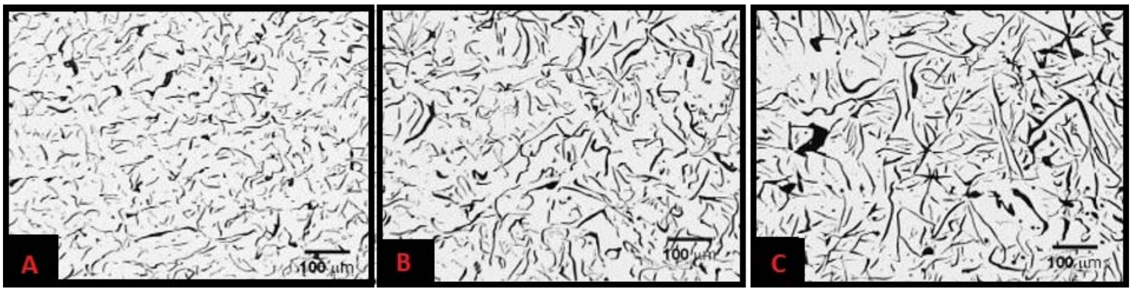

Figure 6. Microstructure of unetched grey iron samples. (A) Hypoeutectic (<4.3% CE), (B) eutectic (4.3% CE), (C) hypereutectic (>4.3% CE).[16]

When observing the solidification sequences of the three categories, dissimilarities can be seen in the first phase that is precipitating as displayed in Figure 7.

When solidification occurs in a hypoeutectic melt the first phase to precipitate is austenitic dendrites. As the proeutectic phase will continue to grow the carbon level will increase in the rest of the melt until the melt reaches the eutectic temperature, T_E. When T_E is reached the eutectic solidifications begins with eutectic growth from numerous nuclei points. The eutectic cells that has formed grows with almost spherical structure until they have consumed the remaining liquid. The proeutectic austenitic dendrites grows parallel to the eutectic austenite but is hard to distinguish without etching the samples.[7]

In a eutectic melt, solidification starts at a regular eutectic temperature, T_E, without any prior formation of proeutectic constituent. It makes the solidification rate the controlling factor. If there is enough undercooling during the solidification the T_E can be lowered which can result in a modification of the expected microstructure, e.g. go from a type A to E or form carbides.[7]

When the hypereutectic melt solidifies, kish graphite is the first to precipitate and can be described as large, straight flakes or as thick, lumpy flakes that often are found at the surface of the melt due to their low density. When the temperature has been lowered to T_E the remaining liquid will continue to solidify with a eutectic structure.[7]

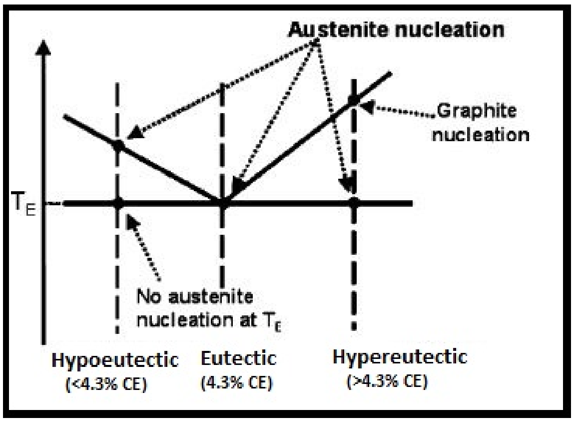

Figure 7. Schematic section of the eutectic region of the Fe–C equilibrium diagram.[16]

The austenite phase will start to decompose with further decrease in temperature by precipitating the dissolved carbon. When reaching the eutectoid temperature this transformation is completed with the result that austenite generally has transformed to either perlite with graphite or ferrite with graphite. Ferrite with graphite is mostly found if the cooling rate is slow, if the ferrite has a high silicon content or a high CE value. The transformation to perlite structure is common if the cooling rate is relatively fast with a relatively low CE value.[7]

2.3 Mechanical behavior

The mechanical behavior of metallic materials can be determined by applying a uniaxial tension load resulting in a stress-strain curve as can be seen in Figure 8. Stress is defined as in equation (4).

$$\sigma = \frac{F}{A} \tag{4}$$

Where F is the force and A is the cross-sectional area. Strain is a unit less measure of the distortion which during tensile testing is the elongation. Engineering stress and strain, shown by the red curve (A) in Figure 8, are calculated using the initial cross-sectional area, A_0, while true stress and strain, shown by the blue curve (B) in Figure 8, are calculated using the current area, A.

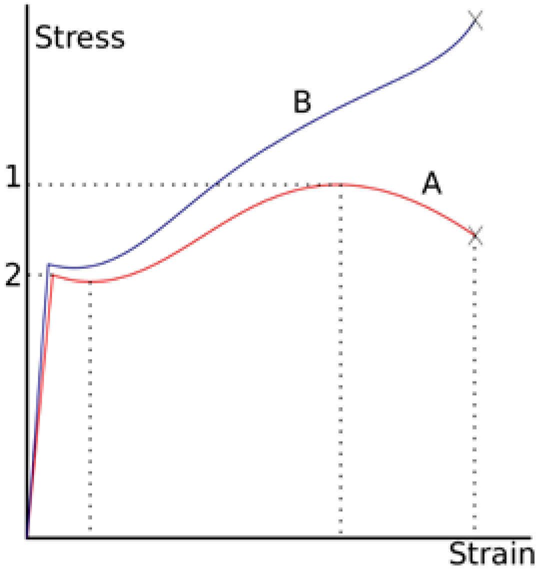

Figure 8. Typical stress-strain curves for structural steel [17]. The red curve (A) shows the engineering stress-strain and the blue (B) show the true stress-strain curve.

The mechanical properties, e.g. Young's modulus (E), yield strength and ultimate tensile strength, can be extracted from a stress-strain curve. Yield strength is the stress at which the material starts to plasticize. For some materials, such as many steels, the yield strength (YS) is determined by the stress value where the linear part of the stress-strain curve transcends to the non-linear plastic part, see point 2 in Figure 8. For many cast iron alloys including grey iron the yield stress at zero plastic strain is hard to identify. The yield stress is therefore often determined at 0.2% plastic strain (Rp0.2). Ultimate tensile strength (UTS), the highest point on an engineering stress-strain curve, point 1 in Figure 8, is the maximum stress the material can withstand before breaking.[3]

2.3.1 Modelling of tensile deformation curve

In cast irons the deformation behavior is primarily controlled by the graphite phase and the constituents in the matrix. By modifying the amount of graphite and its morphology, both the elastic and plastic deformation will be affected. The deformation of a grey iron alloy has been observed and documented when subjected to a tensile test. Four stages of deformation has been distinguished[18]:

- Purely elastic deformation of matrix.
- Plastic deformation of matrix at point of high stress.
- Recoverable strain due to the opening of the graphite cavities.
- Permanent strain associated with the opening up of cavities.

Due to the linear behavior of the true stress σ (Pa) and the true strain ε_{Total} (-) within the elastic region of a tensile test curve an approximation of the true elastic strain ε_{el} (-) can be made using Hooke's law, in which E is the Young's modulus . [10, 19]

$$\sigma = E \cdot \varepsilon_{el} \tag{5}$$

The true total strain is divided in to the true elastic strain ε_{el} and the true plastic strain ε_{pl}.

$$\varepsilon_{Total} = \varepsilon_{el} + \varepsilon_{pl} \tag{6}$$

For grey iron, which does not present a distinct elastic region, the Young's modulus is hard to determine. Figure 9 shows two ways of approximating the Young's modulus, one is by determining the slope of a tangent at $\sigma = 0$. A more common way is to use the secant method at 25 % of the ultimate tensile strength in which the slope of the secant determines the Young's modulus. The yield strength (Rp0.2) is also hard to determine since it is closely connected to the modulus of elasticity.

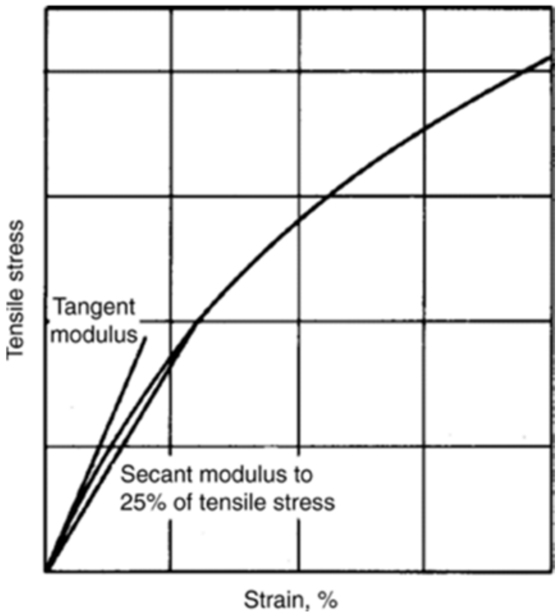

Figure 9. Two different ways to determine the elastic modulus for grey iron, tangent modulus at no load and secant modulus and 25 % of the UTS.[7]

The stress values of the plastic region can also be approximated using a variety of suitable equations, e.g. Hollomon, Ludwigson, Ludwik, Swift and Voce. Two of the most commonly used equations are the Hollomon equation and the Ludwigson equation.[10, 20]

$$\sigma_{Hollomon} = K_H \cdot \varepsilon_{pl}^{n_H} \tag{7}$$

$$\sigma_{Ludwigson} = \left(K_H \cdot \varepsilon_{pl}^{n_H}\right) + \Delta \, , (\Delta = e^{K_L + n_L \cdot \varepsilon}) \tag{8}$$

The Hollomon equation is derived from a previously used approximation model known as the Ludwik model that also contained the stress constant σ_0.[21] In the Hollomon equation the relationship between stress σ and plastic strain ε_{pl} is defined using the strain hardening exponent n_H (-) and the strength coefficient K_H (-).[19] The value of K_H gives an indication of the material strength and the forces required to deform it. The exponent n_H provides important information concerning two material properties, e.g. it signifies the strain hardening or work hardening characteristics of the material and it also works as an indicator for the materials stretch formability. A material with a high value of n_H is preferred for processes which involves plastic deformation while a material with a low value is a good machinable material.[20] The value of the strain hardening exponent n_H varies between *0* and *1* and describes if the material acts perfectly plastic ($n_H = 0$) or if it has a linear deformation hardening behavior ($n_H = 1$).[19] For most metallic materials the n_H value varies between *0.1* and *0.5*.[18]

The Hollomon equation assumes a linear relationship between the logarithms of the true stress and the true strain where the exponent n_H is given by the slope.[10] The Ludwigson equation later added an exponential correction term, (Δ), to the Hollomon equation as seen in Figure 10. The correction term was added to account for deviations at low strains containing the new parameters K_L (lnPa) and n_L (lnPa).[10, 19, 21]

$$log\sigma_{Hollomon} = logK_H + n_H \cdot log\varepsilon_{pl} \tag{9}$$

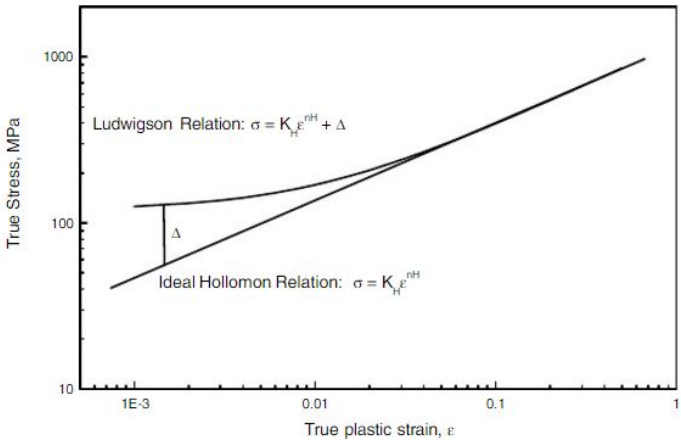

Figure 10. A typical double logarithmic plot of the true stress and true plastic strain. Presenting the curves of Hollomon equation and Ludwigson equation with the correction term at low strains.[20]

2.4 Physical properties

Cast irons, including grey iron, cannot be seen as homogenous when looking at the different physical, or thermal, properties. The amount of graphite affects the density and the specific heat while the size, shape and distribution of the graphite flakes highly affects the thermal conductivity. The matrix structure however is having a significant influence of the thermal expansion of grey iron.[7] These four physical properties are described in this section. Density and specific heat are mostly of interest in order to be able to determine the thermal conductivity, which together with thermal expansion are important properties of a cylinder head and similar cast components that are subjected to heat during its service. E.g. thermal stresses are developed across the cylinder head due to non-uniform expansion caused by temperature gradients within the component during usage. Low thermal expansion limits the thermal stress and high thermal conductivity reduce the temperature gradient.

2.4.1 Thermal expansion

A material, most often, expands when heated. Thermal expansion is a measure of this tendency. It can be either the change in length or the volumetric change. The formulas for thermal expansion are[22, 23]:

$$\alpha_L = \frac{1}{L} \cdot \frac{dL}{\mathrm{d}T} \tag{10}$$

$$\alpha_V = \frac{1}{V} \cdot \frac{dV}{\mathrm{d}T} \tag{11}$$

The coefficient α_L, for linear, and α_V, for volumetric, is the material property and the unit is 1/°C or 1/K. The unit for α_L is often expressed as µm/(m·°C) to get a more convenient number which for most metals is between 5 and 25. The thermal expansion is not constant but varies with temperature. The coefficient is also referred to as CTE, coefficient of thermal expansion. For isotropic materials the volumetric thermal expansion coefficient is three times the linear expansion coefficient.

$$\alpha_V = 3 \cdot \alpha_L \tag{12}$$

A low thermal expansion is desired in many applications, e.g. cylinder heads, where the dimensional tolerances needs to be kept at varying temperatures. For grey iron it is around 10 μm/(m·°C) at room temperature, but can rise up to 16.9 μm/(m·°C) at temperature up to 1070 °C.[7] Aluminium for comparison, which is both lighter and has higher thermal conductivity than grey iron, has a thermal expansion coefficient of around 23 which is why it is less common as a cylinder head material since it causes fretting and wear between the cylinder head and the cylinder block.[24] The matrix structure is what has the greatest impact on grey iron's thermal expansion. Ferritic and martensitic irons have slightly higher thermal expansion compared to pearlitic irons. The thermal expansion is commonly measured using a dilatometer.[7]

Result from experiments [25, 26] when measuring the thermal expansion for castings of the same melt in different solidification conditions, sand and insulation yielding solidification times of approximately 300 s and 1100 s respectively, shows no connection between solidification time and thermal expansion.

2.4.2 Density

Density is defined as the mass per unit volume and the formula for density is:

$$\rho = \frac{n \cdot A}{V_C \cdot N_A} \tag{13}$$

Where n is the number of atoms in one unit cell, A is the atomic weight, V_C is the volume of the unit cell and N_A is Avogadro's number, which is $6.022 \cdot 10^{23}$ atoms/mol.[27] The unit of density is kg/m^3, often also g/cm^3. According to Archimedes' principle, the buoyance, the upward force, of an object submerged in a fluid is equal to the gravitational force on the displaced fluid. The following formula can then be used to determine the density of an object:

$$\rho_o = \frac{m_o \cdot \rho_f}{m_f} \tag{14}$$

Where ρ denotes density, m denotes mass and the subscripts o and f denotes object and fluid respectively. Since, as described in section 2.4.1, materials expand with increased temperature the volume and thus the density of a material decreases with an increase of temperature. Grey iron at room temperature has a density of around 6800-7400 kg/m^3. The width of the span is due to the great difference in density of the microconstituents of grey iron. The matrix phases, e.g. ferrite, austenite, pearlite, cementite and martensite have densities around 7600-7900 kg/m^3, while graphite has a density of only 2250 kg/m^3.[7]

2.4.3 Specific heat

Heat capacity is a property which indicates a materials ability to absorb external heat. It represents the energy needed to rise the temperature of the material by one unit. Specific heat capacity, or often just specific heat, also includes the mass of the material, i.e. the energy needed to increase the temperature one unit per unit mass, which makes the formula for specific heat[22, 28]:

$$C_p = \frac{dQ}{m \cdot dT} \tag{15}$$

The unit for specific heat is therefore J/(kg·K). The subscript p denotes that it is maintained under constant external pressure. Specific heat is often measured by a Differential Scanning Calorimetry (DSC). Specific heat is highly temperature dependent, with higher values at higher temperatures. For grey iron at room temperature the value is around 565 J/(kg·K).[29] The specific heat is lower for graphite than for iron, meaning local areas of more graphite can have a slightly lower specific heat than area with less graphite, however the difference is small.

2.4.4 Thermal conductivity

A material's ability to transfer heat is the definition of the property called thermal conductivity. It can be measured in several ways, either directly or, as has been done in this thesis, measure the thermal diffusivity and then calculating the conductivity. Thermal diffusivity is a measure of a materials ability to spread, or diffuse, thermal energy. The thermal conductivity, λ (k is also often used), of a material is related to thermal diffusivity, α, by the materials specific heat, C_p and density, ρ, by the formula[30]:

$$\lambda = \alpha \cdot \rho \cdot C_p \tag{16}$$

The unit of thermal conductivity is W/(m·K). The thermal diffusivity is, in this thesis, measured by laser flash analysis (LFA). The unit for thermal diffusivity is m^2/s or often more conveniently mm^2/s. In cast iron, including grey iron, several factors influence the thermal conductivity, e.g. graphite morphology, temperature, microstructure and alloying addition. The graphite's shape has the most important influence where flakes of graphite have higher thermal conductivity than spheroidal or compacted shapes of graphite, as illustrated by Figure 11.[31] This means that grey iron, which is composed of graphite flakes, has higher thermal conductivity compared to other types of cast iron. The microconstituents of the material have different values of thermal conductivity, ferrite around 70-80 W/(m·K), pearlite around 50 W/(m·K) and cementite only around 7 W/(m·K). Graphite along the c-axis, see Figure 2, has thermal conductivity of around 80-85 W/(m·K) while for graphite along the basal plane, the a-axis, the thermal conductivity can be as high as 285-425 W/(m·K). [7]

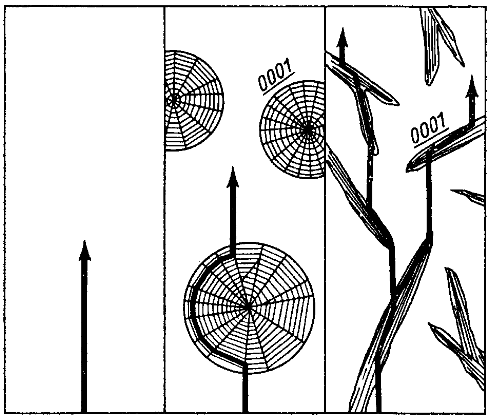

Figure 11. Illustration of thermal transport in steel, nodular cast iron and lamellar graphite iron.[32]

As concluded in [33] structures with straighter and less branched graphite have higher thermal conductivity but the difference decrease at higher temperatures. Also, if cementite is present in the material the thermal conduction is reduced at all temperatures.

Modelling thermal conductivity

Grey iron, as all cast irons, can be seen as a composite material with several phases with different thermal conductivities. The total thermal conductivity of a phase is the sum of the contribution from heat carried by electrons and phonons, which comes from lattice vibrations.[34, 35]

$$\lambda = \lambda_{ph} + \lambda_{el} \tag{17}$$

The thermal conductivity of cast irons can be estimated by knowing the thermal conductivity and the volume fractions of each microconstituents as well as the aspect ratio, also known as the shape factor of the graphite particles, ε [25]. The graphite particles are modelled as ellipsoidal discs with semi-axes of length c and a in the basal planes in the graphite so the shape factor is also referred to as c/a [36]. The aspect ratio can be determined by metallographic observations. First Löhe's parameter, η, needs to be calculated [25, 36].

$$\eta = Average\ of \left(\frac{\pi \cdot l_{max}}{4 \cdot A}\right) \tag{18}$$

Where l_{max} is the principal intersectional length of the graphite particles, called Feret max later in the thesis, and A is the sectional area of it. Both chosen in an arbitrary cross-sectional metallographic plane. Löhe's parameter can be referred to as the inverse of roundness. Roundness, or roundness shape factor (RSF), is defined as:

$$RSF = \frac{A}{A_m} = \left(\frac{4 \cdot A}{\pi \cdot l_{max}}\right) \qquad (19)$$

Where A, Am and l_{max} or l_m is defined as shown in Figure 12.

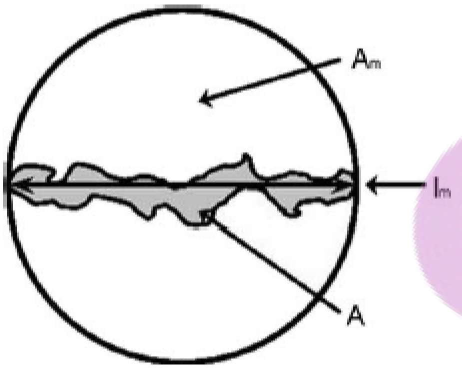

Figure 12. Illustration of the parameter used to calculate Löhe's parameter and roundness.[37]

Having Löhe's parameter, η, the aspect ratio, c/a or ε, can be calculated by [36]

$$\eta = \frac{2 + (c/a)^2}{3 \cdot (c/a)^2} \cdot \frac{2}{1 + \frac{\arccos(c/a)}{(c/a) \cdot \sqrt{1 - (c/a)^2}}} \qquad (20)$$

This is mostly used for calculation of the aspect ratio in CGI, for FGI the aspect ratio can be assumed to be *0.05* [34, 38].The effective thermal conductivity, λ^*, of a grey iron alloy can be calculated as: [34]

$$\lambda^* = \lambda_\beta^* + \frac{1}{3} \cdot f_\alpha \cdot \lambda^* \cdot \left(\frac{\lambda_{\alpha,z} - \lambda_\beta^*}{\lambda^* + p_z\left(\lambda_{\alpha,z} - \lambda^*\right)} + 2 \cdot \frac{\lambda_{\alpha,x} - \lambda_\beta^*}{\lambda^* + p_x\left(\lambda_{\alpha,x} - \lambda^*\right)}\right) + 3 \cdot f_\gamma \cdot \lambda^* \cdot \frac{\lambda_\gamma - \lambda_\beta^*}{2 \cdot \lambda^* + \lambda_\gamma} \qquad (21)$$

In equation (21) the following two expressions are also needed:

$$p_x = \varepsilon \cdot (2 - 2 \cdot \varepsilon^2)^{-1} \cdot \left[(1 - \varepsilon^2)^{-1/2} \cdot \arccos(\varepsilon) - \varepsilon\right] \qquad (22)$$

$$p_z = 1 - 2 \cdot p_x \qquad (23)$$

The subscripts α, β and γ represents the different phases, graphite, pearlite and alloyed ferrite respectively. The γ-phase is modelled as spheroids, the α-phase as ellipsoidal discs surrounded by a matrix of β-phase [25]. The volume fractions of the phases are denoted f. The graphite, α-phase, is significantly anisotropic and the subscript z represents the direction perpendicular to the basal plane, c-axis, while x represents the direction parallel to the basal plane, a-axis, $\lambda_{\alpha,x}=\lambda\alpha_{,y}>>\lambda_{\alpha,z}$. The alloyed ferrite is assumed isotropic while the pearlite is anisotropic with $\lambda_{\parallel}=\lambda_{\beta,x}=\lambda_{\beta,y}>\lambda_{\beta,z}=\lambda_{\perp}$ and λ^*_β is the overall thermal conductivity of the pearlite matrix. The thermal conductivity of the pearlite matrix is calculated as:

$$\lambda_\beta^* = \frac{1}{4} \cdot \left[\lambda_x + (\lambda_x^2 + 8 \cdot \lambda_x \cdot \lambda_z)^{1/2}\right] \qquad (24)$$

$$\lambda_{\parallel}(pearlite) = f(Fe_3C)\cdot\lambda(Fe_3C) + f(ferrite)\cdot\lambda(ferrite) \tag{25}$$

$$\lambda_{\perp}(pearlite) = \left(\frac{f(Fe_3C)}{\lambda(Fe_3C)} + \frac{f(ferrite)}{\lambda(ferrite)}\right)^{-1} \tag{26}$$

The thermal conductivity of each of the microconstituents in grey iron are listed in Table 1.

Table 1. Thermal conductivity of the microconstituents in cast irons [34].

Microconstituents	λ [W/m·K]
Alloyed ferrite (2wt% Ni, 1.5wt% Si)	30
Cementite	8
Graphite, $\lambda_{\parallel}$ (a-axis)	500
Graphite, $\lambda_{\perp}$ (c-axis)	10
Lamellar alloyed pearlite, $\lambda_{\parallel}$	27.3
Lamellar alloyed pearlite, $\lambda_{\perp}$	22.5

This model of the thermal conductivity is only valid at around room temperature and does not take into account the large influence the temperature has on the thermal conductivity of cast iron. Also, as concluded by Holmgren [25] this modelling procedure is quite accurate for compacted graphite iron and grey iron with undercooled graphite but it underestimates the thermal conductivity of grey iron with type A lamellar graphite, as seen in Figure 13. This might be explained by the fact that the graphite morphology and the aspect ratio is determined by sectioning the graphite particle in a 2D-plane.

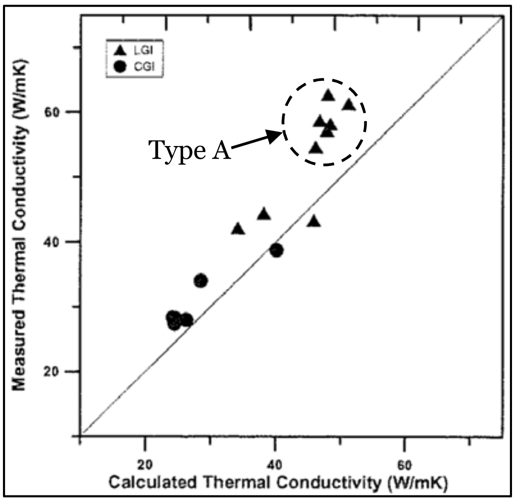

Figure 13. Measured vs. modelled values for thermal conductivity for LGI=grey iron and CGI=compact graphite iron at room temperature.[25] The model underestimates the values for grey iron with type A lamellar graphite, the values within the dashed circle.

In a more recent paper by Holmgren [38] the thermal conductivity of graphite along the basal plane was determined inversely using equation (21) together with experimentally determined values for the thermal conductivity of the pearlite matrix [39], as can be seen in the left graph in Figure 14 and using an aspect ratio of 0.05. The effective thermal conductivity was established experimentally for a FGI with a solidification time of around 200 s. The calculated thermal conductivities of the graphite at different temperatures can be seen in the right graph in Figure 14.

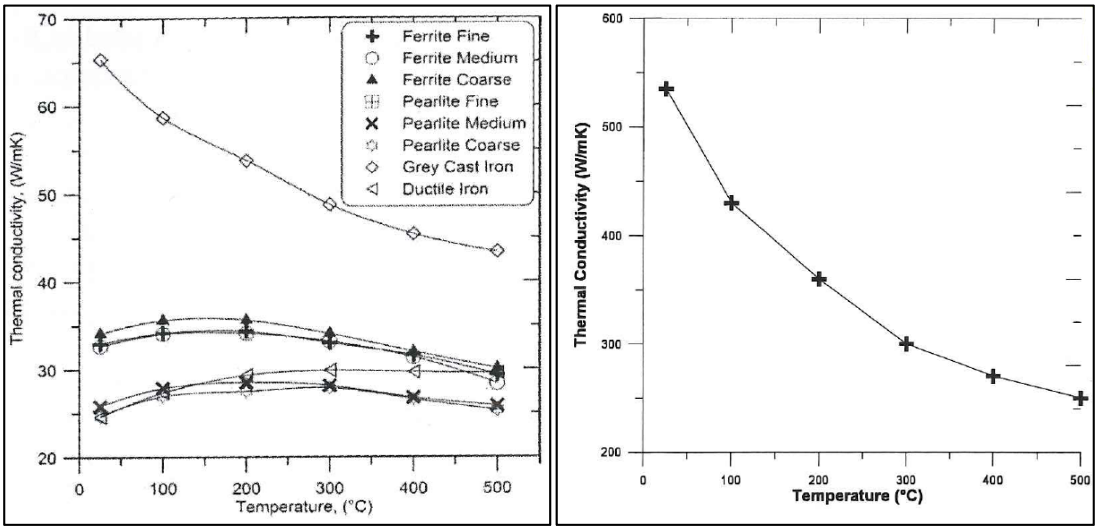

Figure 14. Left graph showing experimentally determined thermal conductivities of different matrices. Right graph shows the calculated thermal conductivity of graphite along the basal plane. [38]

2.5 Material testing

This section describes the different testing procedures used to measure the material properties described in section 2.3 and 2.4.

2.5.1 Tensile testing

Tensile testing, using a tensile test testing machine like the one seen in Figure 15, is one of the most common way to determine a material's mechanical behavior. The tensile test specimen, with typically a circular cross section, are gripped in the testing machine by their large end section and an increasing tensile load is applied.[40] The ISO standard for tensile tests is ISO 6892-1.[41] A laser extensometer is used to measure the strain while the test is performed at a constant cross-head speed. The result is commonly in the form a table of the force applied and the actual cross section area for that force. Form that, a true stress-strain curve as described in section 2.3 can be compiled from which the mechanical properties, e.g. UTS, can be determined.

Figure 15. A Zwick/Roell Z100 tensile testing machine used to perform tensile tests. The displacement is measured using a green laser extensometer.

2.5.2 Dilatometer (DIL)

To measure thermal expansion of a material a push-rod dilatometer, like the one in Figure 16, is commonly used. First a small cylindrical shaped standard sample is placed in a furnace with a controlled atmosphere, often helium, and heated to a pre-determined temperature. Then the same procedure is made for the sample of the material to be tested. The change in length of the sample, which is caused by the thermal expansion of the material, is transmitted by a push-rod to a displacement gauge. Both the change in length, ΔL, and the change in temperature, ΔT, is measured throughout the test. The thermal expansion coefficient, explained in section 2.4.1 can then be calculated using equation (27).[42]

$$\alpha_L = \frac{\Delta L}{L_0 \cdot \Delta T} \tag{27}$$

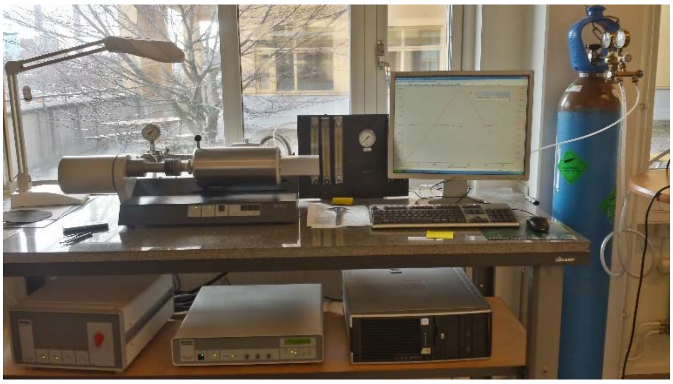

Figure 16. A Netzsch DIL 402C push-rod dilatometer used to measure thermal expansion.

2.5.3 Density determination

Archimedes' principle can be used to measure the density of a material at room temperature, the principle is described in section 2.4.1. A sample of the material to be tested is weighed using an analytical balance together with a set for density determination, like the one seen in Figure 17. The sample is weighted first in the air and then submerged in water and weighted again. The analytical balancer then calculates the density of the material, using equation (14), and displays it. The density at any given temperature, $\rho(T)$, can be calculated using the density of the material at room temperature, RT, and the thermal expansion coefficient, α_L at that temperature.[43]

$$\rho(T) = \frac{\rho(RT)}{1 + 3 \cdot \alpha_L(T) \cdot \Delta T} \tag{28}$$

Figure 17. An analytical balance used to determine density by weighing a sample first in air (left picture) and then in water (right picture).

2.5.4 Differential Scanning Calorimetry (DSC)

Differential Scanning Calorimetry (DSC), using a machine like the one seen in Figure 19, is a popular method to determine the specific heat of a material. It uses a single heating chamber to heat up two crucibles in a controlled atmosphere, often argon. The measurement must be run three times under equal conditions. First with two empty crucibles to get a baseline, then with one empty crucible and one with a standard reference sample. The third measurement is run with one empty crucible and one crucible with the sample of the material to test. The heat flow differences of the standard sample and the material sample to the baseline is then determined, defined as H as seen in Figure 18. The heat flow differences, H, the known specific heat, C_p, of the standard and the two masses can then be used to calculate the specific heat of the sample material [44]:

$$c_{p_{sample}} = \frac{H_{sample} \cdot m_{sample} \cdot c_{p_{standard}}}{H_{standard} \cdot m_{standard}} \tag{29}$$

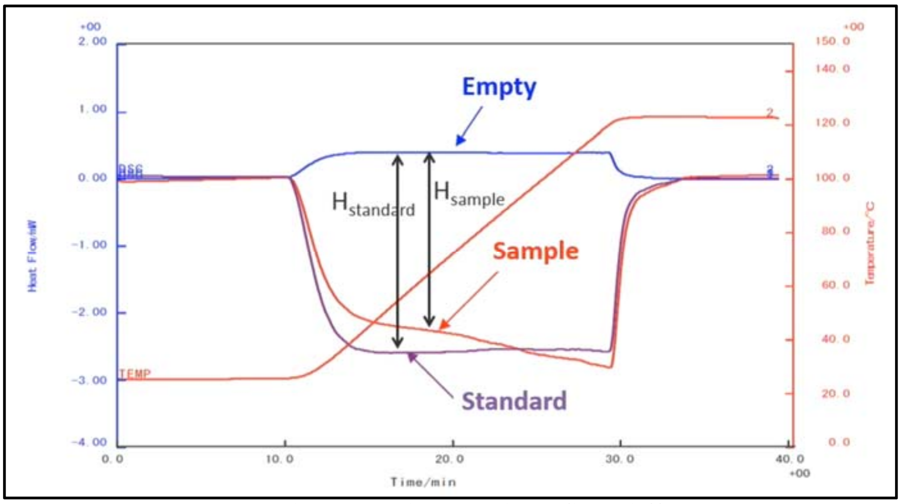

Figure 18. DSC diagram showing heat flow differences.[44]

Figure 19. A DSC machine, Netzsch DSC 404 C, used to determine the specific heat.

2.5.5 Laser Flash Apparatus (LFA)

As mentioned in section 2.4.4 the thermal diffusivity is often measured when the thermal conductivity is sought. The laser flash method, using a laser flash apparatus like the one seen in Figure 20, is a standard way of measuring thermal diffusivity of a material. A disc shaped sample of the material, which must be opaque against laser, is heated at one end by a laser pulse inside a heating chamber with a controlled atmosphere, often argon. The heat from the laser is transported through the sample and the change in temperature on the side opposite to the laser pulse is monitored. The thermal diffusivity can then be calculated by the half time method:

$$\alpha = \frac{0.1388 \cdot L^2}{t_{1/2}} \tag{30}$$

Where L is the thickness of the sample and $t_{1/2}$ is the time it takes for the rear surface to reach half of the maximum temperature. The unit of thermal diffusivity is m^2/s. This formula is true if the system is adiabatic without radiation and if the material is homogeneous. Although there are models that corrects for the influence of heat losses and inhomogeneity.[45]

Figure 20. A laser flash apparatus, Netzsch LFA 427, used to determine the thermal diffusivity.

3 Method and implementation

This thesis consists of a substantial amount of practical work, extracting material samples which were then tested to measure the material properties at different locations throughout the component studied. The material was also studied in optical microscope and the graphite morphology was quantified using image analysis. At the end of this chapter follows a description of a methodology worked out to connect casting simulations FEA using the experimentally measured local physical properties.

3.1 The component studied

The component studied in this thesis is a CH11 cylinder head from a Volvo truck diesel engine, weighing in at around 220 kg. It is cast in grey iron with the material composition as stated in Table 2. A cylinder head is a component which is bolted on top of the cylinder block of an engine and it is housing the valves for the inlet air and the exhaust gas, the fuel injector and cooling channels. The cylinder head is subjected to high temperatures during the combustions but also fluctuating temperatures and pressures.[24] A key aspect for the material in a cylinder head is that it must transport away the generated heat efficiently to limit thermal fatigue, i.e. have high thermal conductivity, while also maintaining the correct dimensions i.e. have low thermal expansion. The thermally induced stresses are also reduced by low thermal expansion, small thermal gradients and low stiffness of the material. The findings in this research is not limited to cylinder heads but could also be of interest in other components where the physical properties are of great interest, e.g. brake discs, cylinder blocks and furnaces.[32]

Table 2. Chemical composition of the cylinder head.[5] C_{ekv} is the carbon equivalent calculated using equation (3).

C	Si	Mn	P	S	Cr	Ni	Mo	Cu	Sn	Ti	V	**C_{ekv}**
3.11	1.88	0.49	0.05	0.09	0.14	0.06	0.19	0.83	0.051	0.010	0.017	**3.61**

3.2 Sample extraction

Material samples for testing were extracted at different locations throughout the cylinder head. How and where samples were taken and why they were taken at those locations are described in this section.

3.2.1 Mechanical property sample extraction

In total 30 tensile test specimens were extracted from the third cylinder head from six different locations in five of the six cylinders. No samples were taken from cylinder one due to its deviating geometry. The samples for mechanical testing were taken at locations according to an extraction plan from a previous work by T. Svensson and G. Stark [5], as seen in Figure 21, used for the first cylinder head. This plan was also followed in another previous work by M. Li [4] when studying the second cylinder head. This plan was followed in order to be able to validate the results of the mechanical testing from previous work.

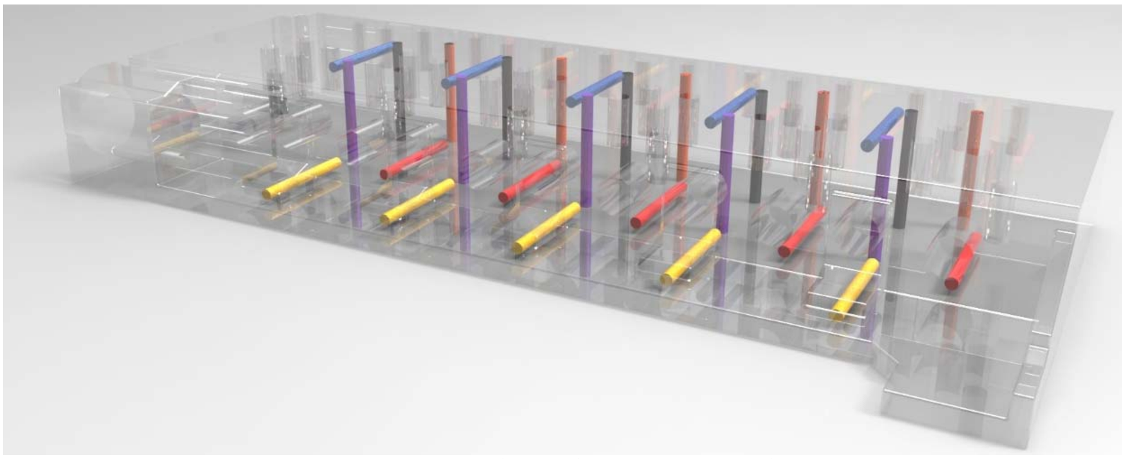

Figure 21. Tensile test bar extraction plan.

The working steps when extracting the test specimens were as followed:

- Removing excess material to fit the cylinder head into the bandsaw.
- Cut the cylinder head into sections, one for each cylinder.
- Divide each cylinder section into an A-part and a B-part.
- Extract rectangular cuboids of test specimens.
- Lathe the test specimens into cylindrical bars.
- CNC-lathing into final tensile test bar shape.

The tensile test specimens were machined to the correct size according to Volvo standard STD 1014,213 and the designation used is the 7C35.[46] The sample extraction was started by removing a large section, section zero, of excess material by angle grinding as marked by the red line in Figure 22. This was because the large 220 kg heavy cylinder head exceeded the maximum width of the vise of the bandsaw for metal cutting.

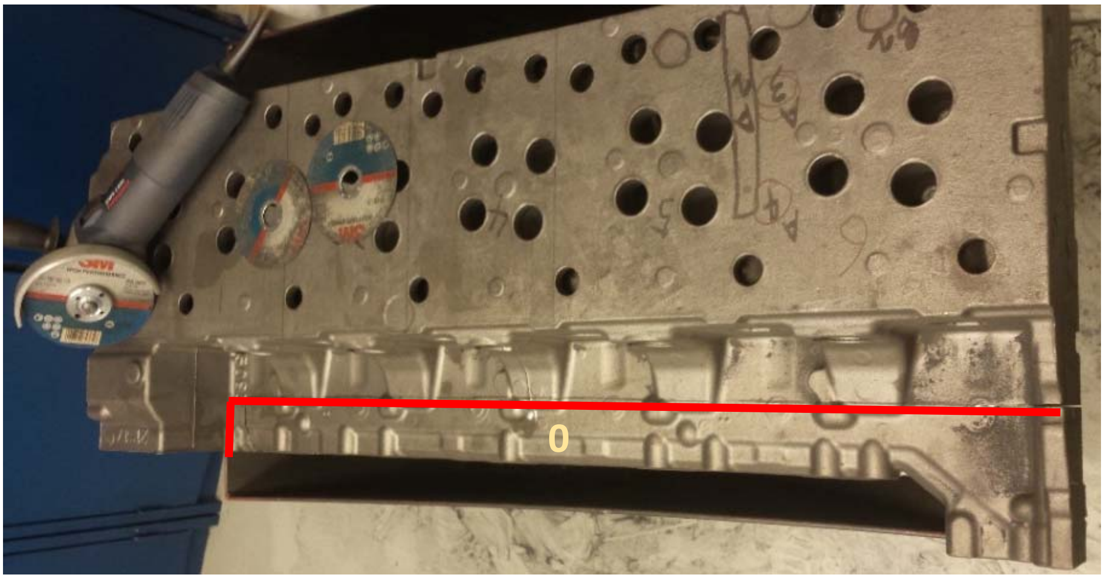

Figure 22. Section zero of excess material was cut off by an angle grinder at the red line.

The cylinder head was then cut into six sections, one for each cylinders seen in Figure 23. Each cylinder section was cut into an A-part and a B-part.

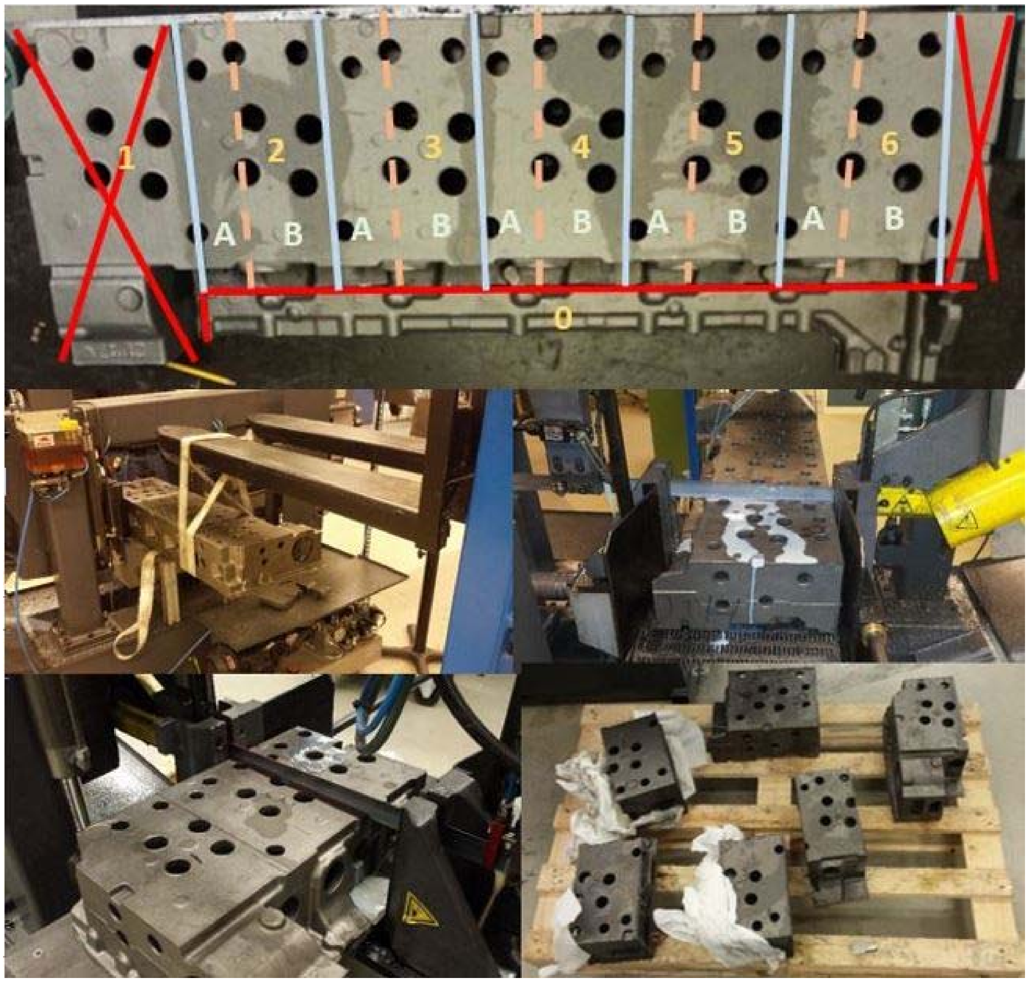

Figure 23. Sectioning of the cylinder head using the bandsaw Bomar Proline 320.280 H.

From each of the five cylinder sections four specimens were extracted from part A and two from part B making a total of 30 specimens. The rectangular cuboid shaped specimens, roughly 20x20 mm in cross section and a minimum length of 110 mm, were then roughly lathed down to cylindrical bars with diameters of 12 mm, as seen in Figure 24. The rotational speed of the lathe was set to 840 rpm and the feeding speed was set to 0.14 mm/revolution. To be able to get the full length of the tensile bars they had to be flipped around and lathed on the full length. The shape of the final tensile test bars were made according to the Volvo standard [46] with the help of a CNC-lathing machine. The top and bottom end still with the diameter of 12 mm with a 50 mm long necking with diameter 7 mm. The transit radius between the necking and the two edges was set to 5 mm as seen in Figure 24.

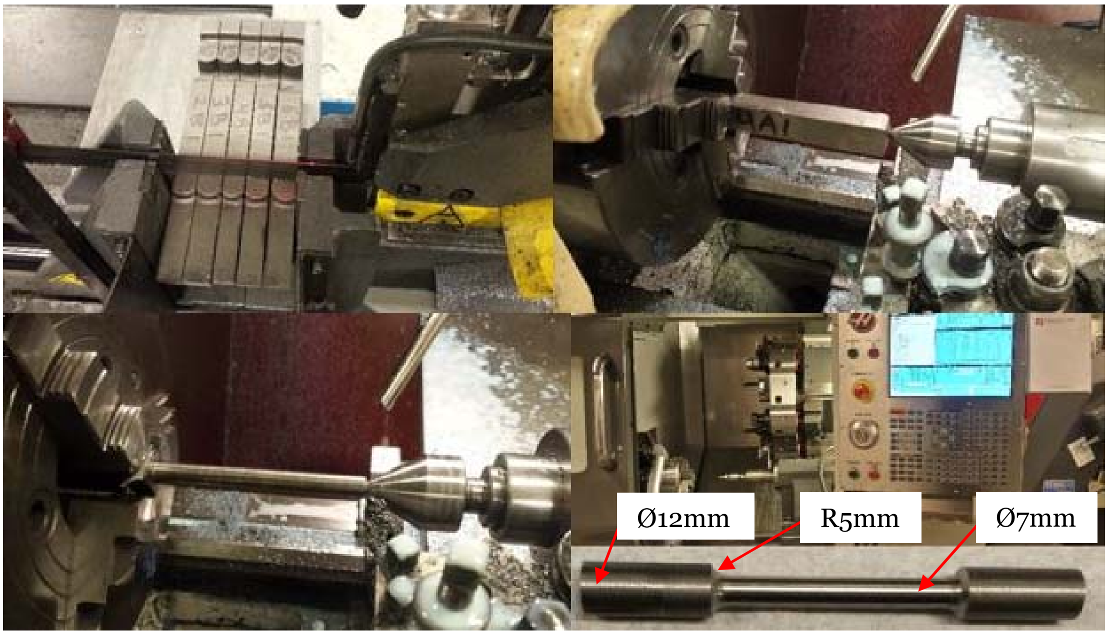

Figure 24. The tensile test bars were cut into rectangular cuboids which were then lathed to cylinders and given its final shape with the necking in a CNC-lathe machine.

To be able to keep track of all the 30 final shaped tensile bars, names were given to them based on:

- cylinder section number, (2-6)
- part A or B
- specimen placement number

For example, specimen named 6B2 explains that it is extracted from cylinder 6, part B with the placement number 2. The location of all samples in the cylinder head can be seen in Figure 27.

3.2.2 Physical property sample extraction

Samples were also needed for the physical property tests, dilatometer test to measure thermal expansion, differential scanning calorimetry testing to determine the specific heat and laser flash apparatus testing to measure thermal diffusivity. All these test procedures have been described in section 2.5. The purpose of the physical testing was to test the material's thermal properties at different locations, solidifying at different rates, in the component. It was decided to test at three different solidification times; fast, intermediate and slow, and with a sample size of three for each solidification condition making a total of nine physical test locations. These locations were determined by studying images from casting simulation performed in MAGMA[47] of the cylinder head showing the solidification times in sections throughout the whole component, see Figure 25. The three different solidification times were chosen to be:

- Fast solidification – around 200 seconds.
- Intermediate solidification – around 600-700 seconds.
- Slow solidification – around 1700-1800 seconds.

The three samples from the intermediate solidification were taken at the surface of the cylinder head which is in direct contact with the cylinder block, which is the source of the heat. The physical properties of the material at this location were of great interest for the manufacturer, Volvo. The three samples from the slow solidification was taken from the center of the component. These six samples, from slow and intermediate solidification, were taken from cylinder section 3, 4 and 5 and after the mechanical sample extraction was finalized it was clear that the best decision was to take the physical test samples from part B which still had a lot of material to take samples from. The three samples from the fast solidification were taken next to each other from the thin section named "0" in Figure 23. The physical test samples were named in accordance with the naming of the mechanical test samples only adding an F, representing physical, at the end. The location of the physical samples can be seen in Figure 25.

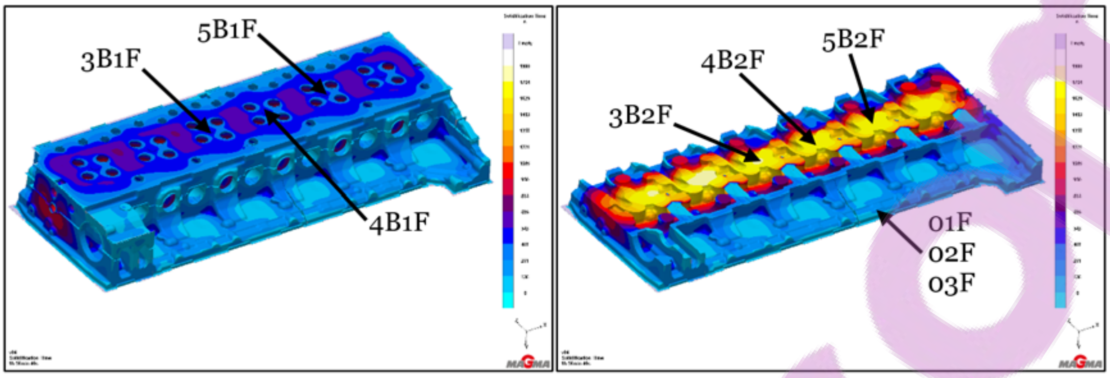

Figure 25. Solidification time of the cylinder head from a casting simulation made by Volvo and arrows showing the locations of the physical test samples.

A rectangular cuboid piece was cut out for each of the six physical test samples and they were then lathed to their final dimensions. The sample dimensions, in accordance to the test equipment's guidelines, for the three tests were as follows:

- DIL – cylindrical rod with 6 mm in diameter 12 mm in length
- DSC – cylindrical disc with diameter 4 mm and 1 mm in thickness
- LFA – cylindrical disc with diameter 12.5 mm and 4.375 mm in thickness

The different samples can be seen in Figure 26. The samples for DIL and LFA were cut out from the lathed piece in the lathing machine, leaving a small stub that was then grinded off, as seen in Figure 26. The sample for the DSC were not taken at different locations due to the reason that the specific heat of the material is independent of the casting conditions which means that it will not wary within the component. They were instead all taken from one single lathed rod and cut out using a low speed saw, as seen in Figure 26.

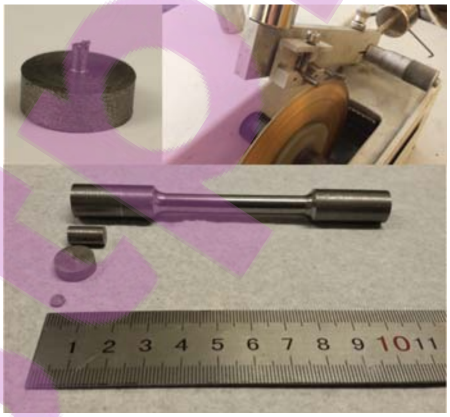

Figure 26. The cutting in the lathe left a small knob that had to be grinded off. Slow speed saw for DSC samples. All different test samples.

All the samples extracted, both for mechanical and physical property testing, are shown in Figure 27, they are:

- Samples for mechanical testing:
    - A1 – Turquois
    - A2 – Grey
    - A3 – Green
    - A4 – Orange
    - B1 – Black
    - B2 – Purple

- Samples for physical testing:
    - 1F – Yellow
    - 2F – Red
    - 0F – Blue

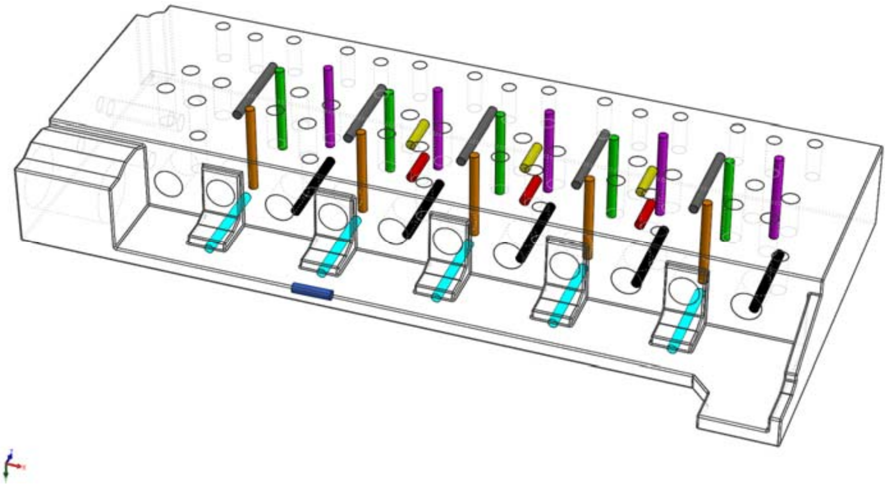

Figure 27. Locations of the test specimens. The long cylindrical bars represent the locations for mechanical testing and the short cylindrical bars represents the samples for physical testing.

3.3 Testing

The material property testing of the cylinder head consisted of the testing procedures introduced in section 2.5. The testing was both of mechanical and physical properties.

3.3.1 Mechanical property testing

The mechanical property testing in this thesis consisted of tensile testing since it was used in test the two previous cylinder heads.

Tensile testing

The tensile test was performed at room temperature at JTH test lab using the Zwick/Roell Z100 tensile testing equipment which has a load capacity of 100 kN. The strain elongation on each tensile bar was measured with a laser extensometer. The tensile testing was executed to be able to collect the mechanical properties at various locations of the cylinder head. The proceeding steps were roughly as follows:

- Measuring the tensile bars
- Configure the software parameters
- Execute the tensile tests
- Collect the data given

The software used when performing the tensile tests needed the input value of the minimum diameter of the necking section of each tensile bar. The measurements were taken in three different areas of the 50 mm necking section, at the bottom area, in the middle and at the top area as could be seen in Figure 28. This was done in order to investigate if the fracture occurred where the tensile bars had the minimum diameter.

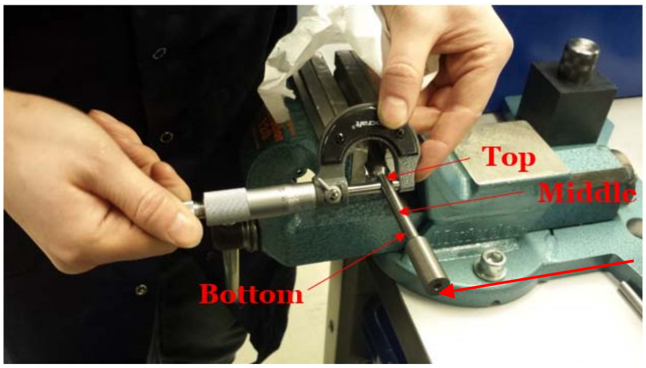

Figure 28. The tensile test bars were measured at three locations on the necking, at the top, the middle and at the bottom.

All parameter settings were then configured into the software to fit the settings from the previously projects performed by Stark & Gustavsson [5] and M.Li [4]. The grip pressure of the tensile bar holders was set to 200 bar to make sure that the tensile bar did not slip when pulled as seen in Figure 15. The gauge length distance of the laser extensometer was set according to the Volvo standard [46] getting readings with a distance of 35 mm apart. The crosshead rate was set to a constant speed of 0.5 mm/min with a preload of 200 N.

One of the samples was destroyed while performing the tensile test and therefore the data from sample 3A4 is missing. After each test the data was collected from the stress-strain curve provided from the software.

3.3.2 Physical property testing

Four different tests, described in section 2.5, were performed to measure the material's physical properties.

Dilatometer testing

The thermal expansion of the samples was measured by a Netzsch DIL 402C push-rod dilatometer, as seen in Figure 16. Due to technical problems with the machine, only six samples were measured, the three from slow solidification and the three from intermediate solidification. This is discussed further in section 5.1.2. The heating chamber was emptied of its air, creating a vacuum, and then filled with Helium gas. This process was done three times to ensure a high enough fraction of Helium in the atmosphere in the heating chamber. The testing was performed at two different occasions, each time doing a standard sample test, with a 12 mm long polycrystalline Al_2O_3 rod, before testing the material samples. At the first occasion samples 5B2F, 4B2F and 3B2F was tested and then the other three were tested. The testing was run from room temperature up to 500°C with a heating rate of 10 K/min. All samples were measured before testing and their lengths can be found in Appendix 1.

Density testing

The density was measured of the six samples made for the LFA testing before the LFA tests. The density was determined using the method described in section 2.5.2 using a KERN ABJ analytical balance as seen in Figure 17.

DSC testing

The specific heat measurement was performed using a Netzsch DSC 404 C as seen in Figure 19. The measurements were made from room temperature up to 500 degrees with a heating rate of 10 K/min. The atmosphere in the heating chamber was composed of Argon gas with a constant gas flow of 85 ml/min after the atmosphere was set to vacuum three times, just like for the dilatometer. In the first run, the correction run, the two crucibles were empty. In the second run, the standard run, one crucible was empty and one contained a standard sample of synthetic sapphire, α-Al_2O_3. Then the three samples were run successively with one empty crucible and one crucible with a sample. The sample were first weighted and their mass was entered into the DSC computer program. Their mass can be found in Appendix 2.

LFA testing

Thermal diffusivity was measured at 25, 100, 200, 300, 400 and 500°C using a Netzsch LFA 427 as seen in Figure 20. Five laser shots were made at each temperature. The atmosphere in the heating chamber was composed of argon gas with a constant heat flow of 50 ml/min after the atmosphere was set to vacuum. The samples were sprayed with a thin layer of graphite to get a non-reflective surfaces for the laser. The laser voltage was set to 450 V and the pulse width was set to 0.8 milliseconds. The IR-detector which measures the surface temperature of the sample was cooled using liquid nitrogen. Each sample was measured using a micrometer and their thicknesses were entered into the LFA computer program which can be found in Appendix 3.

3.4 Sample preparation for optical microscope analysis

To enable the image analysis of the microstructure some of the samples were strategically selected to be prepared before they could be observed in an optical microscope. The preparation comprised the following steps:

- Extracting samples from mechanical tested samples
- Extracting samples from where the physical tested samples were taken
- Imbedding the samples in plastic
- Grinding and polishing the surfaces

3.4.1 Extracting samples from mechanical tested samples

The validation of the data provided from previously completed projects required samples of the third cylinder head to be extracted from the same six locations as for the first and second cylinder head. From these six samples images of the microstructure were already captured and documented. The samples selected were as follow:

- 2A3
- 2A4
- 3A3
- 3A4
- 3B2
- 6B2

The samples were extracted using an angle grinder machine with coolant. Each tensile bar was cut as demonstrated in Figure 29 where the red lines specifies the sample section.

Figure 29. Sample section from tensile bar.

3.4.2 Extracting samples from where the physical samples were taken

The physical property testing had not been investigated in the previously completed projects and therefore no previous documentation was to be considered. All locations where the physical testing were performed were selected to undergo the image analysis.

When extracting the samples to be used in the dilatometer an extra cylinder was cut out from each location. The cylinder shaped rod was also of the length 12 mm and had a diameter of 6 mm. The extra cylinders were used instead of the samples that had undergone the heat expansion testing in the dilatometer.

3.4.3 Embedding samples

The embedding of both the mechanical and the physical samples were performed to be able to easier analyze the surfaces in the optical microscope. The diameter desired of the samples was set to be 30 mm. The equipment used for embedding the samples was a Struers citopress-1 as seen in Figure 30.

Figure 30. Embedding equipment used, Struers citopress-1 with a close up on the cylindrical piston to put the sample.

First the samples needed a flat surface to put on top of the cylindrical piston seen in Figure 30, in the machine, which meant that some samples needed a quick grinding before proceeding. The piston together with the sample was then lowered approximate 20 mm, this was done to enable the filling of the black thermosetting phenolic hot mounting resin called Multifast, used to embed the samples, displayed in Figure 31.

Figure 31. Multifast, the phenolic hot mounting resin used.

The first scoop of Multifast was poured in before the piston was lowered to the final stand. For each sample approximately 2.5 to 3 tablespoons were poured in to embed the whole sample. A lid was then put on to enclose the chamber where the sample was put.

Before starting the embedment, the software input parameters needed to be configured, e.g. the length of the heating time, the length of the cooling time, the heating temperature, the pressure and the cooling rate. A 3-minute heating time at 180 degrees with a pressure of 25 MPa and a 2-minute-long cooling time at a high cooling rate was used. This was enough to make the plastic set properly according to a tablet template used for Multifast.

The finished embedment was then marked with an inscription pen on the side so it would be easy to find the correct sample. The finished embedment together with the inscription pen used can be seen in Figure 32.

Figure 32. Embedded sample completed with inscription on the side.

3.4.4 Grinding & Polishing samples

The surfaces of the embedded samples were still too rough and in need of some further work before they could be observe in the optical microscope. This further work consisted of grinding and polishing steps. The equipment used for this task was a Struers Tegramin-30 that could grind and polish up to six samples at the same time using a sample holder as seen in Figure 33.

Figure 33. Equipment used for grinding and polishing, Struers Tegramin-30 with a sample holder for six samples.

The discs used had the size of 300 mm and were designed for plane grinding or polishing of materials with HV 150-2000. The grinding involved six different steps using grinding discs with small resin bounded diamonds with decreasing coarseness. Other important input parameters configured into the software were e.g. the time, lubrication used, pressure added on the samples, rotation direction and speed of the samples and the disc as seen listed below:

- **Step 1 -** Diamond grit 250, 5 minutes, addition of water, pressure of 30 N, disc rotating counter clockwise and samples clockwise with a speed of 150 rpm.
- **Step 2 -** Diamond girt 500, 4 minutes, addition of water, pressure of 30 N, disc and samples rotating counter clockwise with a speed of 150 rpm.
- **Step 3 -** Diamond grit 1200, same input parameters as step 2
- **Step 4 -** Diamond grit 2000, same input parameters as step 2
- **Step 5 -** Diamond grit 4000, same input parameters as step 2
- **Step 6 -** Diamond grit 4000, 3 minutes, addition of water, pressure of 10 N, disc and samples rotating counter clockwise with a speed of 150 rpm.

After each step the samples were taken out from the grinding machine to be washed with water to make sure no large particles would follow to the next step. If this had happened the larger particles could make scratches in the surface and the procedure would need to start over from the beginning. Also the sample holder was taken out and cleaned before a new step could start.

The grinding steps were followed by two polishing steps with the same input parameters to be configured as before, but instead of using grinding discs two different types of polishing cloths were used. With these polishing cloths a water based diamond suspension with cooling lubricant was added instead of only water. The polishing steps and the parameters can be seen listed below:

- **Step 1 –** Dac-Cloth disc, 1 minutes, addition of diamond suspension (3 µm), pressure of 15 N, disc and samples rotating counter clockwise with a speed of 150 rpm.
- **Step 2 –** Nap-Cloth disc, 1 minutes, addition of diamond suspension (1 µm), pressure of 20 N, disc and samples rotating counter clockwise with a speed of 150 rpm.

As for the grinding steps the samples were washed in water before and after each step. The only difference with the polishing steps was that the samples were also washed with ethanol and cleaned with an ethanol soaked cotton ball afterwards. The samples were then dried using hot air to ensure the sample did not start to oxidize.

The whole procedure was performed on the six selected mechanical tested samples and the nine physical tested samples. Due to insufficient data regarding the second cylinder head the procedure was also performed on the six, already imbedded, selected mechanical tested samples from the second cylinder head.

3.4.5 Etching samples

To confirm that the grey iron cylinder head used in this project contained a matrix with a pearlitic structure, as was to expect, it was necessary for the samples selected to be etched. The etching procedure was performed after pictures were taken of the graphite microstructure in the optical microscope.

The etchant used for the samples was a 2 % Nital solute that contains alcohol (ethanol) and nitric acid (HNO_3) which is the most commonly solute used for cast irons. The 2 % is referring to the weight percentage nitric acid in the solute. The etching procedure is revealing the alpha grain boundaries and constituents together with the cooperative lamellar growth of ferrite and cementite that makes the pearlitic structure.[48]

The samples selected to endure the etching process were six of the selected for the physical testing as listed below:

- 3B1F – Etched
- 4B1F – Etched
- 5B1F – Etched
- 3B2F – Etched
- 4B2F – Etched
- 5B2F – Etched

The etching procedure was started by pouring the 2 % Nital solute into a watch glass. The samples were later immersed into the solute just enough to cover the whole surface area and kept there for 20 s. To stop the etching reaction, the surfaces of the samples were washed with ethanol and finally dried with hot air as seen in Figure 34.

Figure 34. Etching procedure consisting of immersing samples in a 2 % Nital solute.

3.5 Microstructure analysis

The analysis of the microstructure of the material consisted of taking images in an optical microscope, images which were then analyzed in a computer software to quantify the graphite particles.

3.5.1 Optical microscope analysis

In order to investigate the microstructure of the selected samples, images were captured using an optical microscope, the Olympus GX71 seen in Figure 35. This equipment together with the provided software, Stream Motion [49], enabled a mixture of settings and features.

Figure 35. The optical microscope, Olympus GX71, used to capture images of the microstructure.

Unetched samples

The microscope parameter settings used for the unetched samples, e.g. the magnification and the bright field mode, were set constant for all images captured. The images produced provided a resolution of about 3746 x 2778 pixels. According to a previous research regarding shape analysis of graphite [50] the magnification was set to x10 providing a sufficient digital resolution with a pixel size around 0.55 µm. The bright field mode was set to a value of 10. The focus was set manually for each image in order to get the best result. In all the samples images were captured at three different locations as can be seen in Figure 36.

Figure 36. Illustrating the three locations where images were captured within the samples.

In order to get measurements from a larger surface area, four pictures were captured at each location and merged together using a multi-snapshot feature. The multi-snapshot feature allowed the user to produce a start image and then select the direction in which the next image to merge should appear. A calibration was required to be made manually in order to fit the borders of the images, an overlap, indicated by the red arrows in the upper left corner of Figure 37, of approximately 2 cm made this easier. As can be seen in Figure 37 the second image is placed above the start image. The third image was placed to the right-hand side of the second and the fourth just below the third.

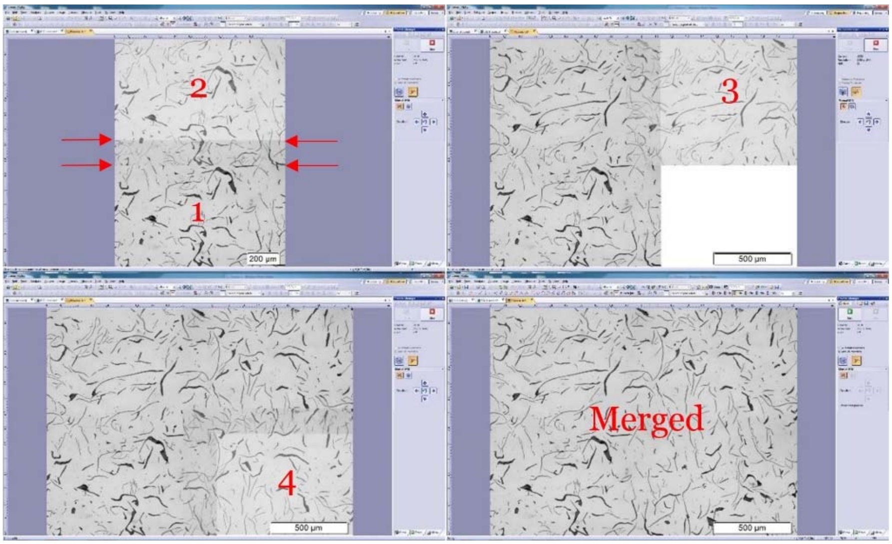

Figure 37. The multi-snapshot procedure merging together the four images in the computer software Stream Motion[49]. The red arrows indicate the overlap required to calibrate.

The procedure was performed on the six selected mechanical tested samples of the second and third cylinder head and the nine physical tested samples of the third cylinder head.

Etched samples

With the intention to determine the matrix structure as pearlitic six of the physical tested samples were investigated. Two images were captured of each etched sample, one overview with a magnification of x20 providing an image with a digital resolution of about 3750 x 2775 pixels and one image with magnification x50 providing a digital resolution of about 2080 x 1544 pixels. The capturing of the overview images followed the same procedure as the unetched samples while the images taken with x50 magnification only were captured with a single snapshot instead of four merged images. The bright field mode was set as for the unetched samples to a value of 10. The focus was also set manually for each image in order to get the best result. Since only ocular analysis was needed to establish if the microstructure was pearlitic or not, no further analysis was done with these samples.

3.5.2 Image analysis

To quantify the amount of graphite, the graphite fraction, and the sizes and form of the graphite flakes the images from the optical microscope were analyzed using an image analyzing computer software called Stream Motion Desktop [51]. The graphite size and form was determined using the Cast Iron module in the software, as seen on the left in Figure 38. The threshold for graphite, i.e. the darkness of the graphite particles needed to be included in the analysis, was then set using a sliding scale as seen to the right in Figure 38.

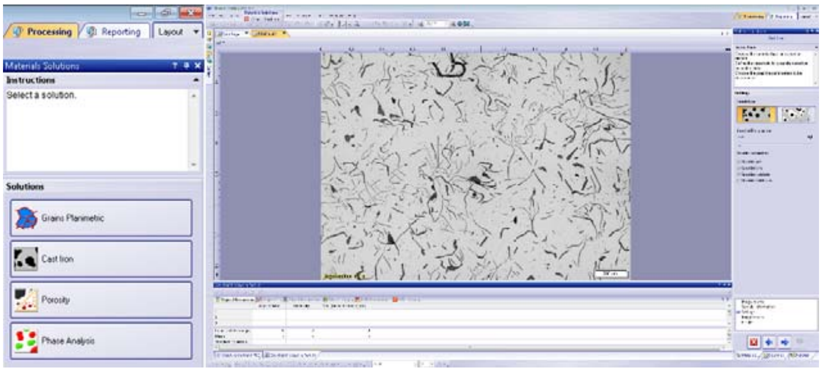

Select a solution.

Figure 38. The modules in the image analysis software and the threshold sliding scale.

A too low threshold value, as seen in the top left in Figure 39, will mean that too little amount of graphite particles will be included in the analysis, i.e. only the very darkest regions. On the other hand, a too high threshold value, as seen in the top left in Figure 39, will mean that too much of the matrix surrounding the graphite particles will be included in the analysis. A good threshold value, as seen in the two pictures in the bottom in Figure 39, will result in all, or close to all, of the graphite particles and no matrix will be included in the analysis.

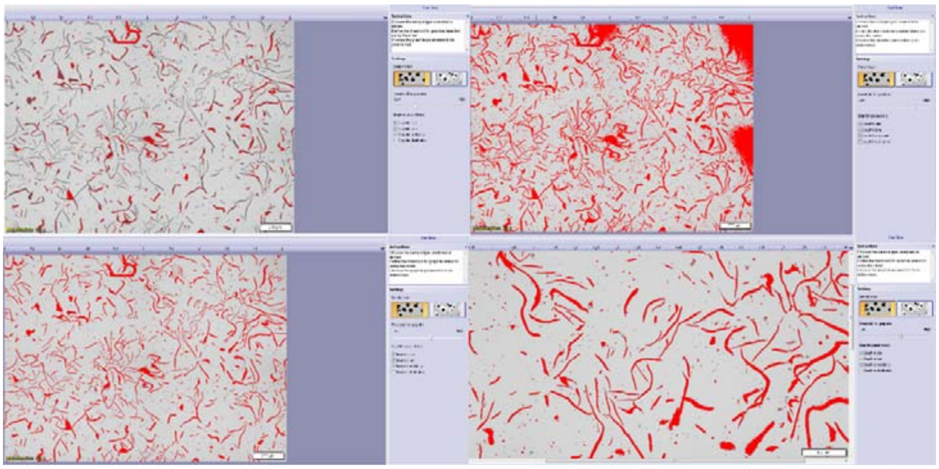

Figure 39. Threshold regulation for determining graphite size and form. Top left: too low threshold value, top right: too high threshold value, bottom left: good threshold value and bottom right: zoomed in on the graphite particles marked with red using a threshold value.

The software then analyses the graphite particles that have their entire shape within the border of the image and classifies them in three different ways as seen in Figure 40, top: graphite size, bottom left: graphite form and bottom right: graphite nodularity. The graphite size chart classifies the graphite particles by their size class as seen in Figure 4 and Figure 5 in section 2.2.2. The graphite form chart indicates that most of the particles are of type VII which is also referred to as flake graphite [6]. Some particles are also classified as type III, which is also called temper carbon, and type IV, which is also called vermicular graphite. This might however not have to be the case; the three dimensional graphite particle can be oriented in a way that in this two dimensional section they only appear to be of that form while in reality they might be flake shaped.

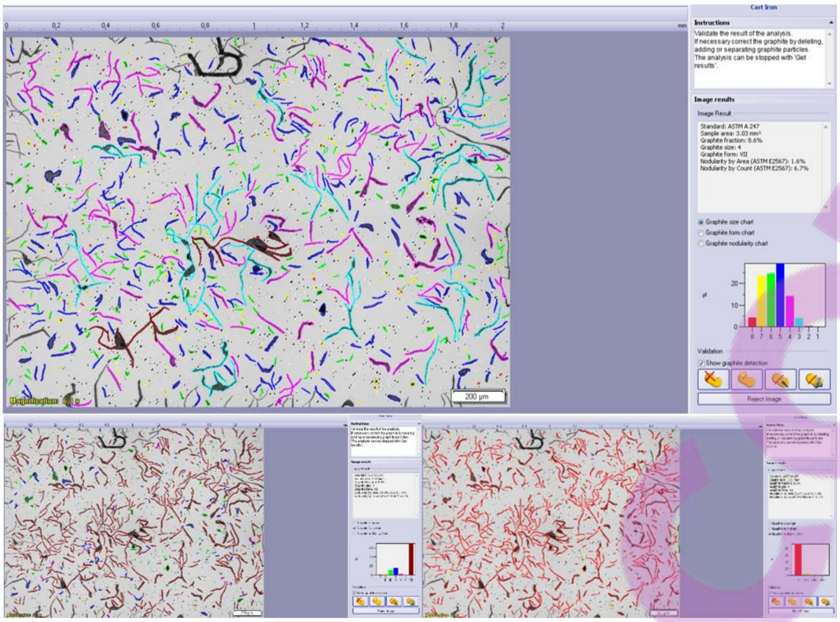
Cast Iron

Instructions

Validate the result of the analysis.
If necessary correct the graphite by deleting, adding or separating graphite particles.
The analysis can be stopped with 'Get results'.

Image results

Image Result

Standard: ASTM A 247
Sample area: 3.03 mm²
Graphite fraction: 8.6%
Graphite size: 4
Graphite form: VII
Nodularity by Area (ASTM E2567): 1.6%
Nodularity by Count (ASTM E2567): 6.7%

● Graphite size chart
○ Graphite form chart
○ Graphite nodularity chart

Validation

☑ Show graphite detection

Reject Image

Figure 40. Image results from the analysis. The graphite particles are grouped by; top: graphite size, bottom left: graphite form and bottom right: graphite nodularity.

To exclude non-graphite particles, e.g. TiCN and MnS [15], some particles had to be removed manually as seen in Figure 41. The result from the image analysis is a spreadsheet containing information about each particle, the area, the maximum Feret diameter, i.e. the largest distance between two perpendicular planes that the particle can be contained within, and the perimeter length.

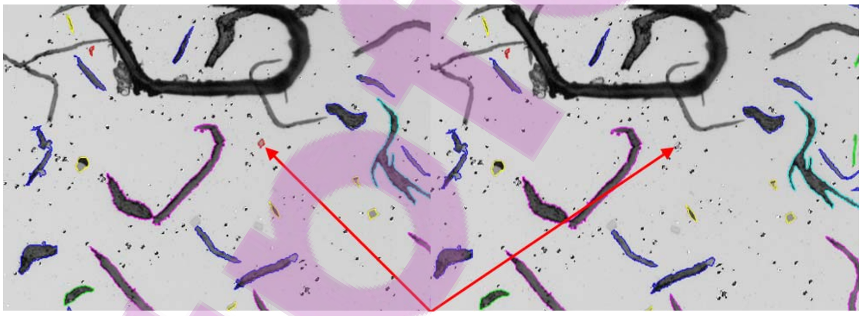

Figure 41. Example of a small non-graphite particle removed manually from the analysis.

The Cast Iron module also shows the graphite fraction, however, since the graphite particles that goes outside the image border is excluded from the analysis the graphite fraction shown is lower than it should be. The Phase Analysis module in the software was therefore used to determine the graphite fraction. A good threshold value for including only the graphite particles was then used, a threshold of 180-185 was found to be the best for most of the samples.

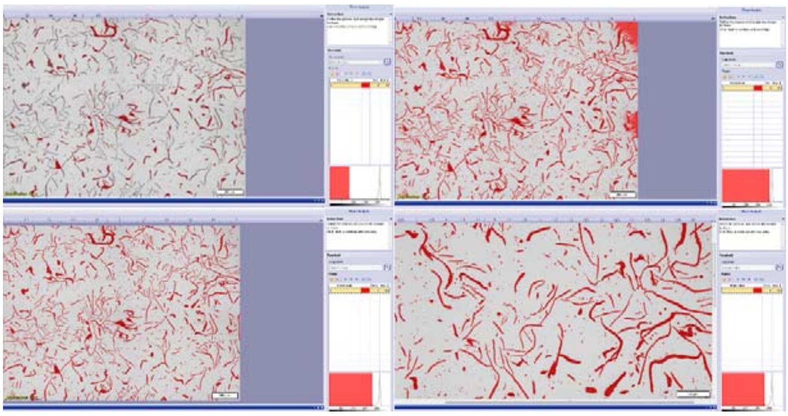

Figure 42. Threshold regulation for determining graphite fraction. Top left: too low threshold value (81), top right: too high threshold value (200), bottom left: good threshold value (180) and bottom right: zoomed in on the graphite particles marked with red using a threshold value.

To filter out small particles that are not graphite, e.g. the MnS and TiCN particles, a minimum object area was then defined. A good value for that was found to be 50 µm² which was used in most the images from the samples. Figure 43 shows how different values for the minimum object area were examined.

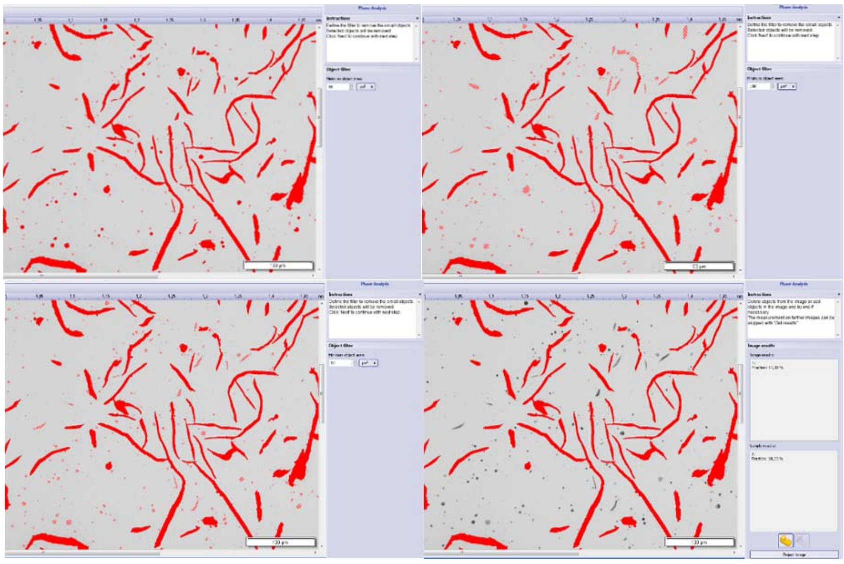

Figure 43. Small particles were filter out from the analysis. Pink particles are excluded and red particles are included in the analysis. Top left: too low minimum object area (20µm²), top right: too high minimum object area (100µm²), bottom left: minimum object area (50µm²) and bottom right: showing the graphite fraction and the excluded particles in grey.

3.6 Connecting casting simulation and FE software

A FEA of a simplified working condition of the cylinder head were performed with homogeneous material definition and with local variations to compare the results. The simulations were made using the experimentally determined physical properties. Also simulations were made using extreme values of thermal conductivities of grey iron found in the literature [25] to better see the difference when using local material definition. A methodology to connect casting simulation and FE software using local physical properties data has been worked out and is explained in this section and is illustrated in Figure 44.

CTE ρ C_p λ

Figure 44. Flowchart of the methodology worked out to connect casting simulation and FE software using local physical properties data.

3.6.1 Design of simplified geometry

A simplified geometry of the complex cylinder head was designed in SolidWorks [52] as seen in Figure 45. The simplified geometry has the same outer dimensions as the real component but without all the intricate internal cavities that the real geometry has which makes the FE-meshing easier and saves time.

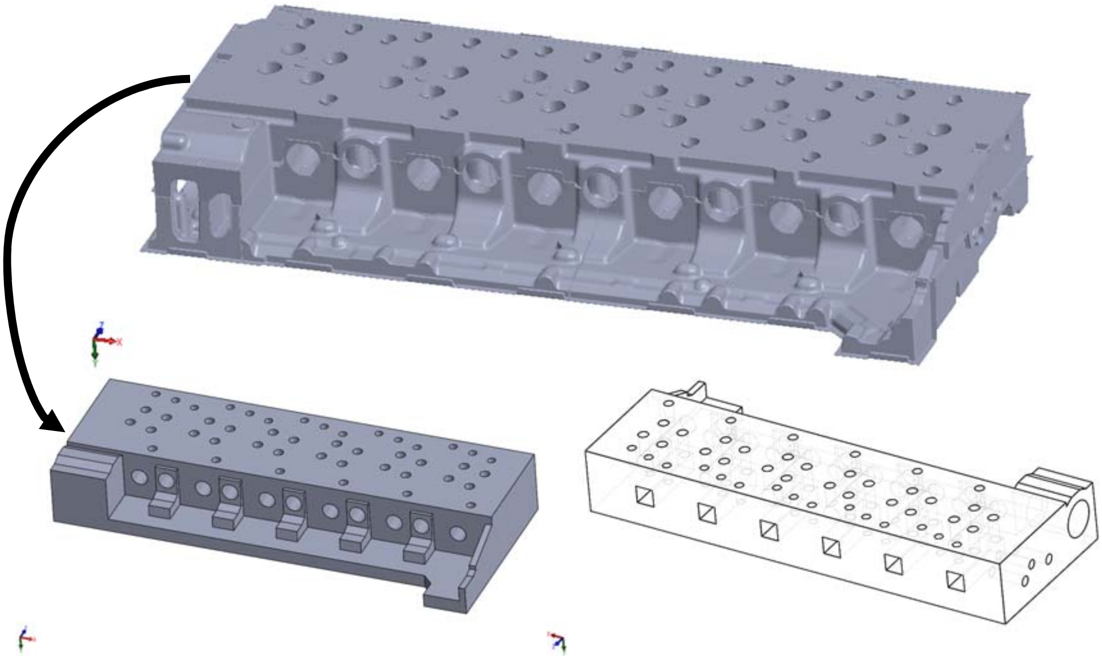

Figure 45. The top image shows the real geometry of the cast cylinder head pre machining. The simplified geometry of the cylinder head used in the simulations in this thesis is shown in the lower images.

3.6.2 Setting up the FE-model

The simplified geometry was imported into Abaqus [53] where a finite element mesh was generated of the part consisting of around 300 000 solid tetrahedral elements. The mesh can be seen in Figure 46. A pinned boundary condition (BC) was set on the surface of the cylinder head which is mounted to the cylinder block, as seen in Figure 46. In the initial step the whole cylinder head was set to be 25°C and then circular areas around the 4 holes, connected to the intake and exhaust, on each cylinder was set to rise linearly to 400°C, which is approximately the working temperature for the component.

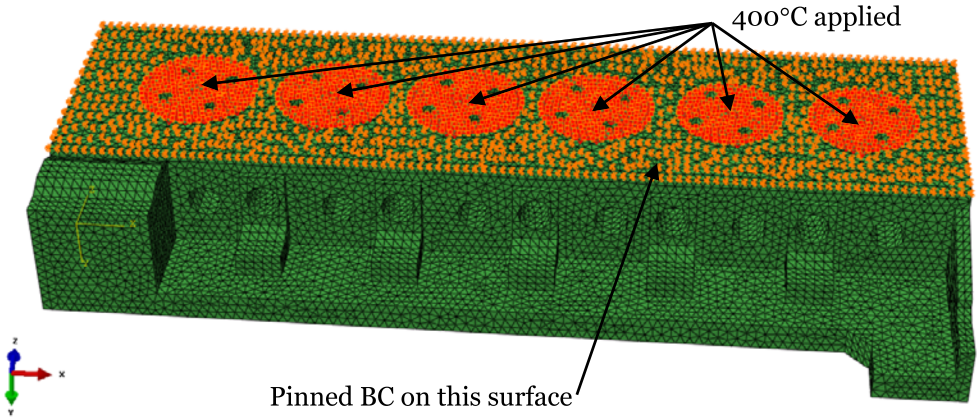

Figure 46. Circular areas on the cylinder head were a temperature rise to 400°C were applied. The surface connected to the cylinder block was given a pinned boundary condition.

In order to compare the results from the simulation with homogeneous material definition to the one with the local variation the temperature in six selected nodes were measured during the simulations. The nodes were selected from a cross section view in the middle of cylinder 3 and the six nodes were numbered according to Figure 47 with node number 1 closest to the surface with the applied temperature load and node number 5 just below the opposite surface. Node number 6 was placed in the thin section, section 0 in Figure 22, where the solidification time is the shortest.

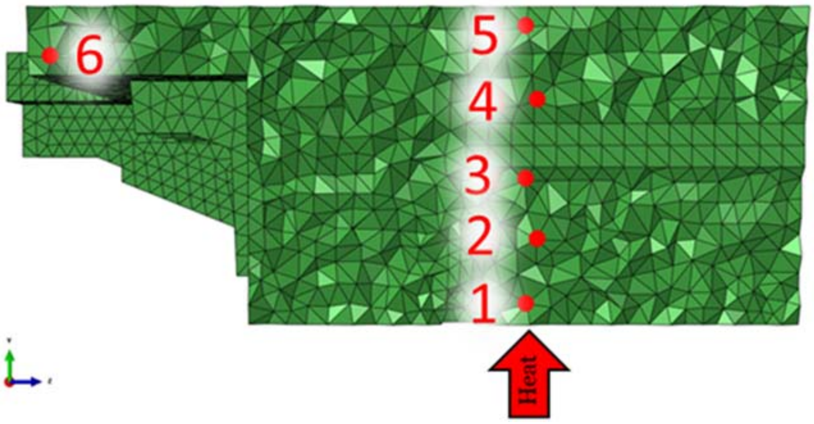

Figure 47. Six nodes for temperature curves were selected in a cross section view in the middle of cylinder 3.

3.6.3 Casting simulation

The simplified geometry was imported into MAGMA [47] where a casting simulation of the geometry was run. The set-up of the simulation correlated to the casting simulation of the real geometry used by Volvo. Only the solidification, i.e. not mold filling, was included in the simulation since only the solidification was of interest. The mesh used in the casting simulation consisted of around 12 million elements. The solidification times from the casting simulation of the simplified geometry can be seen in Figure 48. The solidification times are higher than for the real geometry, a maximum of around 4200 s in the center compared to around 1300 s as seen in the casting simulation of the real geometry in Figure 25.

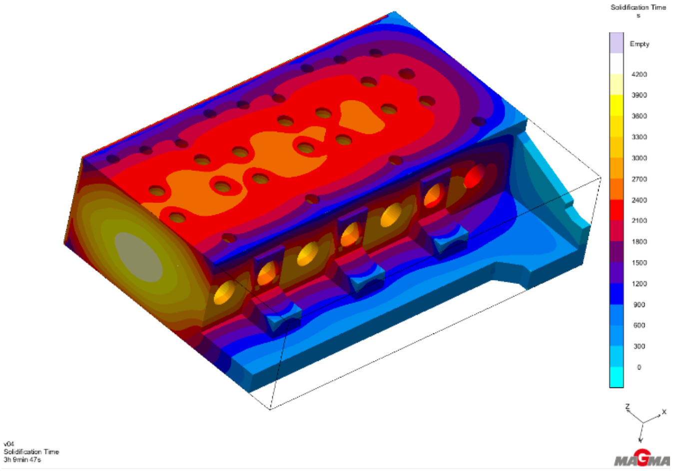

Figure 48. Cross section of the simplified geometry of the cylinder head showing the solidification times results from the casting simulation in MAGMA.

3.6.4 Connecting experimental results to casting simulation results

The experimental values of the physical properties measured in this thesis, see section 3.3.2, were then connected to the casting simulation in MAGMA using user result definitions. These results thereby got included in each of the 12 million elements. The physical property that was found to have local variation was set to linearly vary from the lowest solidification time to the highest solidification time. The physical properties that were found to not have local variations were set as constants. The mechanical properties did not affect the simulation results that were of interest, i.e. the temperature distribution, but were set as constants in order to be able to run the FEA.

3.6.5 Mapping the casting simulation results to the FE-mesh

The FE-mesh was imported as an input file from Abaqus into MAGMA using the MAGMAlink module in MAGMA. The values of the physical properties were mapped from the casting simulation mesh to the FE-mesh and saved as individual file for each property with a values for each element in the FE-mesh. The local material properties were then combined and imported into the Abaqus input file using a Python script developed by J. Olofsson. The input file then contains one material definition for each element in the FE mesh and thus includes the local variation of physical properties.

3.6.6 FEA

The simulation run in Abaqus was an implicit dynamic coupled temperature displacement simulation where the temperature on the circular areas seen in Figure 46 were set to rise from 25 to 400°C and the total simulation time was set to 1000 s. Four simulations were run in total:

- Experimental values – homogeneous material
- Experimental values – local variation of thermal conductivity
- Extreme values – homogeneous material
- Extreme values – local variation of thermal conductivity

4 Results & Analysis

The results followed by analyses of the results are presented in this chapter. Many of the results are also presented with a mean value, μ, i.e. average value, of several samples. Along with the mean value a standard deviation, STDEV or σ, is also calculated using the formula for standard deviation of a population, STDEV.P [54].

$$\sigma = \sqrt{\frac{1}{N} \cdot \sum_{i=1}^{N} (x_i - \mu)^2} \tag{31}$$

The coefficient of variation, CV, which is also known as the relative standard deviation, is also calculated and presented. CV is simply the fraction between the standard deviation and the mean, σ/μ.

4.1 Mechanical test results

The data extracted from the tensile test were imported into a Matlab [55] script to generate tables and stress-strain diagram with the properties of e.g. ultimate tensile strength, yield strength and Young's modulus (E). The values e_b and e_p represents the maximum engineering strain at fracture and the maximum plastic strain respectively. The script also provides the values for the strain hardening exponents n_H and n_L and the strength coefficients K_H and K_L as seen in Figure 49, which are used to calculate the Hollomon and Ludwigson equations, equation (7) and (8). Those equations are then being used to model the tensile test curve. In Figure 49 the Hollomon, K_H and n_H, parameters are determined in the plastic strain interval 0.002-0.01 (0.2 % to 1 %) while the Ludwigson parameters, K_L and n_L, are determined in the interval 0.0005-0.002 (0.05 % to 0.2 %). In Figure 50 the true stress-strain is shown, modelled using only the Hollomon equation with the plastic strain interval 0.0005-0.01 (0.05% to 1 %).

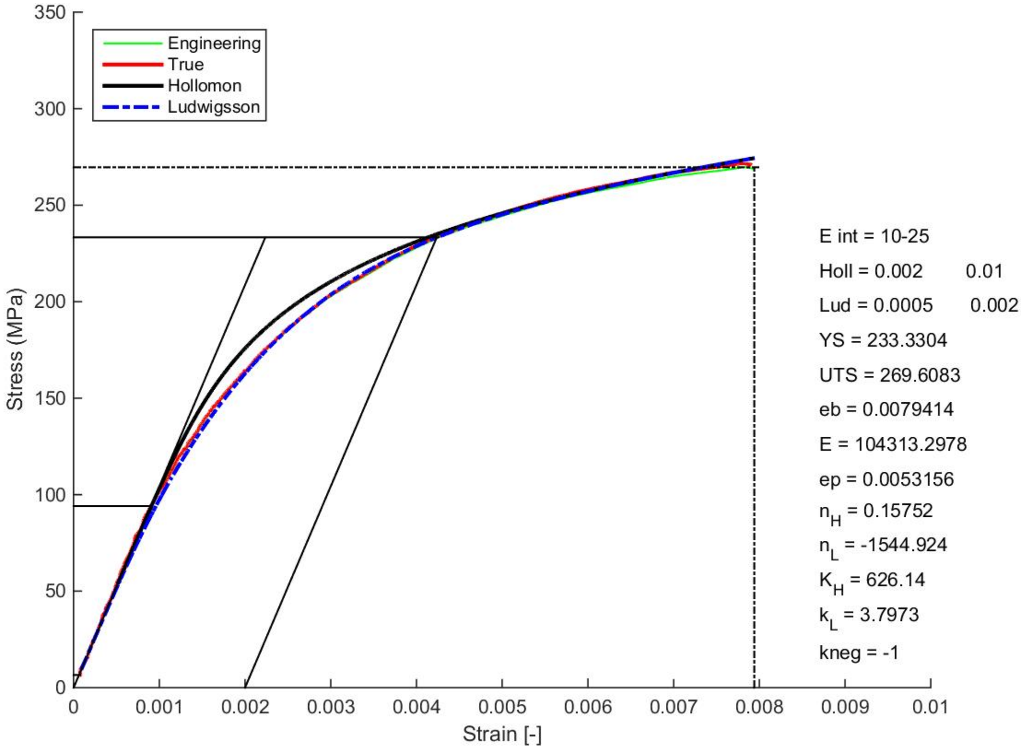

Figure 49. Example of a stress-strain diagram for the sample 4A1 with all mechanical properties generated by the provided Matlab script. The red line shows the true stress-strain curve from the tensile test, the green line shows the engineering stress-strain curve and the black and blue line shows the modelled curve from the Hollomon and Ludwigson equations respectively.

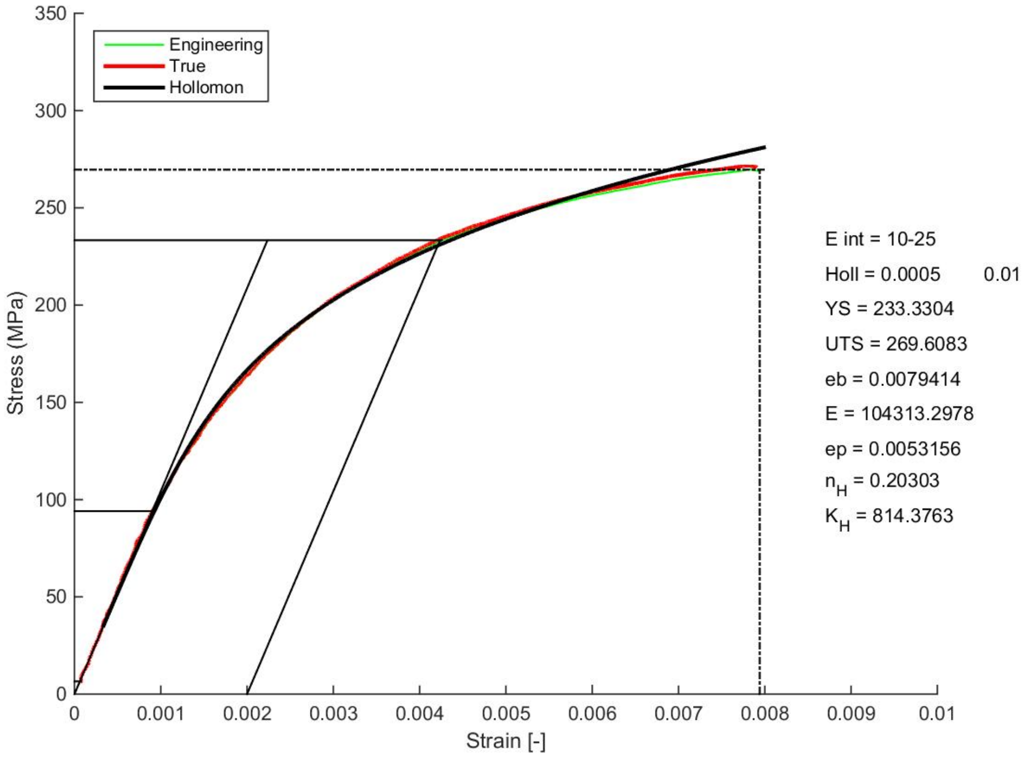

Figure 50. Stress-strain diagram of the same sample, 4A1, as in Figure 49 but with only the Hollomon equation modelled to fit the true stress-strain curve.

As seen in Figure 49 the Ludwigson curve models the curve very accurately at all strains while the Hollomon curve is less accurate at low strains. In Figure 50 the Hollomon equation then models the stress-strain curve accurate for low strains but instead becomes less accurate at high strains which will overestimate the UTS for a given plastic strain in the material.

The Matlab script was used to generate stress-strain diagrams for all the samples extracted from the third cylinder head. In order to compare the results, the Matlab script with the same settings was also used to generate the stress-strain diagrams for all the samples in the first and second cylinder head as well.

4.1.1 Comparing the UTS-values between the three cylinder heads

In order to validate the results collected from the two previously investigated cylinder heads a table was assembled exhibiting the UTS-values as seen in Table 3. Since grey iron is the material investigated, only the UTS values are comparable.

Table 3. Exhibiting the ultimate tensile strength, UTS, provided from all the 30 selected locations in all the three cylinder heads, 90 in total. Also displaying the calculated mean and standard deviation values. Red color indicates missing data.

	CH1	CH2	CH3	Analysis		
Sample	**UTS [MPa]**	**UTS [MPa]**	**UTS [MPa]**	**Mean [μ]**	**STDEV [σ]**	**CV [σ/μ]**
2A1	273	277	261	**270**	**6.8**	**3%**
2A2	302	279	276	**286**	**11.6**	**4%**
2A3	248	244	257	**250**	**5.4**	**2%**
2A4	279	261	295	**278**	**13.9**	**5%**
2B1	290	278	267	**278**	**9.4**	**3%**
2B2	267	279	308	**285**	**17.2**	**6%**
3A1	286	268	265	**273**	**9.3**	**3%**
3A2	288	271	297	**285**	**10.8**	**4%**
3A3	256	250	242	**249**	**5.7**	**2%**
3A4	292	282	-	**287**	**5.0**	**2%**
3B1	286	286	279	**284**	**3.3**	**1%**
3B2	303	299	295	**299**	**3.3**	**1%**
4A1	271	269	270	**270**	**0.8**	**0%**
4A2	266	277	297	**280**	**12.8**	**5%**
4A3	281	258	269	**269**	**9.4**	**3%**
4A4	260	263	281	**268**	**9.3**	**3%**
4B1	277	270	281	**276**	**4.5**	**2%**
4B2	288	290	283	**287**	**2.9**	**1%**
5A1	302	-	262	**282**	**20.0**	**7%**
5A2	293	278	313	**295**	**14.3**	**5%**
5A3	267	255	268	**263**	**5.9**	**2%**
5A4	296	262	279	**279**	**13.9**	**5%**
5B1	273	282	285	**280**	**5.1**	**2%**
5B2	274	282	285	**280**	**4.6**	**2%**
6A1	264	-	262	**263**	**1.0**	**0%**
6A2	363	286	304	**318**	**32.9**	**10%**
6A3	279	266	261	**269**	**7.6**	**3%**
6A4	283	272	289	**281**	**7.0**	**3%**
6B1	296	288	292	**292**	**3.3**	**1%**
6B2	308	296	306	**303**	**5.2**	**2%**

In Table 3 all UTS-values collected from cylinder head 1, 2 and 3 are displayed. All results are based on three measurements except for the sample locations 3A4, 5A1 and 6A1 where only two results are analyzed due to failed tensile testing measurements, marked in red. The values are organized with the cylinder number and the location where the samples were extracted going from top to bottom. The mean value (μ) and the standard deviation (σ) are calculated in order to validate the mechanical properties of the samples extracted from the same locations. The standard deviation shows that the variation of all 30 UTS-values arranges between 0-10 % of the calculated mean values, which results in deviations between 0.8-32.9 MPa. This is true when analyzing all the samples but the majority of the samples shows a variation below 5 % of the calculated mean values, which only results in a maximum deviation of 14.3 MPa.

In Figure 51, Figure 52 and Figure 53 the variation in UTS is displayed in the three investigated cylinder heads, also specifying the cylinder and the location from where the samples have been extracted.

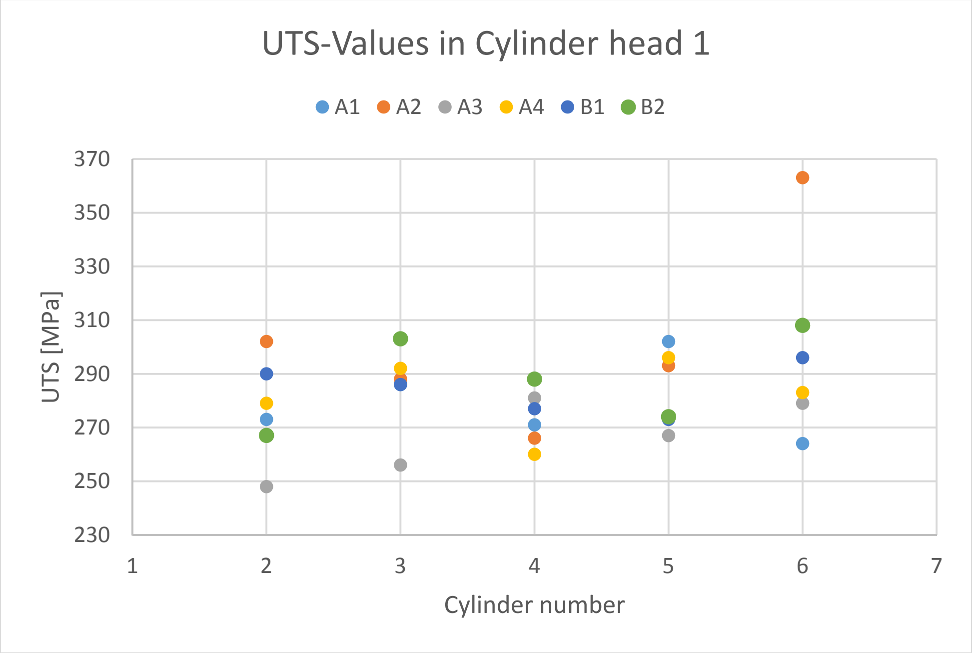

Figure 51. Overview of the UTS-values from Cylinder head 1. The chart is showing the sample locations, both the cylinder number and the position in the cylinder.

From the data collected from the first cylinder head seen in Figure 51 variations in UTS-values can be observed depending on which cylinder or location within the cylinder the samples have been extracted from. From sample 2A3 with the lowest value of 248 MPa up to sample 6A2 with the highest value of 363 MPa. When observing the diagram one can see that the result of the tensile test made on the sample 6A2 is divergent and should be considered as a faulty value. The majority of the data collected varies between 250-310 MPa. The variation is larger comparing the six different locations in one cylinder than compared to the samples from the same location in all cylinders.

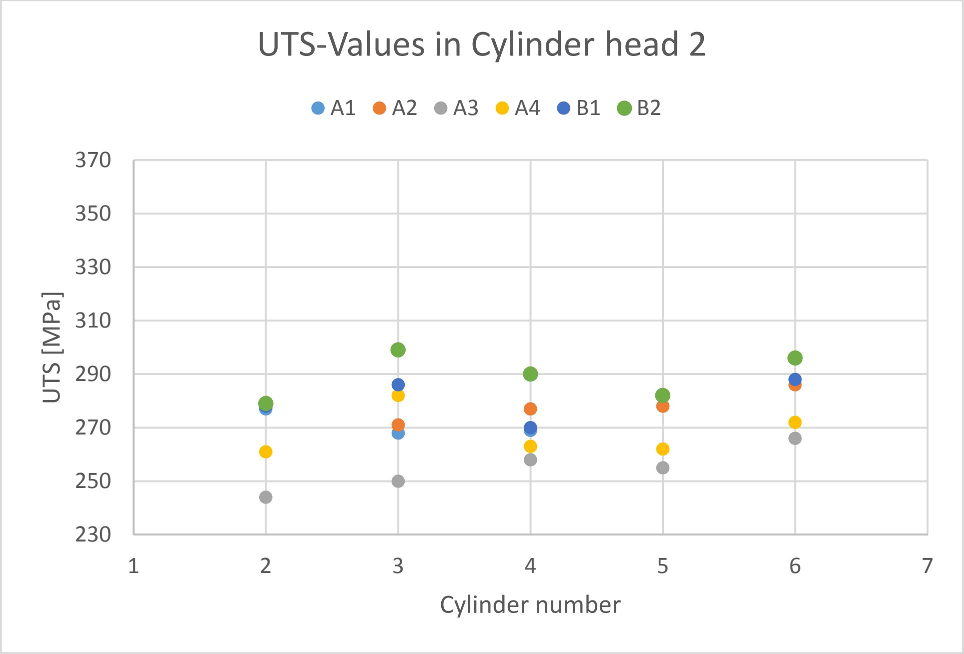

Figure 52. Overview of the UTS-values from Cylinder head 2. The chart is showing the sample locations, both the cylinder number and the position in the cylinder.

Observations regarding the data gathered from the second cylinder head which is shown in Figure 52 detects variations as well. From sample 2A3 with the lowest value of 244 MPa up to sample 3B2 with the highest value of 299 MPa. The variation is correspondingly larger when comparing the locations in one cylinder than comparing the samples with the same location in all cylinders, also acknowledged from the data collected from the first cylinder head. The UTS-values of sample 5A1 and 6A1 are missing due to failure when performing the tensile testing measurements.

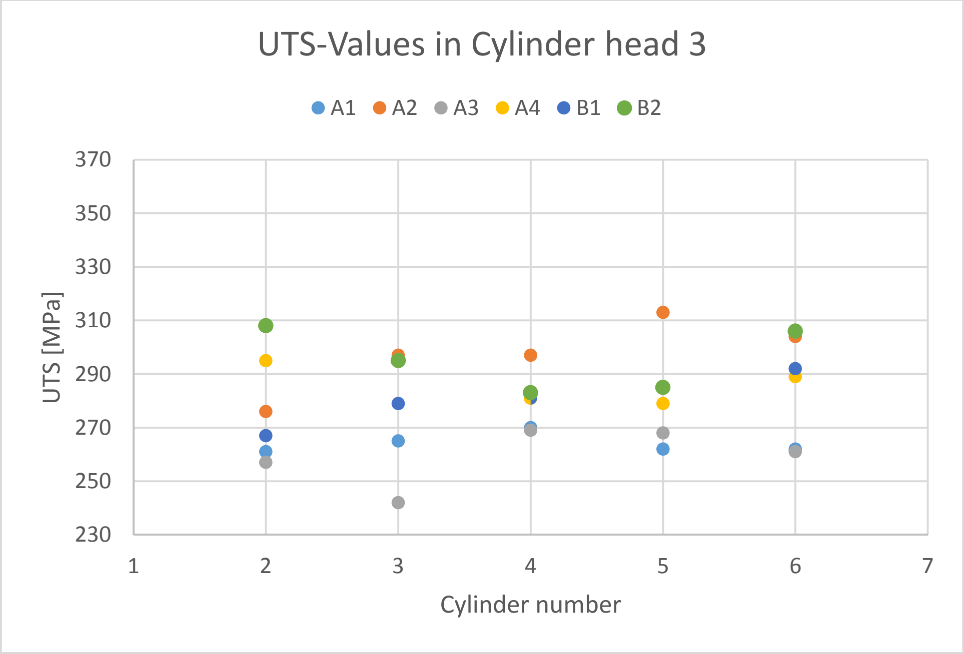

Figure 53. Overview of the UTS-values from Cylinder head 3. The chart is showing the sample locations, both the cylinder number and the position in the cylinder.

Figure 53 exhibits the variations of the UTS-values from the measurements made of the third cylinder head. The sample 3A3 measured the lowest value, 242 MPa, whilst the sample 5A2 measured the highest value of 313 MPa. The variation is also larger in the third cylinder head when comparing the sample positions in one cylinder than if comparing the samples from the same position in all cylinders. The UTS-value of the sample 3A4 is missing due to failure when performing the tensile testing measurements.

When analyzing the findings from all cylinder heads the majority of all UTS-values can be observed in the range 250-310 MPa. Three out of the 90 samples undergoing the tensile testing resulted in failed data. If excluding the sample with a faulty measurement, 6A2, the highest mean value is observed in sample location 6B2 with a UTS-value of 303 MPa while the sample location 3A3 has the lowest mean UTS-value of 249 MPa. The difference between the two are 54 MPa, a difference of about 22 %.

4.1.2 Microstructure analysis comparing six selected samples

In order to validate the provided data of the mechanical properties from the two previously completed projects Table 4 and Figure 54 were created to analyze the six selected samples of each cylinder head, 18 samples in total. Microstructure analysis was conducted on all 18 samples according to section 3.5.

Table 4. Exhibiting the Ultimate tensile strength provided from the six selected locations in each cylinder head together with the calculated mean and standard deviation values.

	CH1	CH2	CH3	Analysis		
Sample	**UTS (MPa)**	**UTS (MPa)**	**UTS (MPa)**	**Mean (µ)**	**STDEV (σ)**	**σ/µ (CV)**
2A3	248	244	257	**250**	**5,4**	**2%**
2A4	279	261	295	**278**	**13,9**	**5%**
3A3	256	250	242	**249**	**5,7**	**2%**
3A4	292	282	-	**287**	**5,0**	**2%**
3B2	303	299	295	**299**	**3,3**	**1%**
6B2	308	296	306	**303**	**5,2**	**2%**

In Table 4 the mean value (µ) and the standard deviation (σ) are calculated in order to validate the mechanical properties for the samples from the same extraction point. The standard deviation shows that the variation of the UTS-values is between 1-5% of the mean values. The results only show a variation between 4-13.9 MPa when analyzing the six selected samples. The results are based on three measurements except for the 3A4 locations were test results from the third cylinder head is missing due to failed tensile testing measurements.

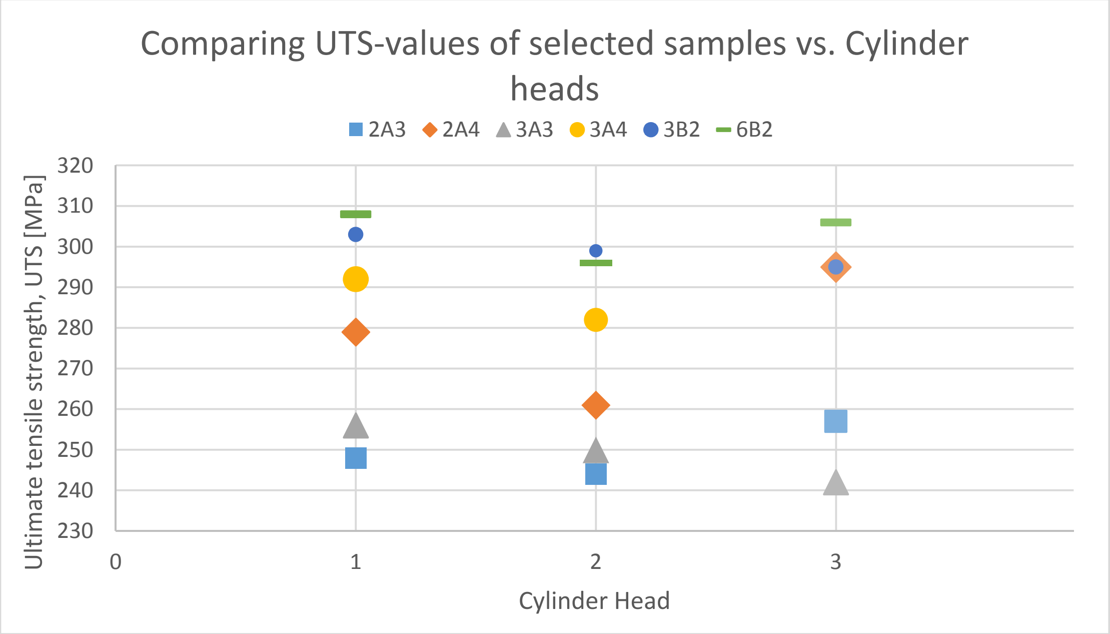

Figure 54. Comparing UTS-values of the six selected samples in cylinder head 1. 2 and 3.

Figure 54 displays the selected samples with the locations within the cylinder heads and compares the UTS-values. The samples with the same location have the same marker, e.g. 2A3 - blue square, 2A4 - orange diamond, 3A3 - grey triangle, 3A4 - yellow circle, 3B2 - dark blue circle and 6B2 - green stripe.

Visual comparison of microscope images

In order to connect the microstructure to the mechanical properties images were captured as mentioned in 3.5.1. The following images seen in Figure 55 - Figure 60 were used to visually analyze the microstructures in the six different locations.

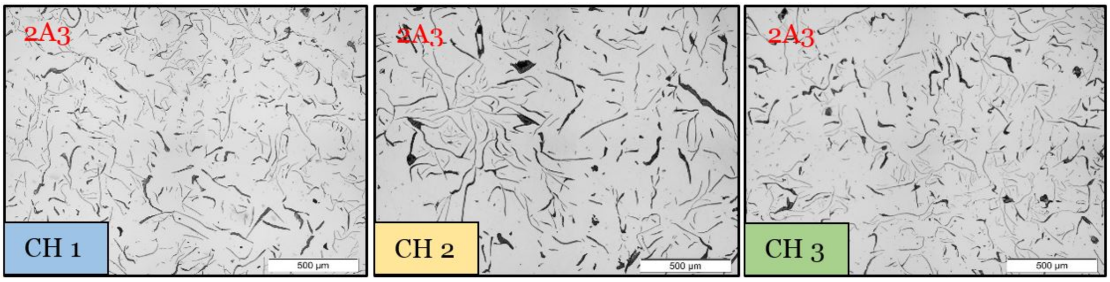

Figure 55. Images captured of samples from the same location, 2A3. Left image from the first cylinder head (248 MPa), the middle image from the second cylinder head (244 MPa) and the right one from the third cylinder head (257 MPa).

In Figure 55 a difference in microstructure can be seen when comparing the 2A3 samples from the first, second and third cylinder head. The microstructure image from the second cylinder head displayed a coarser structure than both the samples from the first and the third cylinder head. With this information together with the mechanical properties the finer structure can be seen to correspond to a higher UTS-value. The difference is not large when analyzing the first and second sample, only 4 MPa.

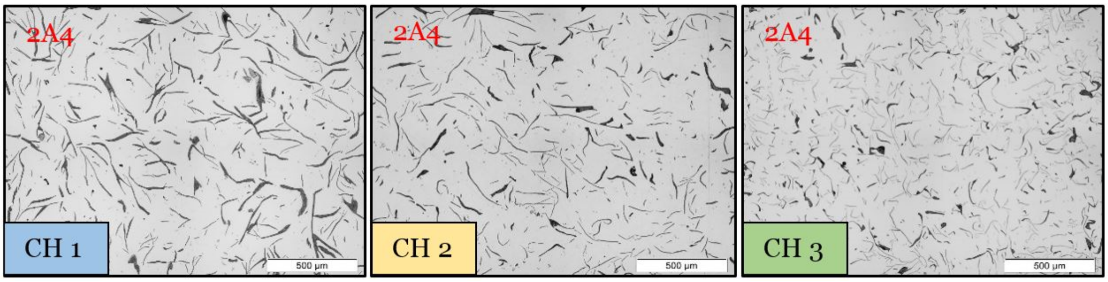

Figure 56. Images captured of samples from the same location, 2A4. Left image from the first cylinder head (279 MPa), the middle image from the second cylinder head (261 MPa) and the right one from the third cylinder head (295 MPa).

In Figure 56 the microstructures of 2A4 samples also differs, showing a finer structure in the sample from the third cylinder head and similar structures from the first and second. The first sample seems to have thicker graphite flakes than the second. When analyzing the mechanical properties, the sample with a finer structure have the highest value of 295 MPa. The two samples with similar structures but with different thickness of the graphite flakes also differs. It shows that the sample from the first cylinder head with thicker graphite flakes gives a higher value, 279 MPa, than the sample from the second cylinder head, 261 MPa.

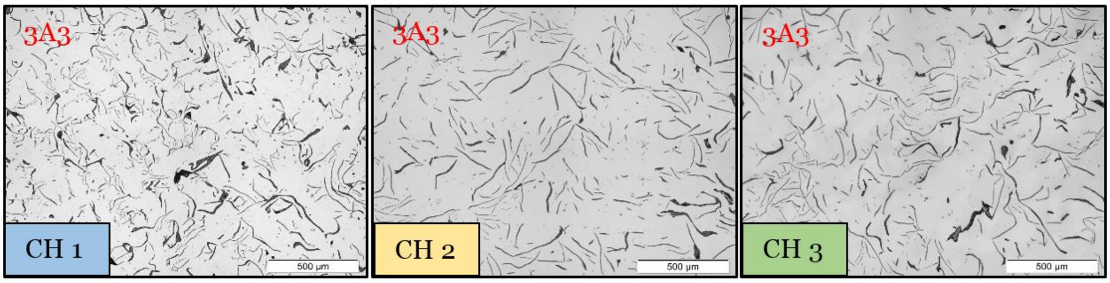

Figure 57. Images captured of samples from the same location, 3A3. Left image from the first cylinder head (256 MPa), the middle image from the second cylinder head (250 MPa) and the right one from the third cylinder head (242 MPa).

In Figure 57 observations can distinguish a finer microstructure in the 3A3 sample from the first cylinder head, this is also the one that yielded the highest UTS-value of the three samples, 256 MPa. The samples from the second and the third cylinder head have coarser microstructures but almost similar UTS-values, 250 MPa from the second and 242 MPa from the third. The difference from the highest to the lowest value does not seem to correlate to only the microstructure seen in the pictures.

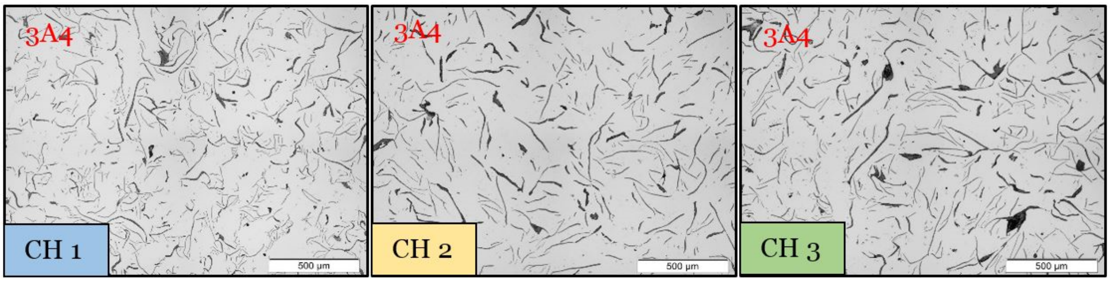

Figure 58. Images captured of samples from the same location, 3A4. Left image from the first cylinder head (292 MPa), the middle image from the second cylinder head (282 MPa) and the right one from the third cylinder head (Failed tensile test).

In Figure 58 the sample with the finest microstructure, the 3A4 sample from the first cylinder head, exhibit the highest UTS-value of 292 MPa. The samples from the second and third cylinder head displays a coarser structure but only the second have a UTS-value to be analyzed, 282 MPa. Due to the failed tensile test of the sample from the third cylinder head no further analyze can be done connecting the microstructure to the mechanical properties.

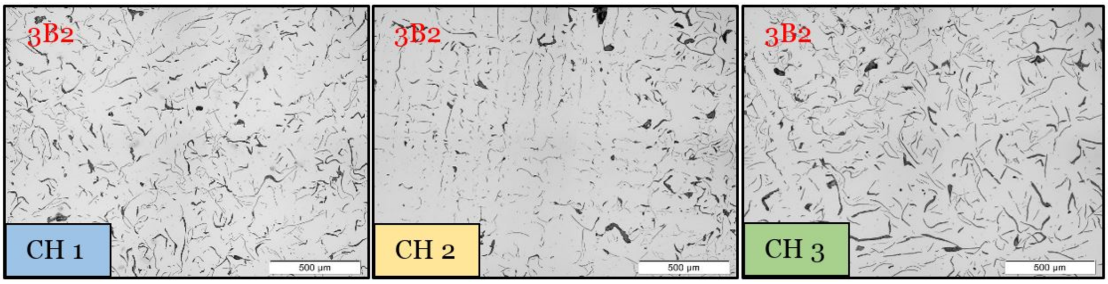

Figure 59. Images captured of samples from the same location, 3B2. Left image from the first cylinder head (303 MPa), the middle image from the second cylinder head (299 MPa) and the right one from the third cylinder head (295 MPa).

In Figure 59 all three 3B2 samples exhibits fine microstructures where the graphite flakes seem to be organized in straight lines. All three samples from the cylinder heads displays high UTS-values, 303 MPa from the first cylinder, 299 MPa from the second and 295 MPa from the third.

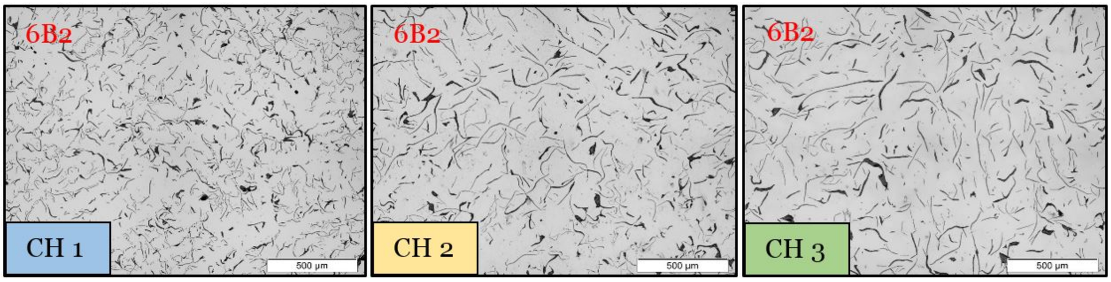

Figure 60. Images captured of samples from the same location, 6B2. Left image from the first cylinder head (308 MPa), the middle image from the second cylinder head (296 MPa) and the right one from the third cylinder head (306 MPa).

In Figure 60 the microstructure of the 6B2 sample from the first cylinder exhibits a finer structure than the second and the third cylinder head. The sample from the first cylinder head also showed the highest UTS-value with 308 MPa. All samples showed a high UTS-value and the difference was only 2 MPa between the highest value and the value collected from the third cylinder head.

The findings collected when trying to connect the microstructure to the mechanical properties indicates that a fine microstructure here corresponds to a high UTS-value. Findings have also shown indications that this may not be the only parameter deciding the mechanical properties of the material investigated.

Microstructural parameters from image analysis

The mechanical property studied, ultimate tensile strength (UTS), was connected to the microstructure parameters of the graphite measured in the image analysis. All three images from each samples were used in the image analysis of the graphite microstructure. The graphite fraction of the 18 samples was measured and the result can be seen in Figure 61 which also shows the measured ultimate tensile strength of the samples.

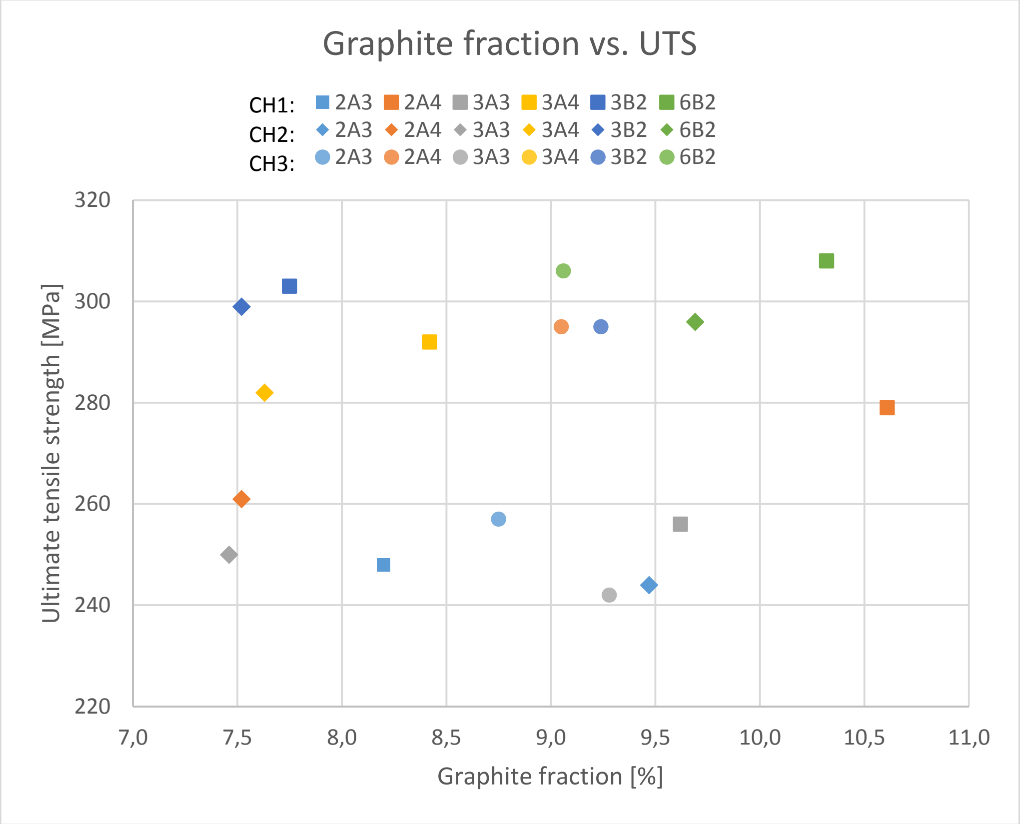

Figure 61. Graph showing the ultimate tensile strength for each of the six studied samples in all three cylinder heads at their different graphite fractions.

As seen in Figure 61 there is no correlation between graphite fraction and UTS of the material. Also it can be seen that the graphite fraction varies from around 7.5 % to 10.5 % in all of the 18 samples. The graphite fraction also varies between the three cylinder heads for the same sample locations.

The relation between the mean graphite particle area and the UTS can be seen in Figure 62.

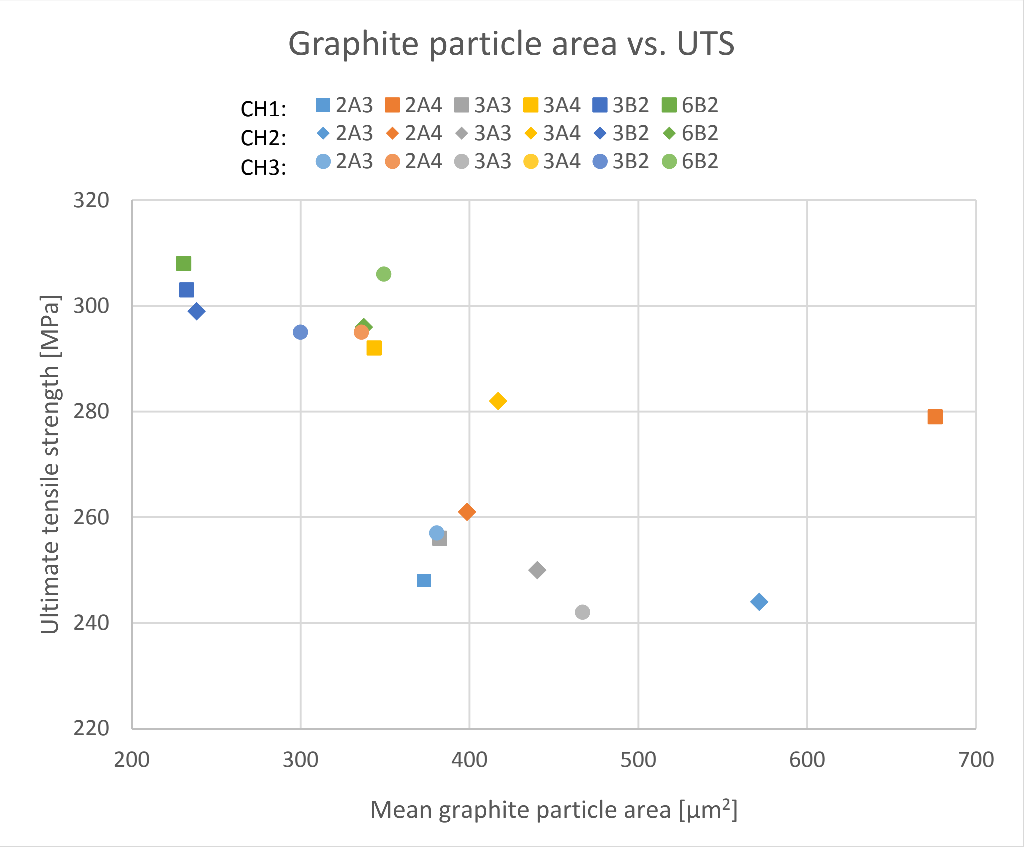

Figure 62. Graph showing the ultimate tensile strength for each of the six studied samples in all three cylinder heads at their different mean graphite particle area.

As seen in Figure 62 there is some correlation between the mean graphite particle area and the UTS. The UTS is lower in samples with larger graphite particles. It can also be seen that the graphite particle area varies between the three cylinder heads for the same sample locations.

In Figure 63 the relation between the number of graphite particles per mm² and the UTS is shown.

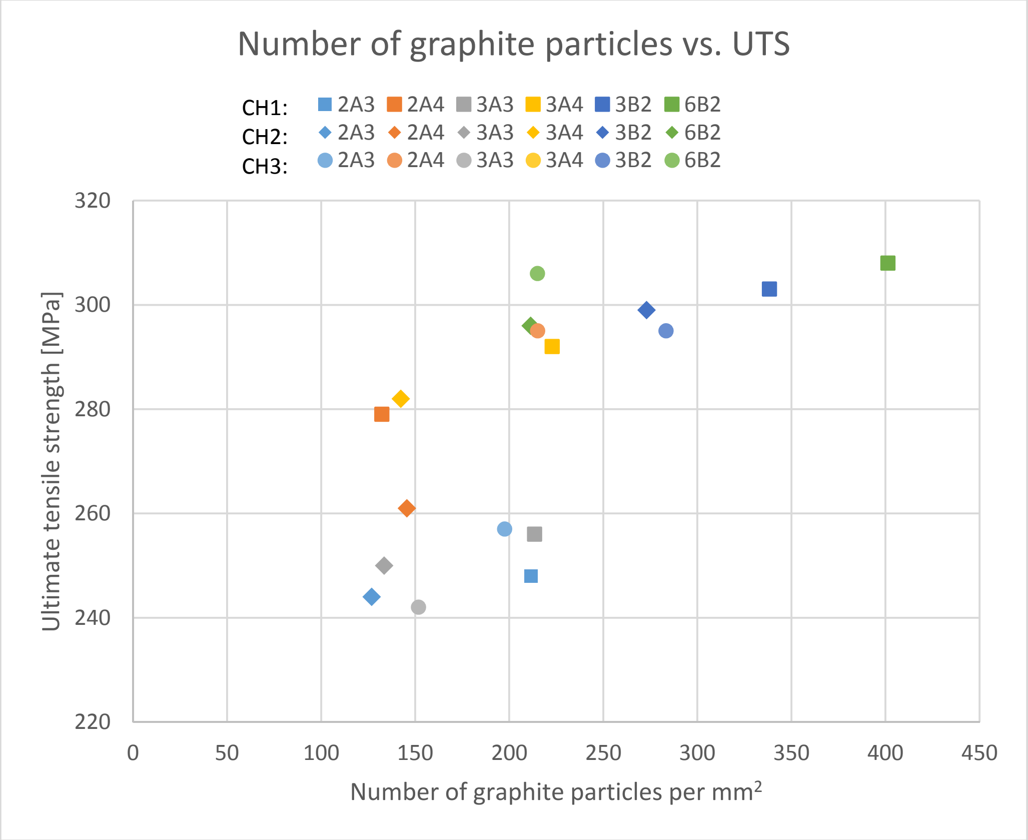

Figure 63. Graph showing the ultimate tensile strength for each of the six studied samples in all three cylinder heads at their different number of particles per mm².

As seen in Figure 63 there is some correlation between the number of graphite particles per mm² and UTS in the material. The UTS is higher in samples with more graphite particles.

The maximum Feret length (Feret max), was also measured in the image analysis. In Figure 64 the relation between the mean Feret max of all the graphite particles in each sample and the UTS can be seen. Figure 65 shows the Feret max of only the 99th percentile of the graphite particles in each image analyzed and the relation to the UTS.

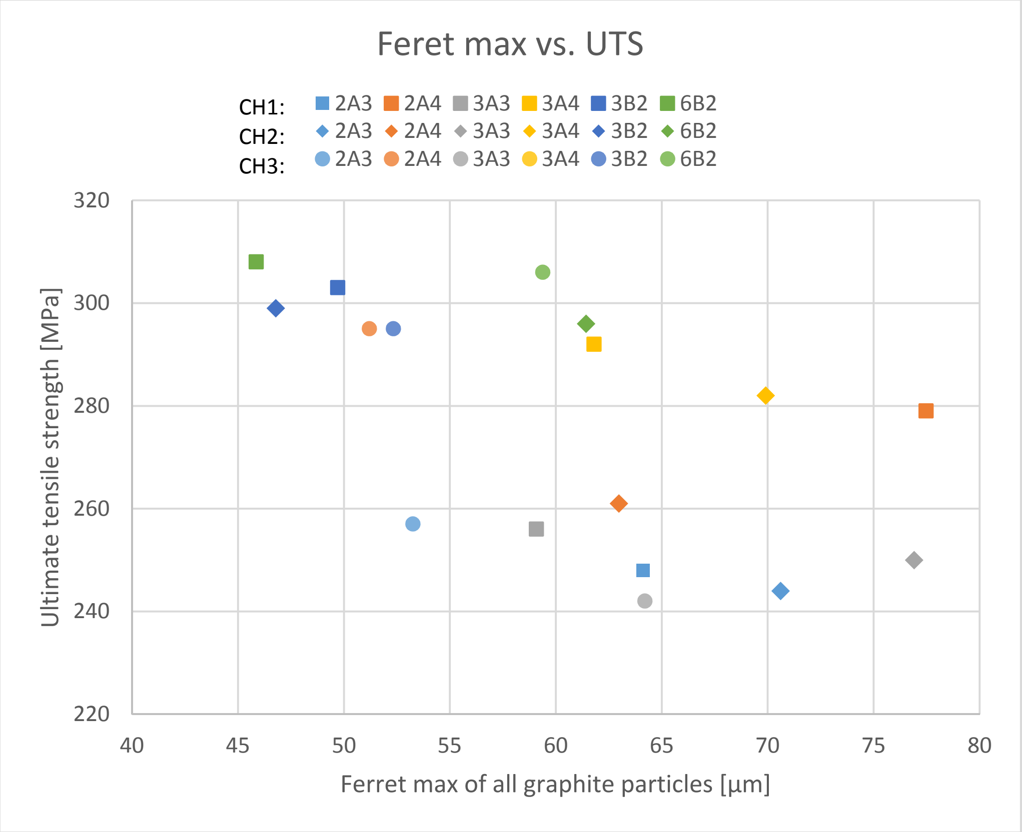

Figure 64. Graph showing the ultimate tensile strength for each of the six studied samples in all three cylinder heads at their different maximum Feret of all particles analyzed.

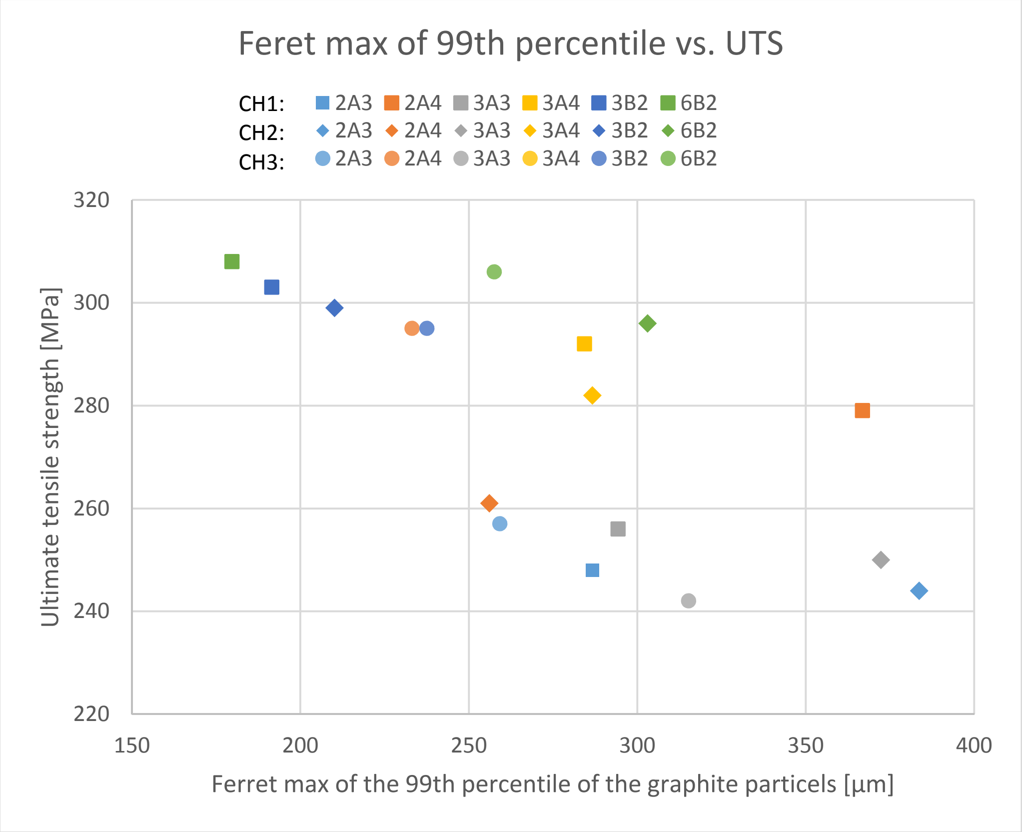

Figure 65. Graph showing the ultimate tensile strength for each of the six studied samples in all three cylinder heads at their different maximum Feret of the 99th percentile of the particles in each image analyzed.

As seen in Figure 64 there is some correlation, however not very clear, between the Feret max of all the graphite particles and the UTS. In Figure 65 the correlation between the Feret max of the 99th percentile and the UTS is clearer. Both graphs indicate that the UTS is lower in samples with longer graphite particles and particularly in samples where the longest graphite particles, the 99th percentile, are longer.

4.2 Physical test results

The results from the physical property testing as well as microstructure analyses are here presented followed by analyses of the results. The section ends with a comparison of the models, using the parameters of the graphite determined in the microstructure analysis, to the experimental values for thermal conductivity.

4.2.1 Dilatometer – thermal expansion

As mentioned in section 3.3.2 and discussed further in section 5.1.2, only six of the nine physical samples were measured with the dilatometer. The data from the dilatometer tests was handled and the coefficient of thermal expansion (CTE), α, was calculated using equation (27) for each selected temperature from 50°C to 500°C using ΔT of around 5°C. The CTE could not be determined well at room temperature, instead CTE at 50°C is presented. The CTE for the six different physical samples can be seen in Table 5 in Figure 66.

Table 5. Coefficient of thermal expansion different temperatures for the six of the physical test samples.

CTE, α [μm/(m·°C)] (ΔT=5)						
Temp °C	**50**	**100**	**200**	**300**	**400**	**500**
3B1F	8.513	11.887	14.173	15.076	15.060	16.546
4B1F	9.924	12.318	14.279	15.034	15.437	16.552
5B1F	10.394	12.392	14.466	15.366	15.644	16.791
3B2F	10.525	12.145	14.007	15.094	14.776	15.982
4B2F	9.409	11.769	13.760	15.094	14.649	15.569
5B2F	10.469	12.489	14.066	14.954	14.080	14.913
Mean (μ)	**10.144**	**12.223**	**14.116**	**15.109**	**14.917**	**15.961**
STDEV (σ)	0.790	0.288	0.242	0.139	0.567	0.718
σ/μ (CV)	7.79%	2.36%	1.72%	0.92%	3.80%	4.50%

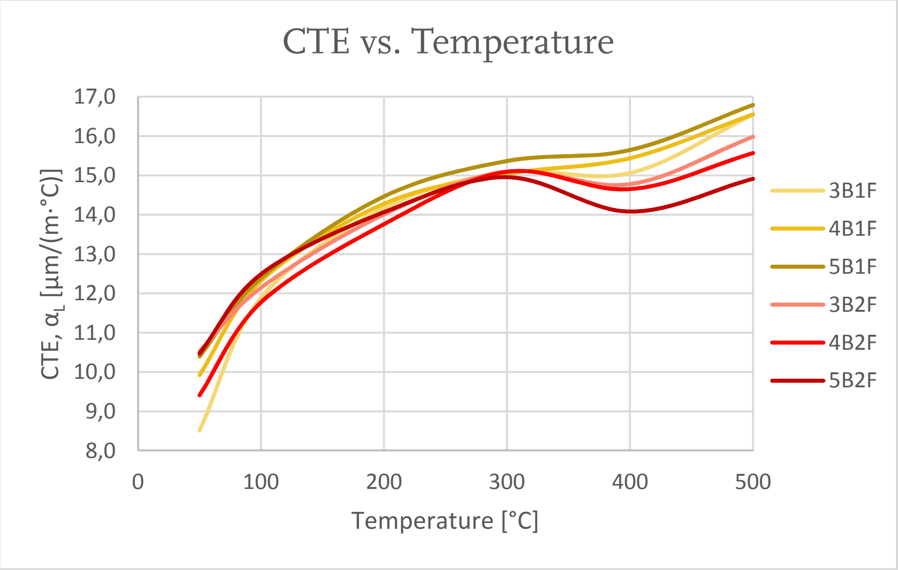

Figure 66. Coefficient of thermal expansion, α, at temperatures from 50-500°C for the six physical test samples. Samples with intermediate solidification time are in yellow and samples with long solidification time are in red.

As seen in Table 5 and Figure 66 the variation is higher at low (50-100°C) and high temperatures (400-500°C) while the variation is much lower at intermediate temperatures. All the samples from the location with short solidification time has larger CTE than the samples from the location with long solidification time at 400°C and above. However, there is no difference between the two sample locations at lower temperatures.

4.2.2 Density

The nine samples' weight in air and their measured density in room temperature were as follows:

- 3B1F – 3.8858 g – 7247.0 kg/m3
- 3B2F – 3.8381 g – 7268.5 kg/m3
- 4B1F – 3.8210 g – 7254.0 kg/m3
- 4B2F – 3.8087 g – 7212.5 kg/m3
- 5B1F – 3.8241 g – 7272.0 kg/m3
- 5B2F – 3.8120 g – 7275.7 kg/m3
- 01F – 3.7531 g – 7246.7 kg/m3
- 02F – 3.9000 g – 7259.0 kg/m3
- 03F – 3.7687 g – 7248.0 kg/m3

The density at elevated temperatures for the samples taken at slow and fast solidification were calculated using equation (28) with the α-values as shown in Table 5. The densities for the samples taken at fast solidification at elevated temperatures could not be calculated in the same way since no thermal expansion testing was performed for those samples. Instead the change in density at elevated temperatures were calculated by multiplying the density values at 25 °C with a change factor. The change factors were calculated for each temperature increase for each of the six samples with known densities and the mean value was used in the calculations. The change factors can be seen in Table 6. All the densities are shown in Table 7 and in Figure 67.

Table 6. Change factors used to calculate densities at elevated temperature for the three samples with unknown CTE.

Change factor for density					
Temp change °C	**25-100**	**100-200**	**200-300**	**300-400**	**400-500**
3B1F	0.9973	0.9953	0.9951	0.9956	0.9935
4B1F	0.9972	0.9953	0.9952	0.9951	0.9939
5B1F	0.9972	0.9952	0.9950	0.9952	0.9938
3B2F	0.9973	0.9954	0.9950	0.9959	0.9940
4B2F	0.9974	0.9955	0.9948	0.9960	0.9944
5B2F	0.9972	0.9955	0.9951	0.9966	0.9947
Mean (μ)	0.9973	0.9954	0.9950	0.9957	0.9941
STDEV (σ)	0.0001	0.0001	0.0001	0.0006	0.0004
σ/μ (CV)	0.01%	0.01%	0.01%	0.06%	0.04%

Table 7. Densities at temperatures from 25-500°C. Measured values for 25°C and calculated values from 100-500°C using equation (28).

Density, ρ [kg/m^3]						
Temp °C	**25**	**100**	**200**	**300**	**400**	**500**
3B1F	7247.0	7227.7	7193.5	7158.0	7126.3	7080.1
4B1F	7254.0	7234.0	7200.0	7165.1	7130.2	7086.8
5B1F	7272.0	7251.8	7217.2	7181.0	7146.2	7102.1
3B2F	7268.5	7248.7	7215.4	7179.1	7149.6	7106.7
4B2F	7212.5	7193.5	7160.8	7123.8	7095.6	7056.0
5B2F	7275.7	7255.3	7222.4	7187.0	7162.3	7124.3
01F	7246.7	7226.9	7193.4	7157.5	7126.9	7084.6
02F	7259.0	7239.2	7205.6	7169.7	7139.0	7096.6
03F	7248.0	7228.2	7194.6	7158.8	7128.2	7085.9
Mean (μ)	7253.7	7233.9	7200.3	7164.4	7133.8	7091.4
STDEV (σ)	19.0	18.6	18.4	18.7	18.9	19.2
σ/μ (CV)	0.26%	0.26%	0.26%	0.26%	0.26%	0.27%

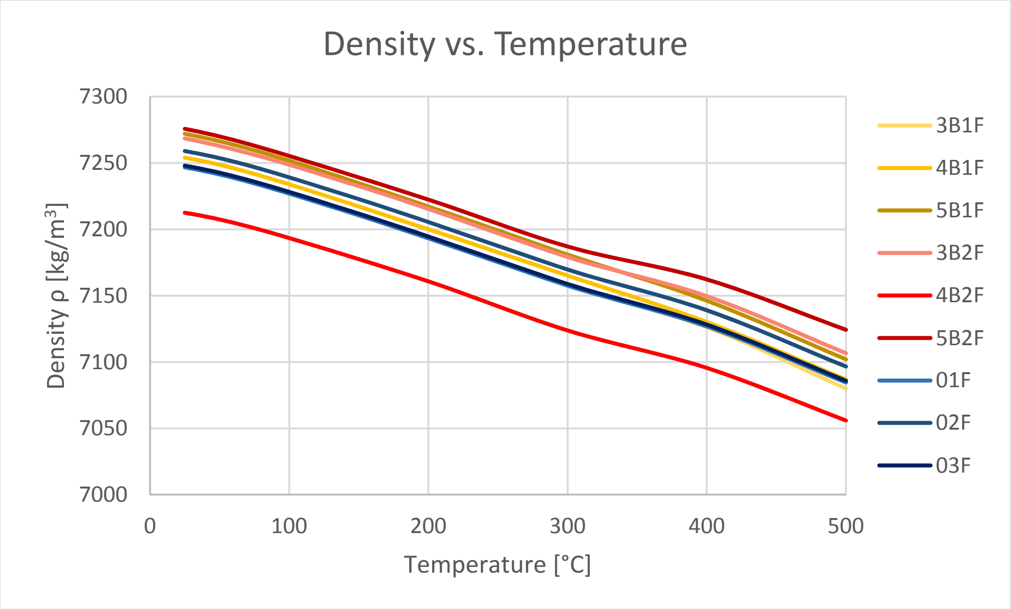

Figure 67. Density at temperatures from 25-500°C. Samples with short solidification time are in blue and samples with long solidification time are in red.

As seen in Table 7 and Figure 67 the density does not vary significantly between the samples. Also there is no difference between the three solidification conditions.

4.2.3 DSC – Specific heat

The C_p curve for specific heat at any given temperature was generated using a standard method, ratio method, built-in in the computer software for the DSC machine. The curve for the first sample. DSC1 can be seen in Figure 68.

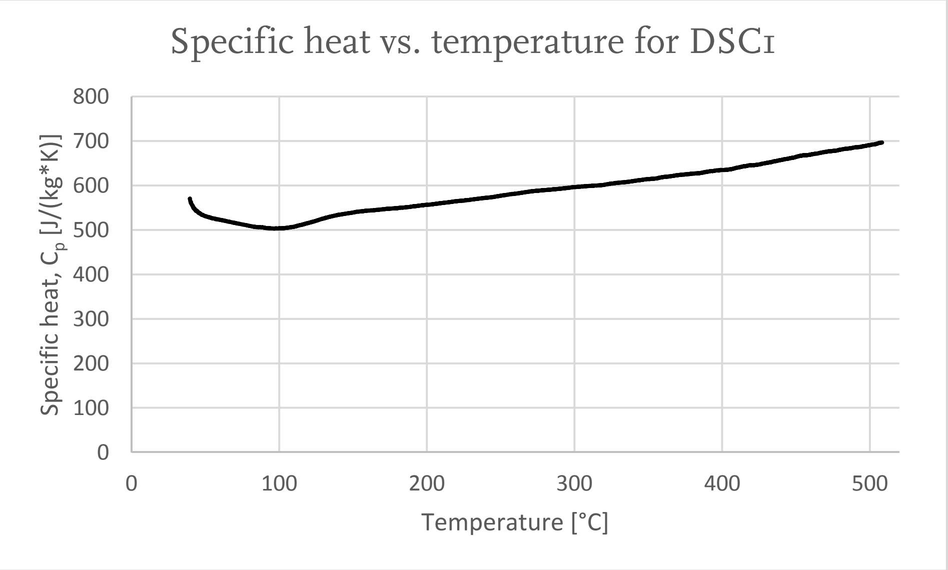

Figure 68. Graph of the specific heat values from the DSC1 sample showing incorrect values below 100°C.

The curve gives incorrect values for the specific heat for temperatures below 100°C. A customary way of dealing with the incorrect values is to interpolate a line to the almost linear part of the curve and extrapolate the missing values from the line. The C_p-values from 100-500°C for the three samples were extracted from the experimental values and mean values were calculated for each temperature as seen in Table 8 and their values can be seen in the black curve in Figure 69. For the room temperature, 25°C, the experimental mean values were linearly interpolated using Microsoft Excel's function for trend line, the dotted line in Figure 69, and the value was calculated using the linear equation (32). The calculated value can be seen in green in Figure 69.

Table 8. Specific heat values at different temperatures from DSC measurements. Experimental values from 100-500°C and calculated value in for 25°C from equation (32) from the trend line in Figure 69.

Specific heat, C_p [J/(kg·K)]						
	Calculated	**Experimental values**				
Temp °C	**25**	**100**	**200**	**300**	**400**	**500**
DSC1		503.45	556.65	596.46	634.81	690.82
DSC2		511.83	556.81	599.03	642.64	707.09
DSC3		512.19	557.91	597.65	637.79	697.22
Mean (μ)	**474**	**509**	**557**	**598**	**638**	**698**
STDEV (σ)		4.04	0.56	1.05	3.23	6.69
CV (σ/μ)		0.79%	0.10%	0.18%	0.51%	0.96%

$$C_p = 0.4597 \cdot T + 462.24 \tag{32}$$

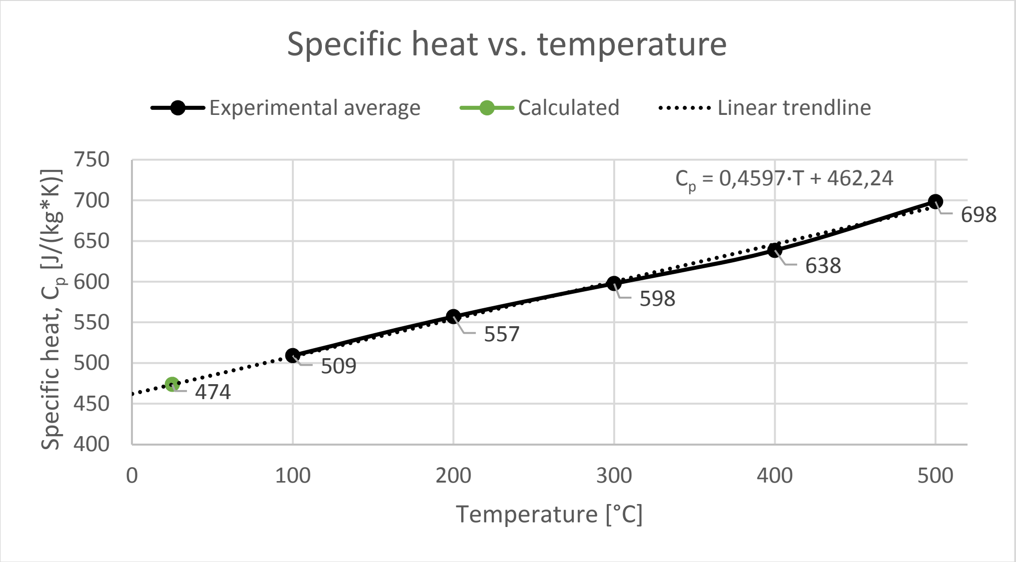

Figure 69. Graph of the specific heat values at different temperatures from DSC measurements. Experimental average values in black and calculated value in green for 25°C from the trend line, equation (32).

As seen in Table 8 the specific heat values do not vary significantly. Also, as seen in Figure 69 the average specific heat results of the DSC measurements fall almost perfectly on a line.

4.2.4 LFA – Thermal diffusivity

The thermal diffusivity results were given directly as the average value of the five shots at each temperature from the LFA and the values can be seen in Table 9.

Table 9. Thermal diffusivity values from the LFA-measurements.

Thermal diffusivity, α [mm^2/s]						
Temp °C	**25**	**100**	**200**	**300**	**400**	**500**
3B1F	14.45	12.82	11.41	10.23	9.09	8.05
4B1F	14.30	12.77	11.41	10.20	9.13	8.04
5B1F	14.26	12.56	11.15	9.95	8.83	7.83
Mean (μ) 1F	**14.34**	**12.72**	**11.32**	**10.12**	**9.02**	**7.97**
STDEV (σ) 1F	0.08	0.11	0.12	0.13	0.13	0.10
CV (μ/σ) 1F	0.58%	0.89%	1.07%	1.26%	1.47%	1.28%
3B2F	14.13	12.62	11.24	10.02	8.93	7.93
4B2F	14.55	12.71	11.28	10.06	8.92	7.81
5B2F	14.38	12.59	11.12	9.87	8.79	7.70
Mean (μ) 2F	**14.35**	**12.64**	**11.21**	**9.98**	**8.88**	**7.81**
STDEV (σ) 2F	0.17	0.05	0.07	0.08	0.06	0.10
CV (μ/σ) 2F	1.21%	0.39%	0.60%	0.82%	0.73%	1.23%
01F	13.84	12.46	11.07	9.91	8.80	7.75
02F	13.82	12.35	10.98	9.79	8.75	7.65
03F	13.96	12.38	11.06	9.86	8.79	7.72
Mean (μ) 0F	**13.87**	**12.39**	**11.04**	**9.85**	**8.78**	**7.71**
STDEV (σ) 0F	0.06	0.05	0.04	0.05	0.02	0.04
CV (μ/σ) 0F	0.46%	0.37%	0.35%	0.53%	0.27%	0.51%

As seen in Table 9 the variation between the three samples in each solidification condition and for each temperature is low.

4.2.5 Thermal conductivity

After having the result for density, specific heat and thermal diffusivity the thermal conductivity could be calculated using equation (16) and the result is shown in Table 10 and Figure 70.

Table 10. Thermal conductivity calculated using equation (16).

Thermal conductivity, λ [W/(m·K)]						
Temp °C	**25**	**100**	**200**	**300**	**400**	**500**
3B1F	49.61	47.16	45.74	43.76	41.34	39.81
4B1F	49.15	47.05	45.76	43.67	41.57	39.79
5B1F	49.12	46.37	44.84	42.69	40.28	38.83
Mean (μ) 1F	**49.29**	**46.86**	**45.45**	**43.37**	**41.06**	**39.48**
STDEV (σ) 1F	0.23	0.35	0.43	0.49	0.56	0.46
CV (μ/σ) 1F	0.46%	0.75%	0.94%	1.13%	1.36%	1.16%
3B2F	48.65	46.56	45.18	42.98	40.74	39.37
4B2F	49.73	46.54	45.00	42.84	40.41	38.46
5B2F	49.55	46.51	44.75	42.40	40.17	38.30
Mean (μ) 2F	**49.31**	**46.54**	**44.98**	**42.74**	**40.44**	**38.71**
STDEV (σ) 2F	0.47	0.02	0.18	0.25	0.23	0.47
CV (μ/σ) 2F	0.95%	0.04%	0.39%	0.57%	0.57%	1.22%
01F	47.51	45.83	44.36	42.41	40.05	38.34
02F	47.51	45.51	44.08	41.94	39.87	37.93
03F	47.94	45.55	44.32	42.17	40.02	38.18
Mean (μ) 0F	**47.65**	**45.63**	**44.25**	**42.17**	**39.98**	**38.15**
STDEV (σ) 0F	0.20	0.14	0.12	0.19	0.08	0.17
CV (μ/σ) 0F	0.42%	0.31%	0.28%	0.46%	0.20%	0.44%

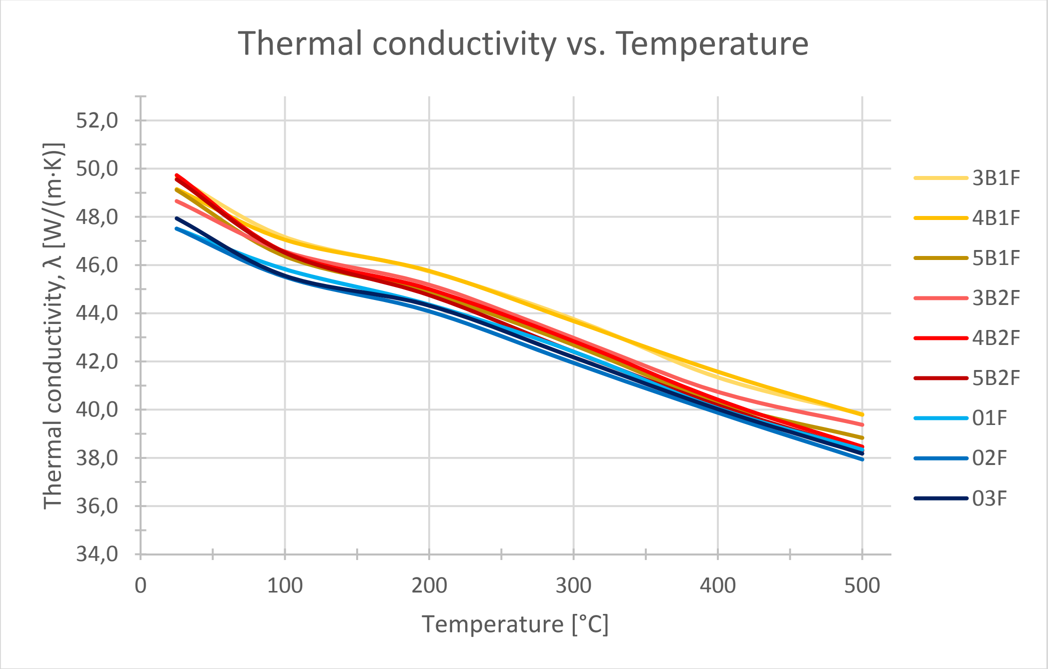

Figure 70. Graph of the thermal conductivity for each sample for temperatures from 25-500°C

As seen in Table 10 and Figure 70, the thermal conductivity decrease with temperature which is expected from the literature, see Figure 14. It is also clear that there is no difference in thermal conductivity between the samples taken from intermediate solidification and the samples taken from the slow solidification. However, there is a difference, although small, between the samples taken from slow (and intermediate) solidification and the samples taken from the fast solidification. This difference is the largest at 25°C, about 3.4 % less, and decreases with increased temperature, about 1.1 % at 400°C and 1.4 % at 500°C.

4.2.6 Microstructure analysis

The results from the image analysis software of the images from the nine physical samples are presented in this section followed by analyses of the results. The graphite microstructures of the three solidification conditions are compared both visually and by the values for graphite fraction and the size of the graphite particles. The matrix is also confirmed to be pearlitic.

Visual comparison of microscope images

When studying the images from the optical microscope it is quite clear that the graphite particles are smaller and shorter in intermediate solidification condition compared to slow solidification. Also the images from samples from fast solidification conditions shows even smaller and shorter graphite particles. One typical image from each solidification condition is shown in Figure 71. Some of the images from the fast solidification also exhibits areas of organized orientation of the graphite particles, type E as described in section 2.2.2, which can be seen in the right image in Figure 71.

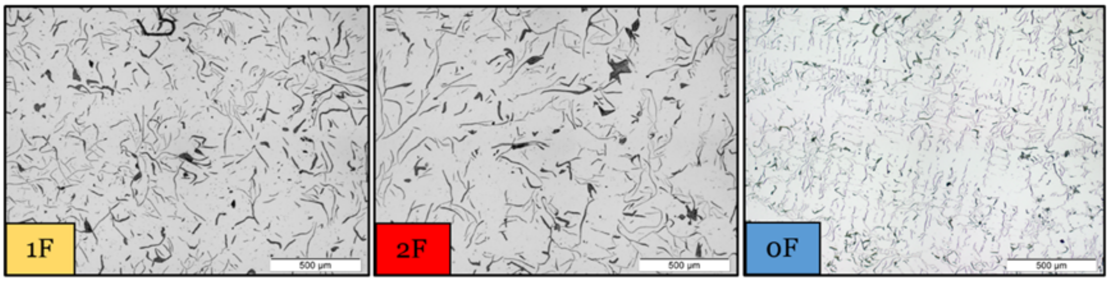

Figure 71. Images from the optical microscope analysis showing the difference in graphite shape and size between the three solidification conditions, intermediate (5B1F image 1), slow (4B2F image 1) and fast (01F image 2).

Graphite fraction

In the image analysis computer software, the graphite fraction of the nine samples were measured and the result can be seen in Table 11. Three images of each sample were analyzed and the mean value of these three is said to be the graphite fraction of that sample.

Table 11. Graphite fraction of each of the nine analyzed samples.

	Graphite fraction					
	Image 1	**Image 2**	**Image 3**	**Mean (µ)**	**STDEV (σ)**	**CV (σ/µ)**
3B1F	10.84	10.61	10.29	**10.58**	0.23	2.13%
4B1F	10.67	9.97	9.46	**10.03**	0.50	4.94%
5B1F	10.33	10.43	9.37	**10.04**	0.48	4.76%
1F				**10.22**	0.49	4.80%
3B2F	10.69	10.16	10.52	**10.46**	0.22	2.11%
4B2F	10.16	9.86	10.39	**10.14**	0.22	2.14%
5B2F	9.15	9.77	10.27	**9.73**	0.46	4.71%
2F				**10.11**	0.44	4.32%
01F	9.99	9.51	10.06	**9.85**	0.24	2.48%
02F	10.09	9.91	9.08	**9.69**	0.44	4.54%
03F	9.98	10.45	10.30	**10.24**	0.20	1.91%
0F				**9.93**	0.39	3.91%

As seen in Table 11 the graphite fraction varies slightly from image to image in a sample, however the variation is quite low. The graphite fraction also varies between each sample, but again the variation is low and all of the nine samples has a graphite fraction of around 10 %.

There is also no sign that the graphite fraction is dependent on the solidification time since the standard deviation within each solidification condition is greater than the difference between the mean graphite fractions of each solidification condition.

Graphite size and distribution

In the image analysis computer software each graphite particle was also measured of its area, the maximum Feret diameter and the perimeter. Table 12 shows the mean values of all the graphite particles from the three sample images for the three parameters.

Table 12. Graphite particles' area. length and perimeter length as the mean value of all particles in each sample.

Mean value of all particles			
Sample	**Area [µm^2]**	**Feret Max [µm]**	**Perimeter [µm]**
3B1F	398.25	51.23	145.23
4B1F	387.28	54.27	145.04
5B1F	355.68	55.32	147.09
Mean (µ) 1F	**380.41**	**53.61**	**145.79**
STDEV (σ) 1F	18.05	1.73	0.93
CV (σ/µ) 1F	4.74%	3.24%	0.64%
3B2F	534.51	63.56	171.84
4B2F	558.72	65.04	182.37
5B2F	516.60	64.64	174.52
Mean (µ) 2F	**536.61**	**64.42**	**176.25**
STDEV (σ) 2F	17.26	0.62	4.47
CV (σ/µ) 2F	3.22%	0.97%	2.54%
01F	167.27	38.82	113.33
02F	175.21	37.44	108.60
03F	143.62	36.20	97.57
Mean (µ) 0F	**162.03**	**37.49**	**106.50**
STDEV (σ) 0F	13.42	1.07	6.60
CV (σ/µ) 0F	8.28%	2.85%	6.20%

As seen in Table 12 the variation between the three samples in each solidification condition is low for all the parameters. What can also be seen is that there is a significant difference between the solidification conditions for all the parameters. The samples taken from slow solidification has graphite particles with larger area, larger Feret maximum and larger perimeter than the samples from intermediate solidification which in return has larger values for all three parameters than the samples from fast solidification as seen in Figure 72.

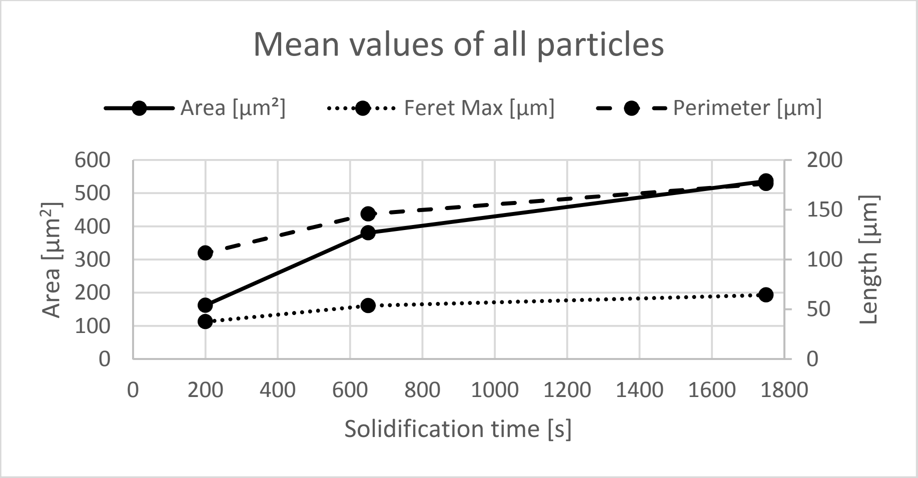

Figure 72. Comparison of the three solidification conditions for each parameter. Mean values of all graphite particles. The area is read on the left vertical axis and the Feret max and perimeter is read on the right vertical axis.

Since the thermal transport in graphite particles occurs predominantly in the a-direction, i.e. along the length of the graphite flakes, the largest graphite particles might have a larger impact on the overall thermal conductivity of the material. Table 13 shows only the top 1 %, i.e. the 99th percentile, of the particles for each parameter in each image in each sample.

Table 13. Graphite particles' area, Feret max and perimeter length. Showing the average of the 99th percentile (top 1 %) of each image in each sample.

Average of the 99th percentile			
Sample	**Area [µm²]**	**Feret Max [µm]**	**Perimeter [µm]**
3B1F	3045.35	230.94	886.80
4B1F	2981.15	246.15	881.59
5B1F	2865.47	252.91	877.29
Mean (µ) 1F	**2963.99**	**243.33**	**881.89**
STDEV (σ) 1F	74.43	9.19	3.89
CV (σ/µ) 1F	2.51%	3.78%	0.44%
3B2F	5222.35	404.69	1292.85
4B2F	4929.06	359.95	1287.04
5B2F	4220.12	322.78	1275.86
Mean (µ) 2F	**4790.51**	**362.48**	**1285.25**
STDEV (σ) 2F	420.73	33.49	7.05
CV (σ/µ) 2F	8.78%	9.24%	0.55%
01F	1319.92	158.05	610.23
02F	1332.61	150.93	639.21
03F	1039.12	145.45	464.25
Mean (µ) 0F	**1230.55**	**151.48**	**571.23**
STDEV (σ) 0F	135.46	5.16	76.56
CV (σ/µ) 0F	11.01%	3.41%	13.40%

When comparing Table 13 and Table 12 it is clear that the largest particles are much larger than the average particles. It can also be seen that the difference between the solidification conditions, as seen in Figure 73, are larger for the 99th percentile than for the mean values in Figure 72.

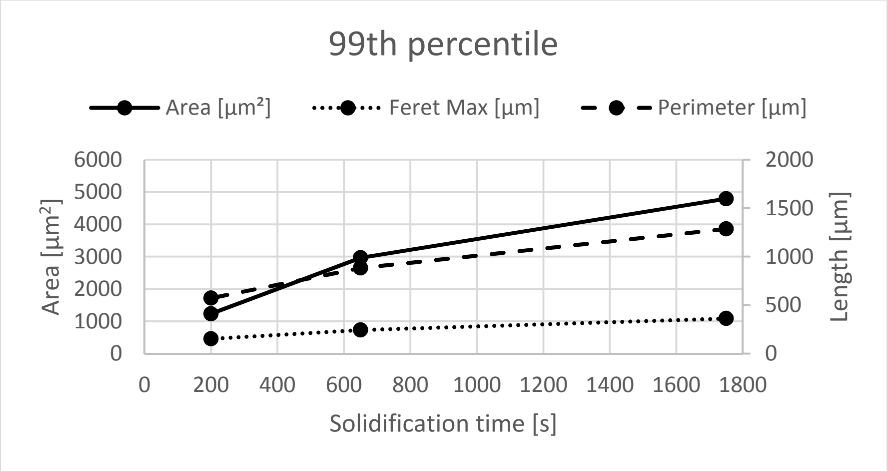

Figure 73. Comparison of the three solidification conditions for each parameter using the 99th percentile values of the graphite particles. The area is read on the left vertical axis and the Feret max and perimeter is read on the right vertical axis.

From the image analysis the number of particles on each image was also counted and an automatic calculation of the number of particles per square millimeter could then be determined. The correlation between the solidification time and the number of graphite particles per mm² is shown in Figure 74. The graph shows the values of the three samples from each solidification condition which are based on all the particles counted in the image analysis.

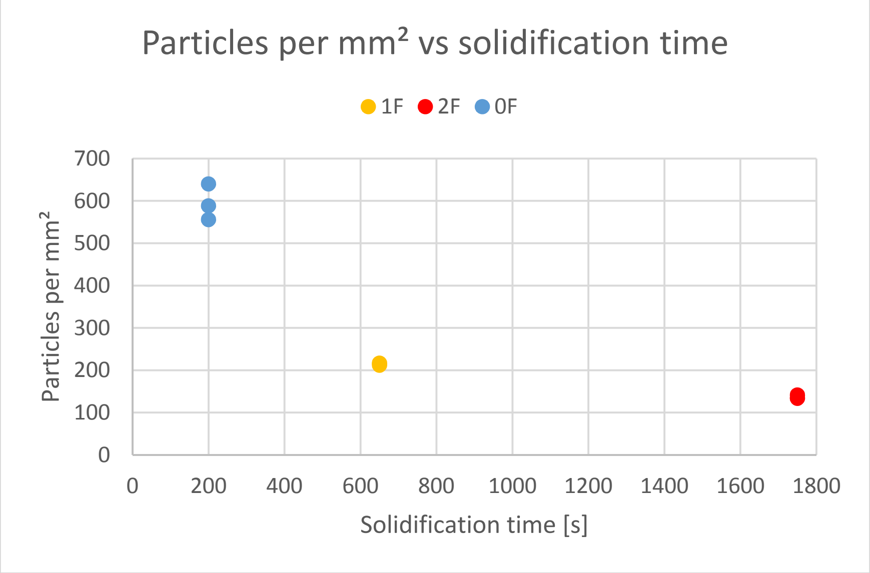

Figure 74. Graph showing the correlation between solidification time and particles per square millimeter.

As seen in Figure 74 there is a clear correlation between the solidification time and the number of particles. The faster the solidification is the number of graphite particles increase. The variation between the samples from the same solidification condition is very small as seen by the grouping of the dots in Figure 74 where the some of the dots are even overlapping each other.

Matrix

The images from the optical microscope analysis of the etched samples were analyzed visually to determine the phases in the matrix of the material. Figure 75 shows images from sample 5B1F. In the left image taken with x20 magnification it can be seen that most of the matrix between graphite particles, the darker grey areas, are of a lamellar structure which indicates that it is pearlite. When studying images of x50 magnification, right image in Figure 75, it can be seen that also the brighter areas, pointed out by the arrow, shows a lamellar structure which means the whole matrix consists of pearlite.

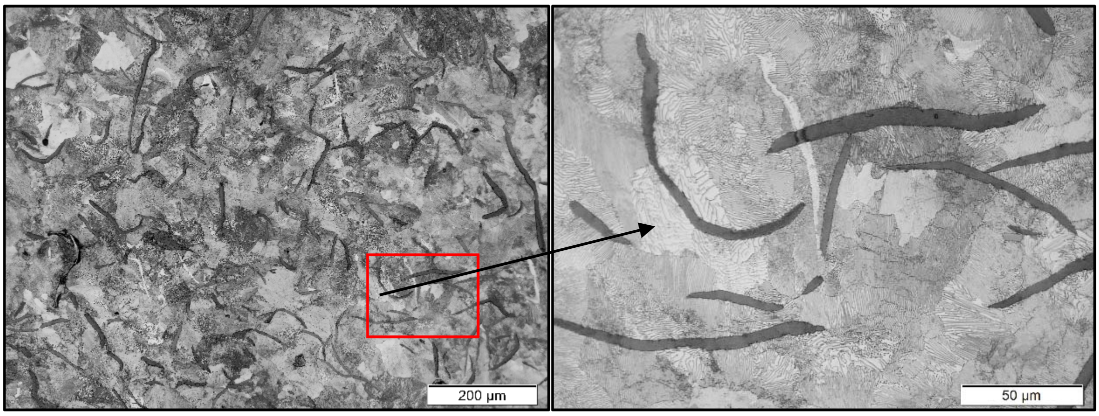

Figure 75. Images from the optical microscope analysis of an etched sample (5B1F) clearly showing a fully pearlitic matrix. The left image is captured with a magnification of x20 and the right image is captured where the red rectangle is with a magnification of x50.

4.3 Comparing modelling- and experimental values for thermal conductivity

The thermal conductivity was modelled using equation (18), (20), (21), (22) and (23) as described in section 2.4.4. The values for thermal conductivity of the microconstituents were set according to the values found in the graphs in Figure 14. For graphite along the c-axis the thermal conductivity was set to 10 W/(m·K), as described in Table 1, for all temperatures. The values used when modelling the effective thermal conductivity can be seen in Table 14.

Table 14. Values for thermal conductivity of the microconstituents used when modelling the effective conductivity.

Thermal conductivity, λ [W/m·K] of microconstituents						
Temperature °C	**25**	**100**	**200**	**300**	**400**	**500**
Graphite, $\lambda_{\parallel}$ (a-axis)	500	430	360	300	260	250
Graphite, $\lambda_{\perp}$ (c-axis)	10	10	10	10	10	10
Pearlite (λ^{*}_{β})	25.6	28	28.5	27.5	26.5	26

Since the matrix was found to be completely pearlitic the fraction ferrite was set to zero. The graphite fraction was set to the values determined in the microstructure analysis in section 4.2.6 for each sample and the values for l_{max} and A was set to the values for Feret max and area also determined in the microstructure analysis in section 4.2.6 for each sample.

The thermal conductivity was modelled both by using the mean values of all particles for Feret max and the area of the graphite particle and by using the 99th percentile, as described in 4.2.6. The result of the modelled thermal conductivity and a comparison with the experimental values at 25°C can be seen in Figure 76 where the lower cluster of data point shows the mean of all particles and the upper cluster shows the 99th percentile.

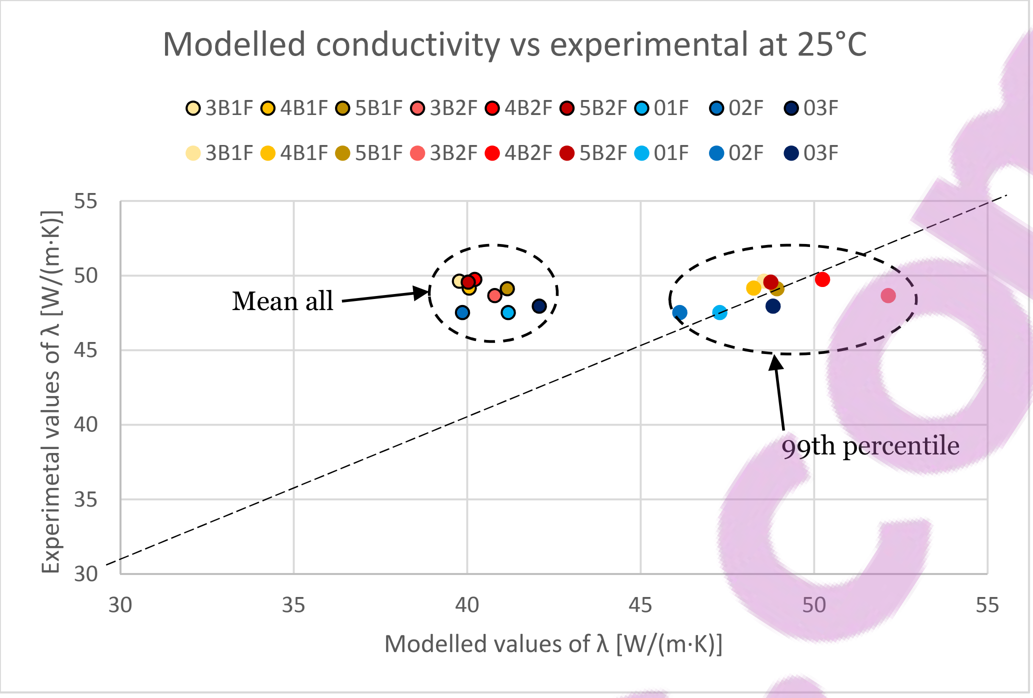

Figure 76. Comparison of the modelled thermal conductivity to the experimental values at 25°C. The dash line represents a theoretical perfect fit. The lower cluster with black rings around the dots uses the mean values of all graphite particles while the upper cluster uses only the 99th percentile of particles when modelling.

As seen in Figure 76 the simulation when using the mean value of all the graphite particles underestimates the thermal conductivity for all the nine samples. The modelled values are around 80-87 % of the experimental values. However, when using the 99th percentile of the graphite particles the model quite accurately predicts the thermal conductivity for eight of the nine samples and the ninth is not very far from the dashed line representing a perfect fit. The modelled values are around 97-102 % of the experimental values except for the outlier, 3B2F, which is 107 % of its experimental value.

The thermal conductivity was also modelled at elevated temperatures using the 99th percentile of the graphite particles and the thermal conductivity of the microconstituents as in Table 14. The modelled values along with the values from experiments made in this thesis are shown in Figure 77 for temperature from 25-500°C in order to compare the two.

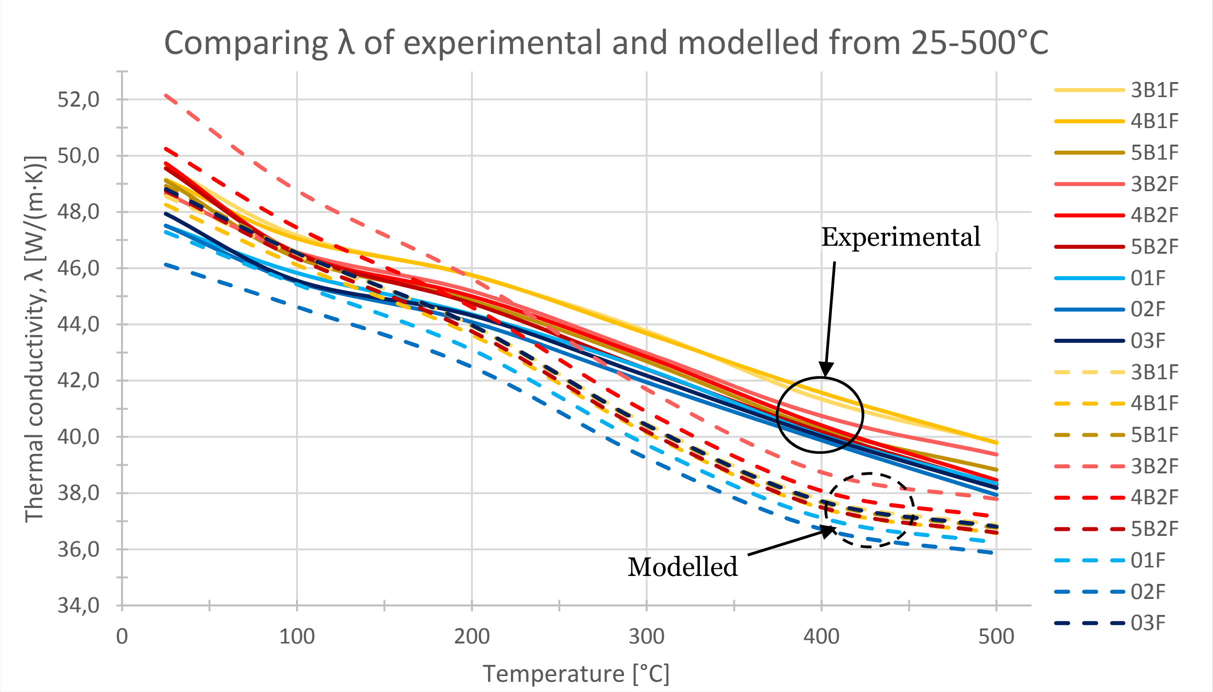

Figure 77. Comparison of the modelled thermal conductivity, of the 99th percentile, to the experimental values at temperatures from 25-500°C.

As seen in Figure 77 the model predicts the thermal conductivity well at 25°C, as seen already in Figure 76. From 25-200°C the model is still quite accurate but at temperatures above 200°C the model underestimates the experimental values. The modelled values are around 93-95 % of the experimental values at 400 and 500°C.

4.4 FEA results

In this section the result regarding the FEA based on both the experimental λ-values and extreme λ-values are displayed. Comparisons are made between a simulation with a homogenous material definition and simulation with a material definition based on local variations.

4.4.1 Experimental values

Input parameters

The homogeneous material definition was set to have the thermal conductivity of the mean value of the samples from 1F as seen in Table 10. The material definition with local variation was set to have the thermal conductivity linearly varying with the solidification time from the lowest values, the mean of the samples in 0F, to the highest values, the mean of the samples in 1F. The local variation of the thermal conductivity can be seen in Figure 78.

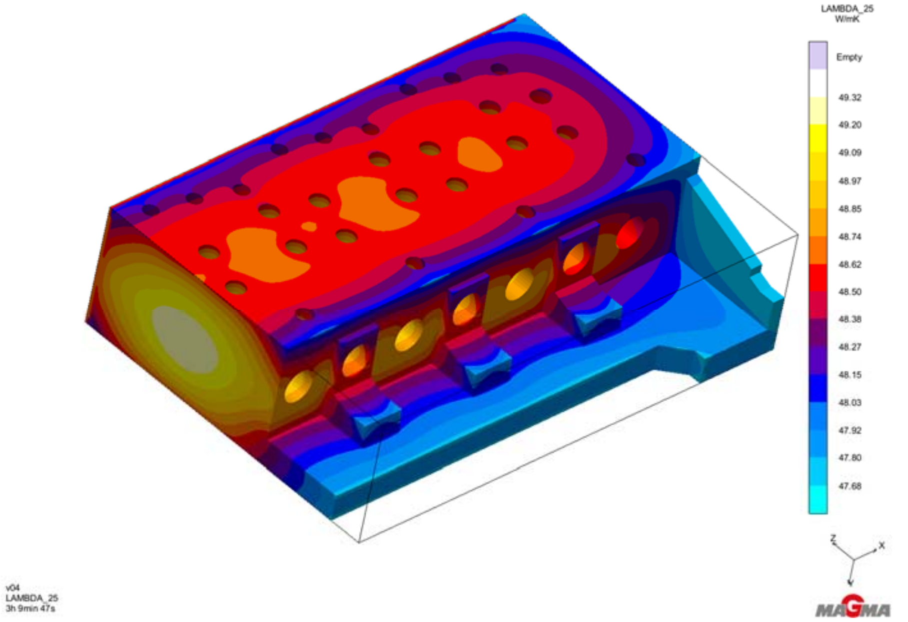

Figure 78. User result defined from casting simulation in MAGMA showing the local variation of thermal conductivity throughout the simplified geometry.

Simulation results

In Figure 79 the temperatures after 1000 seconds can be observed.

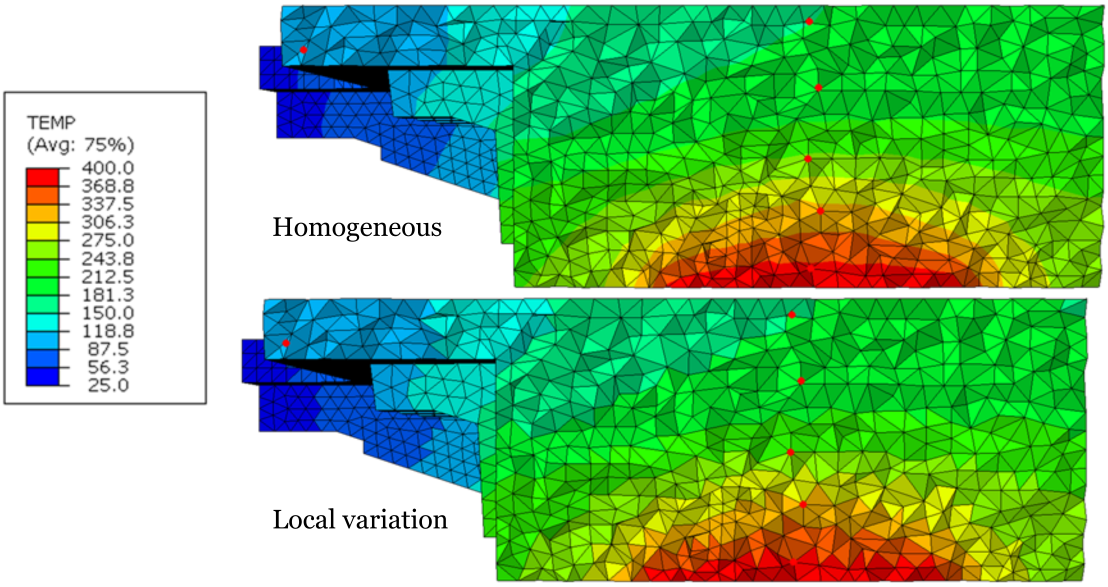

Figure 79. Temperature plot show the result from the simulations with experimental values.

When comparing the two varied simulation set-ups with the experimental thermal conductivity values no significant difference can be seen in the temperature distribution. The measured temperature of the six selected nodes, seen in Figure 47, can be seen as curves in Figure 80 and Figure 81. Also the final temperatures in the nodes are shown.

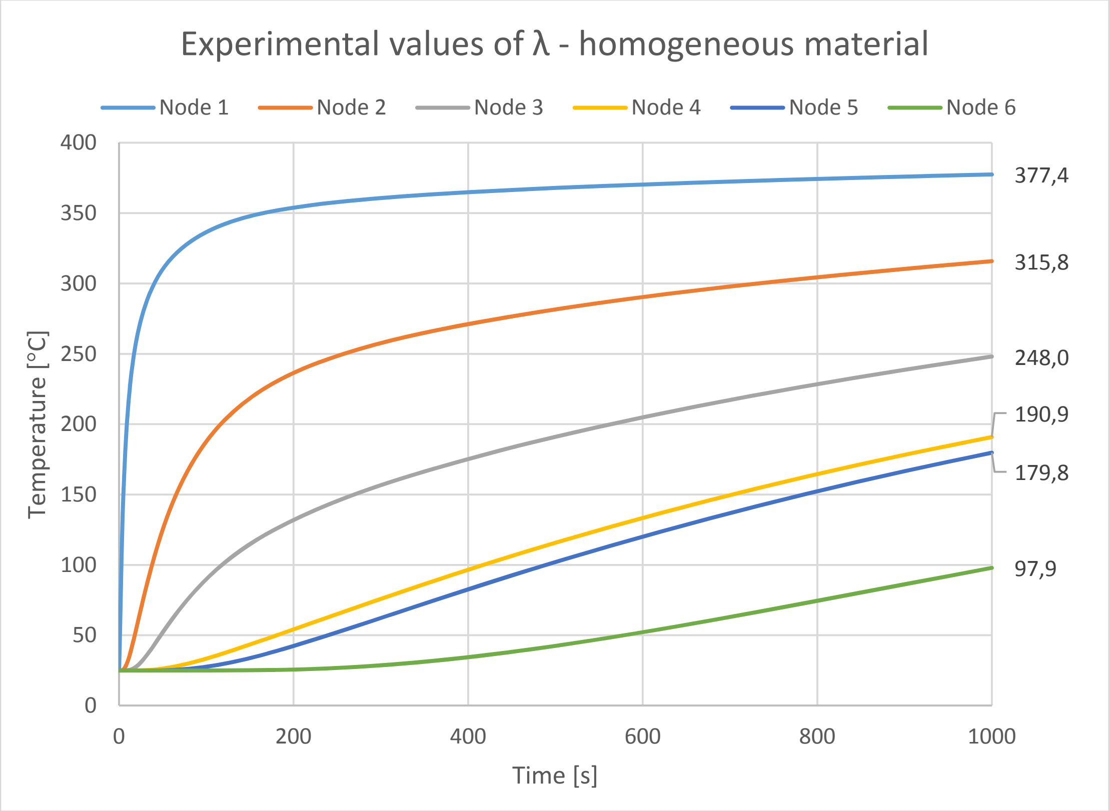

Figure 80. Temperature curves of the six selected nodes using the experimental homogeneous values of thermal conductivity.

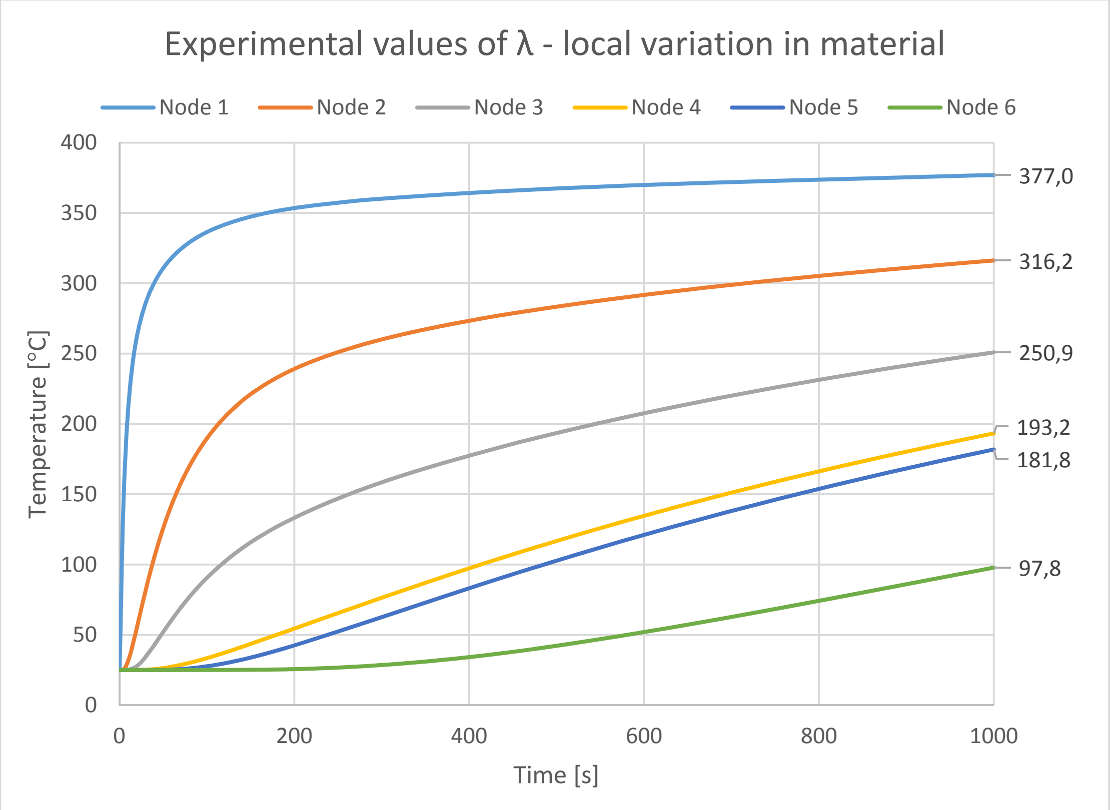

Figure 81. Temperature curves of the six selected nodes using the experimental local values of thermal conductivity.

When comparing Figure 80 and Figure 81 a small variation of the final temperature after 1000 seconds can be seen. The difference of the final temperature is larger when comparing the nodes far away from the heat source. However, the temperature difference between the same nodes from homogeneous and local variation is only around 1°C.

4.4.2 Extreme values

Input parameters

The values used in the simulations with extreme are taken from experiments by Holmgren [25] and they can be seen in Table 15. For the simulation with homogeneous material definition the maximum values in the table were used.

Table 15. Extreme values for thermal conductivity taken from experimental values from Holmgren [25]. Values are from the same material with different solidification condition, minimum values are from "Chill_3" and maximum values are from "Insulation_3".

Temp [°C]	Min λ [W/(m·K)]	Max λ [W/(m·K)]
25	44.5	62.5
100	44.0	55.5
200	43.0	50.0
300	42.0	47.0
400	40.0	43.0
500	38.0	40.0

Simulation results

In Figure 82 the temperatures after 1000 seconds can be observed.

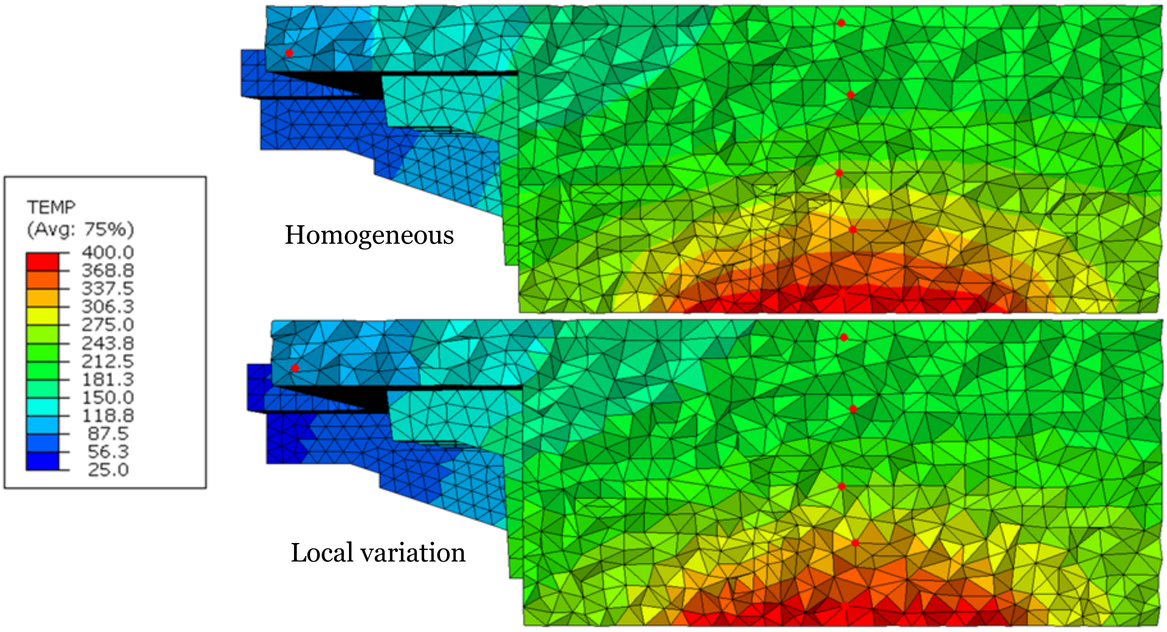

Figure 82. Temperature plot show the result from the simulations with extreme values.

When comparing the two varied simulation set-ups with extreme thermal conductivity values a small difference can be seen in the temperature distribution. The measured temperature of the six selected nodes can be seen as curves in Figure 83 and Figure 84.

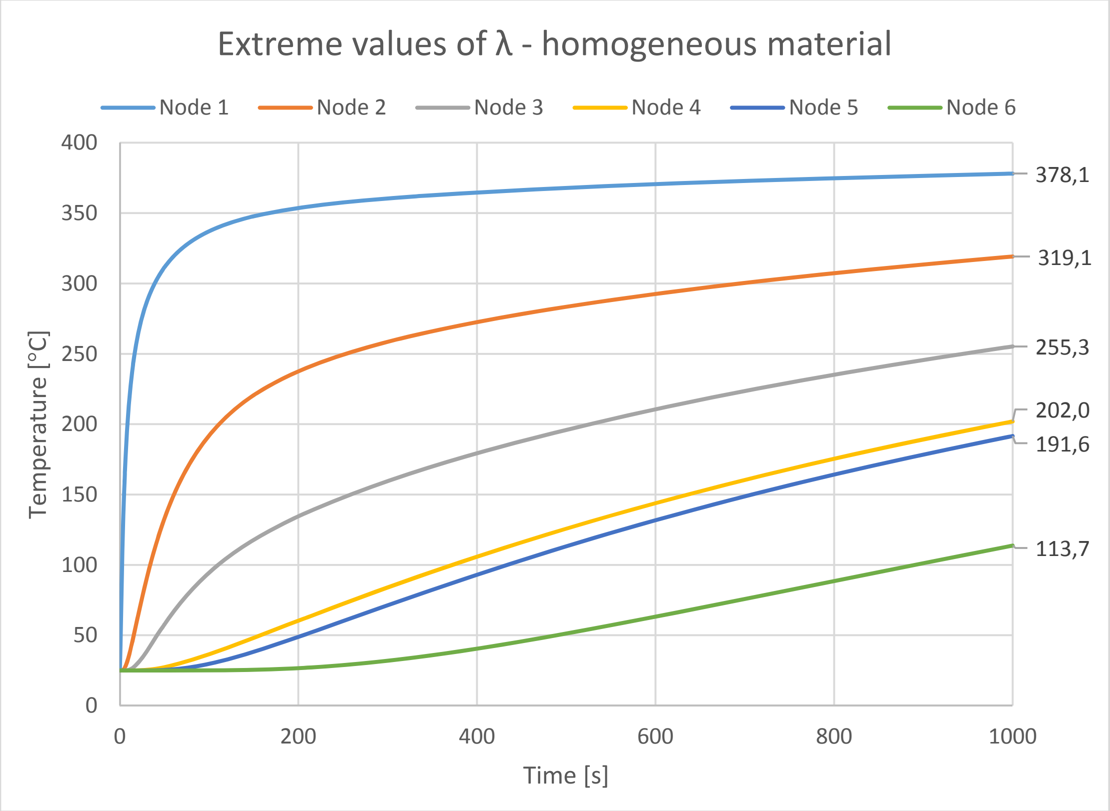

Figure 83. Temperature curves of the six selected nodes using the extreme homogeneous values of thermal conductivity.

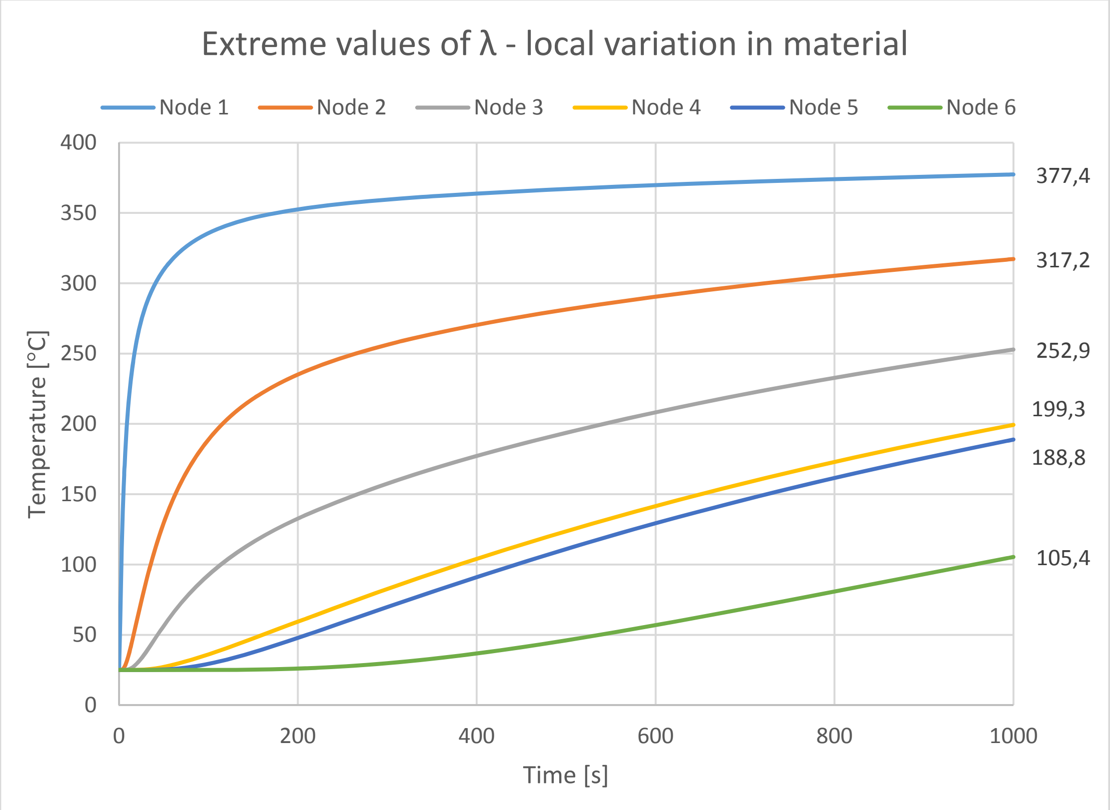

Figure 84. Temperature curves of the six selected nodes using the extreme local values of thermal conductivity.

When comparing results using the extreme values in Figure 83 and Figure 84 a larger variation of the final temperature distribution can be observed after 1000 seconds. Node 6 shows a difference of 8.3°C which is the node most far away from the heat source.

5 Discussion and conclusions

In this section both the methodology in section 3 and the results from section 4 are discussed. Based on the discussion, conclusions are drawn and suggestions for future work that can be done on the subject is presented.

5.1 Discussion of method

The various methods used in this thesis are discussed, along with a small evaluation of the methodology used which are presented in order to improve future work.

5.1.1 Sample extraction

When extracting all samples from the third cylinder head, the samples that were undergoing the mechanical testing were extracted first and only after this was done the physical samples were extracted. The extraction was made in this order to ensure that all 30 of the mechanical samples would be extracted from the same location as the samples extracted from the cylinder heads from the two previous projects. Both the documentation from previous projects and the planning before starting to cut into the third cylinder head could have been improved. If improvements had been done both the physical and mechanical samples could have been extracted at the same time and saved time spent in the workshop.

Mechanical property sample extraction

The first step when sectioning the component into smaller and easier machined parts was by cutting away material using an angle grinder in order to make the 220 kg heavy component fit into the bandsaw. The material section that was cut away may have been affected by the elevated temperature since no cooling was applied. To eliminate the machining of angle grinders a larger bandsaw that would fit the whole component would be the solution. In this thesis project no samples were taken close to the angle grinding cut, the fast solidified samples were at least 5 cm away from the cut.

The final work on the samples intended for the tensile testing was completed by a CNC-lathe machine and resulted in the necking of the tensile bars. It was difficult to accomplish the tolerances needed and therefore it was good that three test bars were used to calibrate the CNC-lathe before machining the 30 real samples needed for this thesis project.

Physical property sample extraction

From all the six selected locations, rectangular cuboids were extracted and machined into the dimensions required for undergoing the three physical property tests. The most difficult stage was to reach the dimensions of the sample undergoing the DSC and dilatometer tests. The samples were stepwise lathed down with steps of approximately 0.1 mm before the desired diameter was achieved. This procedure was critical because increasing the amount of material being removed at each step caused the pressure put on the sample to rise which could result in a sample that would snap off and be destroyed.

5.1.2 Testing

Mechanical property testing

The mechanical property testing of the samples from the third cylinder head was performed in room temperature in order to validate the previous results collected from the first and second cylinder head. All settings were set as the documentation described except the use of the digital image correlation setup used when performing the tensile testing on the first cylinder head.

One out of the 30 tensile bars was destroyed when tested due to a mistake caused by the operator. After each test the tensile bar holders were moved further away from the starting positions caused by the pulling force applied on the tensile bars. This movement was reset by pressing a reset button in the software after each performed test. This action made the tensile bar holders move back to the original positions. The reset button was not pressed before the tensile bar that was destroyed was tested. As a result, the tensile bar holders did not have an area big enough to hold on to and the increased grip pressure crushed the top of the tensile bar.

Physical property testing

The physical property tests were performed from room temperature (25°C) up to 500°C in order to get readings from the work temperatures of the component.

In order to measure the thermal expansion of the investigated material the dilatometer equipment was used. The equipment was timeworn resulting in an oven that had difficulties reaching the temperature required and often reached a temperature of approximate 25°C below the input value. The input maximum temperature was given a higher value in order to compensate the otherwise faulty output data. This problem was managed with the help of an experienced personal that frequently use the equipment.

When all input parameters were configured and the measurements were about to start the push-rod used for measuring the thermal expansion automatically started to press against the sample in the cradle. The push-rod was crooked and needed assistance in order to be placed against the center of the cylindrical sample. This procedure was not ideal and required a couple of attempts before the push-rod established a satisfying placement.

The measurements of the thermal expansion were first planned to only be taken from locations within the component with an intermediate and slow solidification time. It was discovered later on in the project while observing the thermal conductivity values that measurements from locations with fast solidification time were of interest as well. At this point the oven used for the dilatometer was already undergoing mechanical service and would not be used more within this project. Since no measurements of thermal expansions were made for the samples from the fast solidification the density of those samples could not be determined exactly. Instead a change factor between the different temperatures based on the samples from and slow solidification were used.

In order to measure the specific heat, the DSC-equipment was used. There were no significant complications while examining the samples except one small obstruction with one of the calibrations. During the three-hour calibration of the sapphire sample something must have tilted the worktable with the equipment which resulted in a significant deviations of the plotted curve. The calibration of the sapphire was required to be restarted in order to collect correct specific heat values of the material investigated.

When the thermal diffusivity measurements using the LFA were performed, six temperature levels were carefully selected in which readings would be collected; at room temperature (25°C), at 100°C, at 200°C, at 300°C, at 400°C and at 500°C. In all of these temperature levels five measurements were executed in order to collect a statistically reliable mean value. In order to get even better readings, the selected temperature levels could have been increased to eleven by adding measurements every 50°C up to 500°C. The amount of measurements at every temperature level could also have been increased from five to ten in order to collect even more statistically reliable mean values. Taking into account that each sample took approximate 6-7 hours in order to collect all the fulfilling measurements and these changes would have prolonged the time spent examining each sample, which is why the changes was not made in this thesis project.

5.1.3 Sample preparation

The six samples from the already tested tensile bars were extracted with the use of an angle grinding machine with coolant. Extraction in this way made the surfaces flat and facilitated the subsequent work unlike the extraction from the physical property tested samples. The samples from the physical property tested samples were cut out with the use of the lathe machine. Cutting out the samples with the use of the lathe machine also gave flat surfaces but left a small pin in the center that had to be grinded away using sand paper. When grinding down this small pin it was hard to hold the sample in the correct angle in order to get a flat surface. This procedure was also time consuming.

When mounting the samples, a black thermosetting phenolic hot mounting resin called Multifast was used, which is the most common plastic for general use. Another choice would have been to select Polyfast, a thermosetting mounting resin with carbon fiber which is used for edge retention and allows observations to be made in the SEM (Scanning Electron Microscope). No such observations were required in this project and therefore Multifast was selected.

The grinding and polishing steps used in this project were suitable in order to get sufficient surface finish of the samples. The most difficulties were experienced when trying to get rid of all the scratches that were clearly showing when observed in an optical microscope, but still not over polishing the samples which could result in graphite flakes smeared out on the surface or pearlitic structures appearing where it was not desired. The grinding steps were often required to be repeated when observing scratches after finished the polishing steps.

5.1.4 Microstructure analysis

Three images, each based on four merged images, were captured from each sample at different locations, roughly the same locations for all the samples, using the optical microscope. Different locations were chosen in order to verify if the same microstructure occurs throughout the whole sample. Three images might be too few to get a statistically validated result of the microstructure. Additional images would be beneficial for the ocular analysis but also for the image analysis. Alternatively, larger images that includes a larger area with more graphite particles to be analyzed could also be used.

The image analysis was performed by the same person for all the samples examined to minimize the difference in influence by the user, e.g. deciding threshold values and which particles should be excluded from the analysis. The image analysis process was completed during several sessions, it would probably have been beneficial to do all the image analysis at once so the chosen threshold and which particles that should be excluded would remain the same for all the images analyzed.

5.1.5 Connecting casting simulation with FE software

Due to the limited time frame of this project it was decided that the FEA would only consider the physical properties and comparing the effect of using a local variation of the physical properties that have found to be dependent on the solidification condition, i.e. only thermal conductivity, to the standard way of using a homogeneous material definition. Even though the experimental results showed no variation in thermal conductivity between the intermediate and slow solidified samples, the thermal conductivity was set to linearly vary from the lowest value found for the fastest solidified elements to the highest value found for the slowest solidified elements. A non-linear translation of the thermal conductivity to the elements in the casting simulation would have been beneficial to get more realistic results.

The mechanical properties which has been found to have local variations were excluded from the simulations in this thesis project. However, in order to run the type of simulation selected, coupled thermal displacement simulation, some mechanical properties had to be set in order to make the simulation run. The mechanical properties were set as constants. When setting up the simulation the intention was to include also the local variation of mechanical properties and compare the stress in the component. Later it was changed to only consider the local variation of the physical properties which meant that the type of simulation could possibly have been changed.

5.2 Discussion of results

The results presented in this thesis are here discussed. The mechanical test results are first discussed followed by the physical test results. The test results are then discussed together with the results from the microstructure analysis and then the comparison between the experimental results and the modelled values, based on microstructure parameters, for thermal conductivity are discussed.

5.2.1 Mechanical test result

The UTS values from the tensile tests performed on the third cylinder head were found to be close to the results from the two previous tested cylinder heads. The coefficient of variation, CV, is only around 1-7 % for all the 30 samples, excluding the considered faulty sample from the first cylinder head. The mechanical test results from the third cylinder head indicates that mechanical properties are similar in the different location throughout all the three cylinder heads. However, a larger sample size than three would be required in order to validate the results.

The difference in mean value from the three cylinder heads between the highest UTS, 303 MPa, and the lowest, 249 MPa, has been found to be 54 MPa. That is a difference of 22 % which indicates that there is a local variation of UTS throughout the component.

5.2.2 Physical test result

The dilatometer test results showed that there is no difference in the thermal expansion between the samples from intermediate and slow solidification. This result is backed by previous experimental results by Holmgren [25, 26], as described in section 2.4.1. Although, at temperature above 400 degrees all the three samples from intermediate solidification yielded higher thermal expansion than the ones from slow solidification. However, the sample size and the difference is small which means no conclusion can be drawn that slower solidification means lower thermal expansion at high temperature.

The density values of the nine physical property samples indicate no correlation between solidification time and density. The density is sinking with temperature which is as expected as described in section 2.4.1. The density for the samples from fast solidification at elevated temperatures were calculated using change factors based on the change in density between temperatures for the other samples. This assumed there would be no difference in thermal expansion for the fast solidified samples compared to the others, something that was never confirmed with testing. This means the density values for the samples from fast solidification might be somewhat unreliable.

The specific heat was measured to identify local variation; it was known beforehand that the specific heat would not be affected by different solidification condition. Since the DSC-measurements could not yield reliable results for specific heat at temperatures below 100°C the value for 25°C had to be estimated. The three DSC samples resulted in very consistent specific heat values and when plotting the mean values of the three they fall almost perfectly on a line, as seen in Figure 69. This means that when extrapolating that line down to 25°C the approximated value can be very reliable.

The results from the LFA have found that there is virtually no difference in thermal diffusivity, and hence no difference in thermal conductivity between the samples from slow and intermediate solidification. However, a small difference was found between those samples and the samples from fast solidification. The difference was found to be the largest at 25°C and decreased at higher temperature which was also concluded by Holmgren [33] as described in section 2.4.4. The thermal conductivity results are discussed further in section 5.2.4.

5.2.3 Microstructure analysis

The results from the image analysis are quite dependent on the threshold values used to identify the graphite phase both for determining graphite fraction and graphite size and distribution. Also the amount of graphite particles and the average area and Feret max is influenced by the particles excluded from the analysis. In theory only the graphite particles should be included and all the non-graphite particles, e.g. TiCN and MnS, should be excluded. Even though the image analysis was done roughly the same way for all samples examined a small uncertainty of the results should be given.

In the microstructure analysis it was found that the graphite fraction of the mechanical samples varied from 7.5 to 10.5 %, a lot more than the physical samples which yielded graphite fractions from 9.7 to 10.6 %. When looking at the solidification time, which is known for the physical samples, there seem to be no correlation between solidification time and graphite fraction so the variation must be due to other causes.

There seem to be a correlation between the graphite particle area and the UTS where samples with smaller average graphite particles yield higher UTS-values. The same correlation can be found for the Feret max where shorter graphite particles yield higher UTS-values, especially when looking at only the top 1 % of the longest graphite particles. When the physical samples were studied correlation between the solidification times and the graphite area and Feret max could also be found. A faster solidification results in graphite particles with smaller area and shorter Feret max. Also, mechanical property samples with a large number of graphite particles per mm^2 tend to result in higher UTS-values. Again, when locking at the physical samples with known solidification times a clear correlation between the solidification time and the number of graphite particles can be seen. A fast solidification result in larger amount of graphite particles.

A connection could then be drawn between the solidification time and the UTS; faster solidification results in more graphite particles with smaller area and shorter Feret max which in return results in higher UTS-values. However, the spread of the dots representing the UTS in Figure 62 to Figure 65 is quite large which indicate that the graphite microstructure might not be the only thing that affects the mechanical behavior of the material.

5.2.4 Modelling and experimental values of thermal conductivity

The graphite particles' size and length (area and Feret max) has been found to be dependent on the solidification time with larger and longer graphite particles in samples which solidified slower. This would theoretically yield higher thermal conductivity for the samples with larger and longer particles. However, this has not been backed by the experimental results for thermal conductivity in this thesis. It has been found that the thermal conductivity is practically the same for the samples from intermediate and slow solidification. The fast solidified samples however yielded slightly lower conductivity than the other samples.

The modelling of the thermal conductivity predicted the experimental values very accurately when using only the 99th percentile of the graphite particles, as seen in Figure 76. When including all the graphite particles in the model it underestimates the thermal conductivity, similar to the results by Holmgren [25] as seen in Figure 13. This suggests that it is the largest graphite particles that has the most influence on the thermal conductivity and that only the largest should graphite particles should be included in the modelling of the thermal conductivity. Also, the model did not predict the samples from slow solidification to constantly yield higher thermal conductivity than the samples from intermediate solidification, even though there was a difference in graphite area and Feret max. This can be explained to some extent by the difference, however small, in graphite fraction between the different samples.

5.2.5 FEA results

The FEA performed on the simplified geometry of the cylinder head showed that the temperature gradient after applying a heat source of 400°C only differed a tiny bit from the simulation made with homogeneous material compared to the simulation with the local variation of thermal conductivity found in this thesis' material tests. The difference is so small, approximately 1°C in the node furthest away from the heat source after 1000 s, which in this component with this material the local variation of physical properties might be unnecessary. When using more extreme difference in thermal conductivity for grey iron, found in the literature, the difference between the homogeneous and the local variation increased some, around 8°C in the node furthest away from the heat source.

However, the temperature gradient is not itself what is of interest in this kind of component. It is the thermal stresses the thermal gradient gives rise to. The thermal stresses are also dependent on the mechanical properties, which were not included in the simulations in this thesis project. The mechanical properties have been found to have local variation within the cylinder head and they should be included in future work within this research project since they might be largely contributing to the difference in thermal stresses when using local variation of material properties compared to homogeneous.

5.3 Conclusions

The research questions that this thesis aimed to give answers to, described in section **Error! Reference source not found.**, are here restated and answers are given based on the results found in this thesis project.

- *Will the local mechanical properties of cylinder head one and two be validated by the results from the third cylinder head?*

As discussed in section 5.2.1 the mechanical test results from the third cylinder head indicates that the results of all three cylinder heads are similar since the variation of the UTS-values from each sample location is low and the coefficient of variation is only between 1-7 %. A validation would require investigating more than three components.

- *How are the mechanical properties varying within the studied component and can the variations be connected to the local microstructure of the material?*

The tensile test results performed on the three cylinder heads indicates that there are local variations of the mechanical properties. The difference in UTS-value between the highest and lowest samples is 54 MPa which is a 22 % difference which means that the variation is large enough to be significant. With the microstructure analysis, correlations have been found between the UTS and some of the microstructural parameters, e.g. Feret max, graphite area and number of graphite particles per mm^2. Finer graphite structure with more, shorter and smaller graphite particles generally gives higher UTS. The variation in UTS can however not be explained solely by the graphite microstructure which indicates that the mechanical behavior is more complex. It is most likely also dependent on the matrix and defects in the material.

- *How are the physical properties varying within the studied component and can the variations be connected to the local microstructure of the material and be predicted by a casting simulation?*

Most of the physical properties were found to not have local variation, e.g. thermal expansion, density and specific heat. The thermal diffusivity and thereby also the thermal conductivity was found to have small variations within the studied component. However, there is no significant difference in thermal conductivity found when observing the results from the samples from the thick main body of the cylinder head which includes the samples from slow and intermediate solidification. Only when compared with the samples taken from the section with fast solidification a difference can be seen. The thermal conductivity is slightly lower in the section with fast solidification, 47.65 W/m·K compared to 49.31 W/m·K at 25°C. The difference decrease at higher temperature.

When comparing the graphite microstructure parameters there is a significant difference between the three solidification conditions. The slower the solidification is, the longer the graphite particles are, i.e. large Feret max, especially the longest (99th percentile). The studied model for thermal conductivity has been found to underestimate the thermal conductivity if considering the mean values of Feret max and graphite area from all the graphite particles in a sample. However, when using only the longest, 99th percentile, of the graphite particles the model predicts the experimental values very well. The model did not predict the samples from slow solidification, which has the longest graphite particles, to have higher thermal conductivity than the samples from intermediate solidification since it also takes into account the small local variation in graphite fraction. The local variation of graphite fraction has however not been found to have any correlation with the solidification time which was the only casting condition parameter studied in this thesis.

- *How can a casting simulation be connected to an FE software to include local variation of physical properties in the FEA?*

In this thesis project a methodology for connecting a casting simulation to an FE software to include local variations of thermal conductivity has been worked out and it is described in detail in section 3.6. The results from the simulations, presented in section **Error! Reference source not found.**, shows that the difference in temperature distribution throughout the component is very small when using homogeneous thermal conductivity values compared to the experimentally found local variation. This suggest that local variations of physical properties might not need to be considered in this specific component with this material. However, simulations with more extreme difference between the highest and lowest thermal conductivity shows that a larger and more significant difference in temperature distribution between a homogeneous and a locally variating material definition can be achieved. This means that in other types of component with larger variations of thermal conductivity, or other properties, due to large difference of material thickness or in other types of material, local variations of physical properties could be considered. In those cases, the methodology presented in this thesis can be used successfully.

If considering the local variation of material properties, both mechanical and physical, in a cast material when designing components, combined with design optimization, truly optimized components could be achieved. This will reduce the material usage which in components used in the automotive industry results in lower fuel consumption leading to less emissions. Beneficial both economically and environmentally.

5.4 Future work

This thesis project has been a part of an ongoing research project within the Materials and manufacturing department at Jönköping University. Some suggestions for the continuation of this work are here presented:

- Complete image analysis on all the mechanical samples from all three cylinder head to get a larger statistical base for the correlation between microstructural parameters and ultimate tensile strength.
- Perform FEA on the real geometry with a realistic load case.
- Include local variation of mechanical properties and compare to a homogeneous material. Also test to find out what impact the variation of thermal conductivity has to the stress results from the simulation.
- Include thermally dependent mechanical properties to really simulate the behavior of the component at elevated temperature.
- Perform compression tests on samples from the same location as the tensile test samples and include the compression strength in the simulations.
- Include a non-linear connection between experimental values that have local variation to the solidification time determined by the casting simulation.
- Investigate local variations of material properties in other materials and use the methodology described in this thesis to connect casting simulation to FEA.

6 References

[1] K. Tanner, "Experimental research designs," in *Research Methods for Students, Academics and Professionals (Second Edition)*, ed: Chandos Publishing, 2002, p. 126.

[2] K. Williamson, F. Burstein, and S. McKemmish, "The two major traditions of research," in *Research Methods for Students, Academics and Professionals (Second Edition)*, ed: Chandos Publishing, 2002, pp. 25-47.

[3] J. Olofsson, "Simulation of Microstructure-based Mechanical Behaviour of Cast Components," ed, 2014.

[4] M. Li, "Experimental investigation on local properties of a grey cast iron component," Jönköping University - School of Engineering 2015.

[5] G. Stark and T. Svensson, "Investigation of local properties of a grey cast iron component - Experimental with support of stereo digital image correlation," Bachelor thesis, Materials and manufacturing, Jönköping University - School of engineering, 2015.

[6] G. M. Goodrich, "Introduction to Cast Irons," in *ASM Handbook Online*. vol. 15 - Casting, ed: ASM International, 2008, pp. 785-811, http://www.asmmaterials.info.

[7] G. M. Goodrich, "Gray Iron Castings," in *ASM Handbook Online*. vol. 15 - Casting, ed: ASM International, 2008, pp. 835-855, http://www.asmmaterials.info.

[8] H. R. Abbasi, M. Bazdar, and A. Halvaee, "Effect of phosphorus as an alloying element on microstructure and mechanical properties of pearlitic gray cast iron," *Materials Science and Engineering: A,* vol. 444, pp. 314-317, 2007.

[9] R. Gundlach, M. Meyer, and L. Winardi, "Influence of Mn and S on the Properties of Cast Iron Part III—Testing and Analysis," *International Journal of Metalcasting,* vol. 9, pp. 69-82, 2015.

[10] M. Selin, "On thermal conductivity and strength of compacted graphite irons : influence of temperature and microstructure," Chalmers University of Technology, Göteborg, 2010.

[11] M. Selin, D. Holmgren, and I. L. Svensson, "Effect of alloying elements on graphite morphology in CGI," vol. 649, ed, 2010, pp. 171-176.

[12] "ASTM A247-10," in *Standard Test Method for Evaluating the Microstructure of Graphite in Iron Castings*, ed. West Conshohocken, PA: ASTM International, 2010.

[13] C. V. White, "Gray Iron," in *ASM Handbook Online*. vol. 1 - Properties and Selection: Irons, Steels and High-Performance Alloys, ed: ASM International, 1990, pp. 12-32, http://www.asmmaterials.info.

[14] R. O'Rourke, "CAST IRON: The Engineered Metal," *Advanced Materials & Processes,* vol. 159, pp. 65-68, 2001.

[15] J. R. Davis and Associates, "Metallurgy and Properties of Gray Irons," in *ASM Specialty Handbook - Cast Irons*, ed Ohio: ASM International, Material Park, 1996, pp. 32-53.

[16] G. L. Rivera, R. E. Boeri, and J. A. Sikora, "Solidification of gray cast iron," *Scripta Materialia,* vol. 50, pp. 331-335, 2// 2004.

[17] D. Richfield. (2009, 24.03.2016). *File:Stress v strain A36 2.svg*. Available: https://commons.wikimedia.org/wiki/File:Stress_v_strain_A36_2.svg

[18] I. Svensson and T. Sjögren, "ON MODELING AND SIMULATION OF MECHANICAL PROPERTIES OF CAST IRONS WITH DIFFERENT MORPHOLOGIES OF GRAPHITE," *International Journal of Metalcasting,* vol. 3, pp. 67-77, 2009.

[19] J. Olofsson and I. Svensson, "Incorporating predicted local mechanical behaviour of cast components into finite element simulations," *Materials and Design,* vol. 34, pp. 494-500, 2012.

[20] K. G. Samuel, "Limitations of Hollomon and Ludwigson stress–strain relations in assessing the strain hardening parameters," *Journal of Physics D: Applied Physics,* vol. 39, p. 203, 2006.

[21] D. C. Ludwigson, "Modified stress strain relations for fcc metal," *Metallurgical transactions,* vol. 2, pp. 2825-2828, 1971.

[22] W. D. Callister, "Materials science and engineering : SI version," D. G. Rethwisch, Ed., 8. ed.. ed Hoboken, NJ: Wiley, 2011, pp. 781-799.

[23] T. Atkins and M. Escudier. (2013). *A dictionary of mechanical engineering - thermal expansion (expansivity)*. Available: http://www.oxfordreference.com/view/10.1093/acref/9780199587438.001.0001/acref-9780199587438-e-6607?rskey=OglcDu&result=6

[24] what-when-how.com. (2016-02-04). *Cylinder Head (Automobile)*. Available: http://what-when-how.com/automobile/cylinder-head-automobile/

[25] D. M. Holmgren, A. Diószegi, and I. L. Svensson, "Effects of transition from lamellar to compacted graphite on thermal conductivity of cast iron," *International Journal of Cast Metals Research,* vol. 19, pp. 303-313, 2006/12/01 2006.

[26] D. Holmgren and M. Selin, "Regression model describing the thermal conductivity of various cast irons," vol. 649, ed, 2010, pp. 499-504.

[27] W. D. Callister, "Materials science and engineering : SI version," D. G. Rethwisch, Ed., 8. ed.. ed Hoboken, NJ: Wiley, 2011, p. 51.

[28] T. Atkins and M. Escudier. (2013). *A dictionary of mechanical engineering - specific heat (specific-heat capacity, C)* Available: http://www.oxfordreference.com/view/10.1093/acref/9780199587438.001.0001/acref-9780199587438-e-5925?rskey=Jq0RXq&result=1

[29] J. R. Davis and Associates, "Physical properties," in *ASM Specialty Handbook - Cast Irons*, ed Ohio: ASM International, Material Park, 1996, pp. 428-436.

[30] K.-O. Yu, "Modeling for casting and solidification processing," K.-O. Yu, Ed., ed New York: Marcel Dekker, 2002, p. 218.

[31] D. Holmgren, "Thermal conductivity of cast iron," Department of Component Technology-Castings, 2006.

[32] D. Holmgren, "Review of thermal conductivity of cast iron," *International Journal of Cast Metals Research,* vol. 18, pp. 331-345, 2005.

[33] D. Holmgren and I. L. Svensson, "Thermal conductivity–structure relationships in grey cast iron," *International Journal of Cast Metals Research,* vol. 18, pp. 321-330, 2005.

[34] J. Helsing and G. Grimvall, "Thermal Conductivity of Cast Iron: Models and Analysis of Experiments," *Journal of Applied Physics (USA),* vol. 70, pp. 1198-1206, 1991.

[35] G. Grimvall, "Physical properties of multiphase alloys," vol. 123-125, G. Grimvall, Ed., ed, 1992, pp. 297-303.

[36] W. Gaudig, R. Mellert, U. Weber, and S. Schmauder, "Self-consistent one-particle 3D unit cell model for simulation of the effect of graphite aspect ratio on Young's modulus of cast-iron," *Computational Materials Science,* vol. 28, pp. 654-662, 2003.

[37] M. Selin and M. Konig, "Regression Analysis of Thermal Conductivity Based on Measurements of Compacted Graphite Irons.(Report)," *Metallurgical and Materials Transactions A,* vol. 40, p. 3235, 2009.

[38] D. Holmgren, "Modelling the Thermal Conductivity of Various Cast Irons," *Key Engineering Materials,* vol. 457, pp. 318-323, 2011.

[39] T. Sjögren, D. Holmgren, and M. Rinvall, "Study of the thermal and mechanical properties of pearlitic and ferritic cast iron matrices," *International Foundry Research/Giessereiforschung,* vol. 59, pp. 14-21, 2007.

[40] T. Atkins and M. Escudier. (2013). *A dictionary of mechanical engineering - tensile test (tension test)*. Available: http://www.oxfordreference.com/view/10.1093/acref/9780199587438.001.0001/acref-9780199587438-e-6552?rskey=48sf7k&result=1

[41] (2016-02-05). *ISO 6892-1:2009 Metallic materials -- Tensile testing -- Part 1: Method of test at room temperature*. Available: http://www.iso.org/iso/catalogue_detail.htm?csnumber=51081

[42] T. Matsushita, "Dilatometer," G. Söderström, Ed., ed: Jönköping University School of Engineering, [videoclip] 2015.

[43] D. M. Holmgren, A. Diószegi, and I. L. Svensson, "Effects of Inoculation and Solidification Rate on Thermal Conductivity of Grey Cast Iron," presented at the 67th World Foundry Congress, Harrogate, United Kingdom, june, 2006.

[44] T. Matsushita, "Differential Scanning Calorimetry (DSC) ", G. Söderström, Ed., ed: Jönköping University School of Engineering, [videoclip] 2015.

[45] T. Matsushita, "Laser Flash," G. Söderström, Ed., ed: Jönköping University School of Engineering, [videoclip] 2015.

[46] Volvo. (1994-06, 2016-02-05). *Tensile test pieces, type C*. Available: https://webstd.volvo.com/webstd/docs/1014,213

[47] "MAGMA5, v. 5.3.0.2," ed. Aachen, Germany: MAGMA Gießereitechnologie GmbH, 2011.

[48] J. M. Radzikowska, "Metallography and Microstructures of Cast Iron," in *ASM Handbook Online*. vol. 9 - Metallography and Microstructures, ed: ASM International, 2004, pp. 565–587, http://www.asmmaterials.info.

[49] "Stream Motion, v. 1.9," ed. Shinjuku Monolith, 3-1 Nishi-Shinjuku 2-chome, Shinjuku-ku, Tokyo, Japan: OLYMPUS CORPORATION, 2013.

[50] A.Velichko and F. Mücklich, "Shape Analysis and Classification of Irregular Graphite Morphology in Cast Iron," *Praktische Metallographie,* vol. 43, pp. 192-208, 10.03.2006 2005.

[51] "Stream Motion Desktop, v. 1.9.1," ed. Shinjuku Monolith, 3-1 Nishi-Shinjuku 2-chome, Shinjuku-ku, Tokyo, Japan: OLYMPUS CORPORATION, 2014.

[52] "SOLIDWORKS Education Edition, 2015 SP3.0," ed. Vélizy-Villacoublay, France: Dassault Systèmes, 2015.

[53] "Abaqus/CAE 6.13-5," ed. Providence, RI, USA: Dassault Systèmes Simulia Corp, 2013.

[54] MathIsFun.com. (2014, 2016-05-06). *Standard Deviation Formulas*. Available: https://www.mathsisfun.com/data/standard-deviation-formulas.html

[55] "MATLAB R2014b, v. 8.4.0.150421," ed. Natick, Massachusetts USA: MathWorks, 2014.

7 Search terms

8 Appendices

Appendix 1 – Lengths of the dilatometer samples
Appendix 2 – Masses of the DSC samples
Appendix 3 – Thicknesses of the LFA samples

8.1 Appendix 1

Lengths of the dilatometer samples.

Sample	Length [mm]
3B1F	12.035
4B1F	12.025
5B1F	11.950
3B2F	12.095
4B2F	12.020
5B2F	12.050

8.2 Appendix 2

Masses of the DSC samples.

Sample	Mass [mg]
DSC1	91.70
DSC2	94.70
DSC3	96.60

8.3 Appendix 3

Thicknesses of the LFA samples.

Sample	Thickness [mm]
3B1F	4.415
4B1F	4.295
5B1F	4.250
3B2F	4.385
4B2F	4.325
5B2F	4.280
01F	4.180
02F	4.365
03F	4.235